UNIVERSITA' DEGLI STUDI DI PARMA

DOTTORATO DI RICERCA IN

Scienza e Tecnologia dei Materiali

CICLO XXXIV

Design and Development of Printable and Injectable

Bio-Hybrid Inks for Tissue Engineering and Regeneration

Coordinatore:

Chiar.mo Prof. Enrico Dalcanale

Tutore:

Chiar.ma Dott.ssa Monica Sandri

Dottoranda: Margherita Montanari

Anni Accademici 2018/2019 – 2020/2021

Design and Development of Printable and Injectable Bio-Hybrid Inks for Tissue Engineering and Regeneration

Margherita Montanari

Contents

Aim

Within this work we applied the principles of biomimicry to develop printable and injectable gealtine-based bio-hybrid inks to target the regeneration of three different tissues: chondral tissue, bone tissue and neural tissue.

Starting by the same natural biopolymer, gelatine, derived by hydrolysis of collagen, the main human body extra-cellular matrix (ECM) constituent, we exploited different process technologies, functionalization, and crosslinking techniques to develop devices suitable for the targeted tissues engineering.

More specifically, we performed a process comparison among two process technology, three-dimensional printing, and mould casting, for the realization of three-dimensional scaffolds for chondral regeneration. We developed nano-hydroxyapatites (nHAs) functionalized bioinks embedding human bone marrow stem cells (hBMSCs) and possible to crosslink with visible (VIS) light for bone regeneration and we designed and realized an *in-vivo* injectable and *in-situ* crosslinkable conductive ink for neural regeneration.

An all-round characterization of the crucial aspects for each device was thoroughly performed, highlighting the main achievements and hindrances, as well as the main aspects overall possible to be improved.

CHAPTER 1

Introduction

1.1 Regenerative medicine and tissue engineering

Regenerative medicine is the branch of medicine that develops methods to regrow, repair or replace damaged or diseased cells, tissues, or organs[1,2,3].
It includes genic therapy, genomic editing, cell therapy and tissue engineering.

Among those, tissue engineering is attracting more and more attentions due to its potential. It is an interdisciplinary field that applies the principles of life sciences and engineering towards the development of biological substitutes to restore, maintain, or improve tissue and organs functions (Fig. 1.1).

It consists in the development of engineered scaffolds, loaded or not with cells and drugs, operating within the organism as closed or open systems[4,5].

The scaffold must be able to mime the structure and biological function of natural extracellular matrix (ECM) in terms of both chemical composition and physical structure[6].
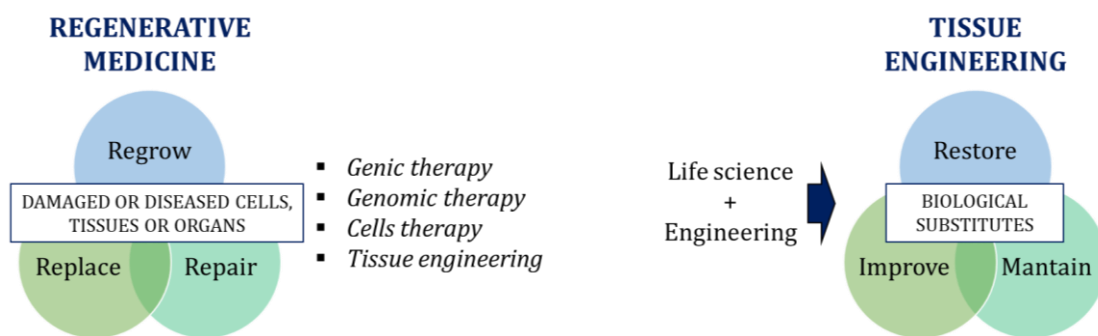
Fig. 1.1 Regenerative medicine and tissue engineering graphical definitions.

ECM is originally known for its role in providing structural support to cells and as a location for cell migration[7]. Appropriate scaffolds for tissue engineering applications should be biodegradable, biocompatible, nontoxic, non-mutagenic, and nonimmunogenic. Furthermore, they should be able to provide appropriate

mechanical support and show favorable surface properties, such as helping adhesion, proliferation and differentiation of cells[6,8].

1.2. Biomimicry

But which better teacher than Nature to learn how to face and solve some of the outstanding issues humans are struggling with?

The art, even if would probably be more accurate to say the science, to look at, learn from, and mimic the strategies found in Nature to solve the most diverse human challenges is called biomimicry [9,10].

Multiples are the examples of successfully applied biomimicry in the most diverse fields, from the "lotus effect" employed to create self-cleaning surfaces[11–13], to the thistle used as inspiration for the creation of Velcro®, passing by new generation adhesives applying the gecko pawn rule[14], till arriving to architecture and functional design[9] (Fig. 1.2).

| *Lotus effect and self cleaning surfaces* | *Thistle and Velcro®* | *Gecko pawns and adhesives* | *Architecture and functional design* |
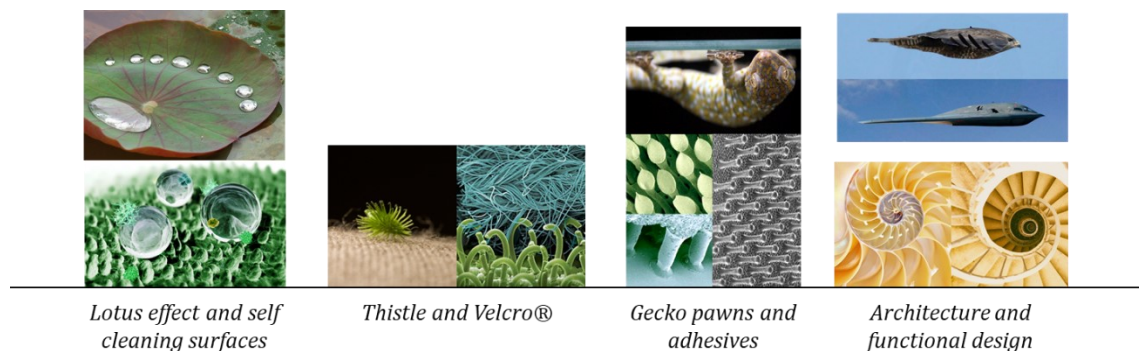
Fig. 1.2 Examples of successfully applied biomimicry in the most diverse fields, from tissue industry to architecture and functional design.

1.3. Designing a tissue engineering device

But which are the steps to make when designing a device for tissue engineering (Fig. 1.3)?
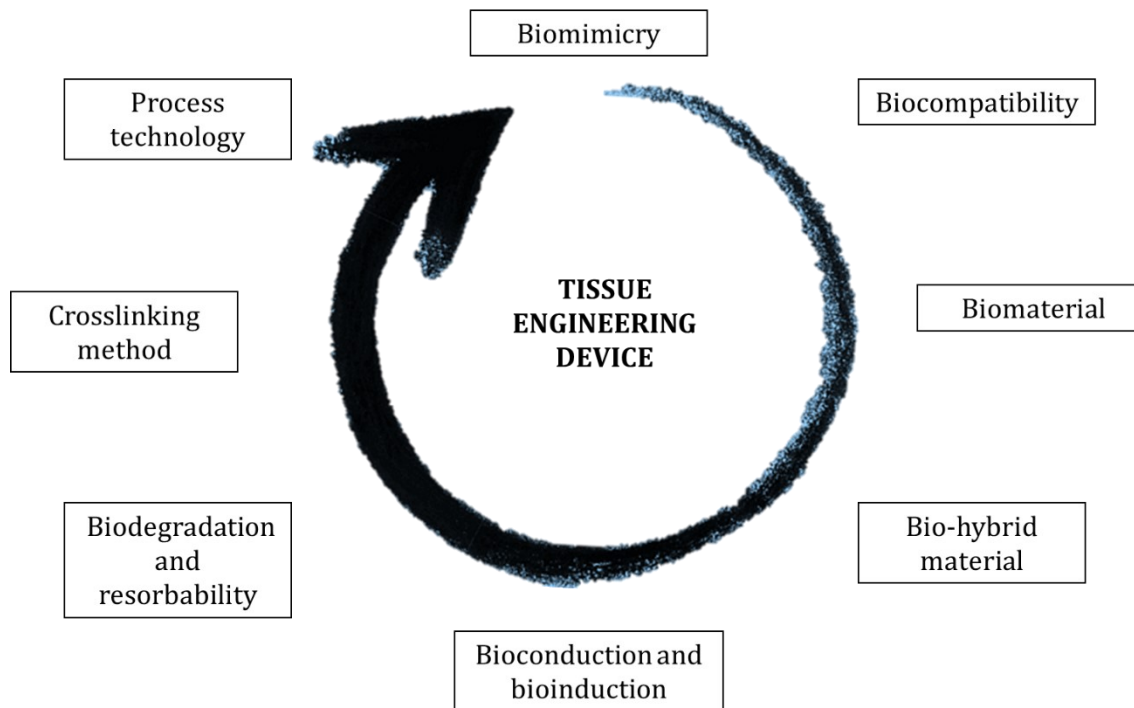
Fig. 1.3 Schematic representation of the steps to follow when designing a device for tissue engineering.

1.3.1 Biomimicry applied to tissue engineering

It has been said the first one is to look at the Nature. Finding if we can get a hint on the direction to take to solve the problem. The design and development of three-dimensional scaffolds that reproduce the structural and morphological complexity of human tissues and organs is still a challenge because of different limitations in currently available manufacturing technologies. With this in mind, new trends in materials science research are focussing on the unique characteristics and properties of natural structures and processes, using these as new sources of inspiration in the development of innovative devices[10,15,16,17].

1.3.2 Biocompatibility

It has to be taken in mind the designed device will have to work within a living organism, which means it has to be biocompatible, a term that is right now in continuous need of a reappraising definition due to the quick evolution of the field and that can have different meanings depending on the context but that we can overall define as the ability of a component to perform in a specific situation within a living organism with an appropriate host response[18].

1.3.3 Biomaterials

The next step is the election of the best biomaterial to be used for the device realization.

A biomaterial is defined as a substance that fit the definition of biocompatibility and that can be exploited, alone or as part of a complex system, to direct by controlled interactions with a living system the course of therapeutic or diagnostic procedure. The general definition of biomaterial has evolved in time with the evolutions of biomaterials themselves. While among 1960 and 1970 biomaterials definition was used to indicate inert materials that were possible to be used in replacing damaged tissues providing structural support with minimal impact on the patient, within 1980 and 1990 the definition shifted to identify bioactive materials able to promote, thanks to functional coatings, a biological reaction in the contact area between the material and the host with an increased effectiveness of the medical device. These biomaterials were although still presenting considerable setbacks, especially in terms of infections and immunological reactions, problems that were overcome with the creation, in the first decade of 2000s, of biodegradable materials, able to degrade and be absorbed by the host, thereby minimizing, or avoiding the disadvantages of permanent implants. Those paved the way for the creation, in the second decade of 2000s, of the so called "smart biomaterials", made possible by the advances in different fields, that are featured by the ability of emulating natural structures and mechanisms, repairing, and regenerating the damaged tissues by promoting specific reactions of the cells. These materials are the ones nowadays referred as biomimetic materials[19].

1.3.4 Synthetic and natural biopolymers

Biomaterial election in the design of a device for tissue engineering is a fundamental step. Some of the most used biomaterials employed for tissue engineering are biopolymers. But we need to make a distinguish among two main classes of biopolymers: synthetic biopolymers and natural biopolymers. While both can be biocompatible and biodegradable, they show some crucial differences (Fig. 1.4).
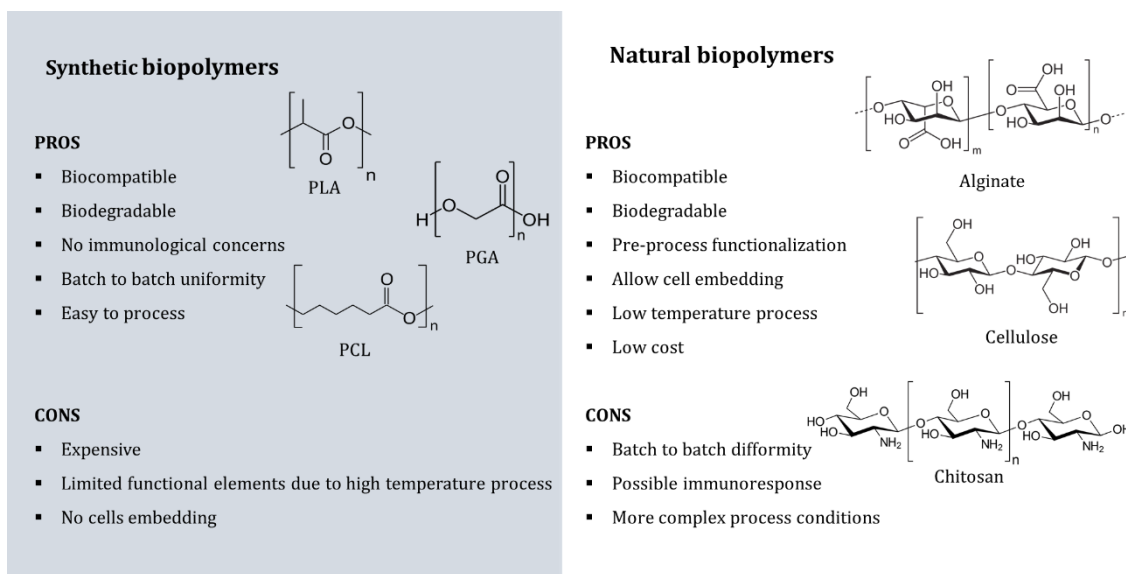
Fig. 1.4 Main features of synthetic and natural biopolymers, with some examples for each biopolymer class.

Synthetic biopolymers have a minimum risk of inducing an immunological response, show batch to batch uniformity and they are normally easy to process. At the same time, they are expensive, pre-process functionalization is limited by the high temperature required to process them and for this they do not allow cells embedding[4,5,20,21].

Among the main used synthetic biopolymers in tissue engineering are polycaprolactone (PCL), an aliphatic and semi-crystalline polymer that exhibits superior toughness and mechanical strength along with adequate biocompatibility, polyglycolic acid (PGA) and polylactic acid (PLA), biodegradable and biocompatible aliphatic polyesters, widely used in medical applications (Fig. 1.4).

Natural biopolymers, on the other hand, consent a wide range of pre-processing functionalization, included cells embedding, due to the low temperature required for their process. Moreover, they can be obtained from industrial wastes, that makes them extremely low cost[15,22,23]. This aspect, though, is also the reason of one of their main drawbacks, that is batch to batch deviations. Being products of extraction, indeed, they might differ due to raw materials variations, and that can significantly affect the downstream process. In addition, they can cause an immune response and they normally require more complex process conditions.

Multiple are the natural biopolymers used in tissue engineering, among which gelatine, a polypeptide derived from collagen hydrolysis, and different polysaccharides like alginate, an edible polysaccharide extracted by brown algae, cellulose, a plant-derived water-insoluble polysaccharide and chitosan, a crustacean-derived polysaccharide (Fig. 1.4).

1.3.5 Gelatine

For this work, after thorough consideration of all the possibilities, gelatine was identified as the best option.

Why gelatine?
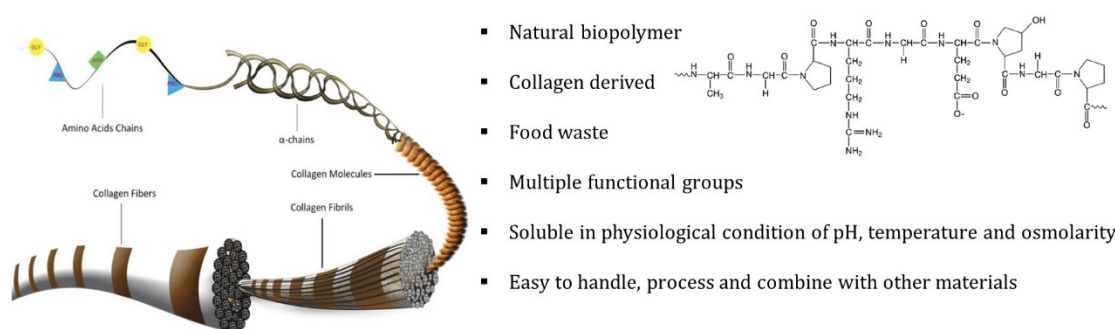
Fig. 1.5 Schematic representation of a collagen fibre structure (left), a gelatine molecule (right) and list of the main advantages of gelatine as biopolymer of election for regenerative medicine (middle).

The ECM, a complex network of collagen, laminin, elastin, and proteoglycans, represents the idealized matrix for which biomaterial researchers take their

inspiration[24] (Fig. 1.5). These proteins and carbohydrates materialize into a robust matrix helped by specific and robust non-covalent interactions that can be described as supramolecular or "beyond the molecule." This kind of molecular assembly and disassembly can occur via reversible bonds such as hydrogen bonding, metal chelation, hydrophobic interactions, π–π interactions, and/or van der Waals interactions[25]. Supramolecular biomaterials have been developed that span from elastomeric polymers, low-molecular-weight hydrogelators to polymeric-based hydrogels. Hydrogels can mimic tissue not only in terms of hydration, sometimes absorbing thousands of times their dry weight in water, and mechanical properties, but also provide a medium for growth factor delivery and support three-dimensional tissue formation[26].

Gelatine is a supramolecular biomaterial that can be exploited for the creation of polymeric-based hydrogels. It belongs to the natural biopolymers family, it is derived by hydrolysis from collagen, the main constituent of extracellular matrix (ECM) in the human body, it is extremely low cost coming from wastes of food industry, presents multiple functional groups, it is soluble in physiological conditions of pH, temperature and osmolarity and it is easy to handle, process and combine with other materials[27–32,33].

1.3.6 Bio-hybrid, biocomposite and bioceramics materials

A biomaterial can be engineered by combining it with functional elements to create a biocomposite material addressing the final purpose, that can be of simple bioconduction or more specifically of bioinduction. While bioconduction implies mainly guide and support the cells, and can be exploited also by a simple biomaterial, bioinduction entail providing cells with the correct cues and stimuli to fulfill the goal[5,28,34].

Trying to provide the most comprehensive and inclusive definition, a biocomposite is a biocompatible material which is produced from two or more constituent materials. These constituent materials have notably dissimilar chemical or physical properties and are merged to create a material with properties unlike the individual elements. When the two components are neither distinguishable nor dissociable it is possible to identify the biocomposite as bio-hybrid material.

Whether one of the constituents is a nature-inspired biomimetic ceramics phase, identified as bioceramics, it is possible to speak of ceramics bio-hybrid or biocomposite materials. Bioceramics phases are designed and realized according to the biomimicry principle, trying to mimic at best the features of the native tissue into which they are thought to be used and are commonly employed as functional elements in bone tissue engineering to booster and lead regeneration towards specific supply of correct physico-chemical and mechanical signals[6,18,35–39].

1.3.7 Biodegradability

The whole design process has finally to consider that the device, to be a device suitable for regenerative medicine, must be biodegradable, meaning partially or completely resorbable in a functional time, reason why the crosslinking method employed to stabilize it in physiological condition as well as the process technology employed to hit the goal must be thoroughly thought[15,21,40,41].

1.4 Three-dimensional printing

By all the process technology possible to exploit in tissue engineering, three-dimensional printing (3D printing), also known as additive manufacturing (AM), solid freeform fabrication (SFF) layered manufacturing (LM) and rapid prototyping (RP) is highly promising. Consisting in the creation of three-dimensional metallic, polymeric, ceramic or composite objects through layer-by-layer deposition guided by a computer aided design (CAD) file, it makes possible to deal with complex geometries and a large variety of materials, it is characterized by high performances and reproducibility and can be exploited for the creation of patient-specific anatomically shaped devices.
Surface features of the three-dimensional CAD files are then exported to a file typically with a .STL extension. The .STL file is the main input file for an AM fabricator where the part is built. The surface file is sliced in a virtual environment into many two-dimensional (2D) layers. An AM machine then uses those 2D layers of the design file and creates the necessary tool-path along the X and Y directions for direct manufacturing. Finally, each layer is processed sequentially one on top of the other to

form a three-dimensional part. Since each part is fabricated by adding layers on top of a previous layer, this type of manufacturing approach is called "additive manufacturing[42] (Fig. 1.6).

1.4.1 Extrusion-based three-dimensional printing
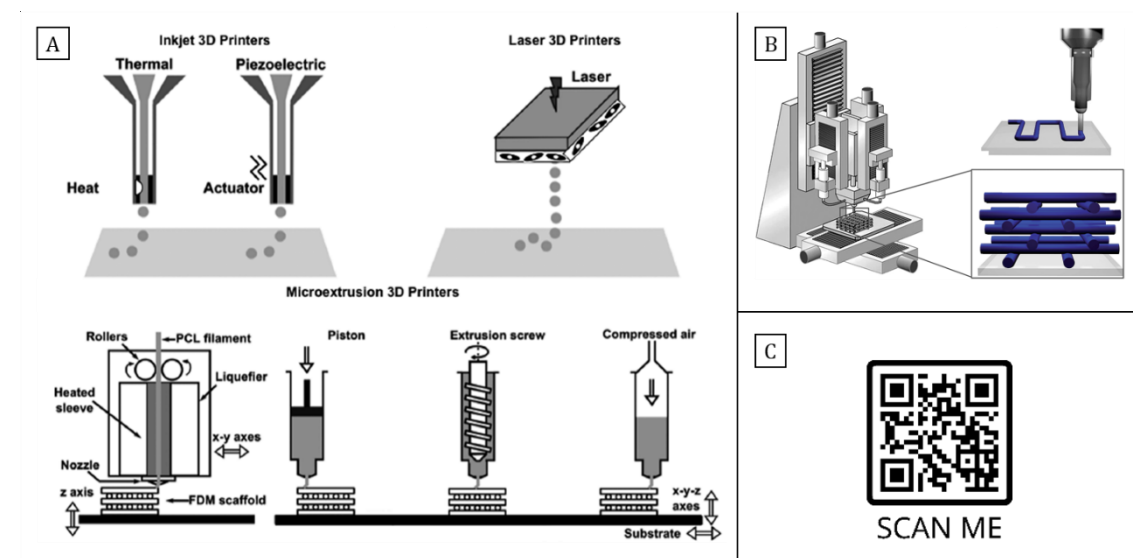
Fig. 1.6 Example of different extrusion-based three-dimensional printing processes (A). Insight in a 3D printed scaffold (B) and live extrusion-based 3D-printing process (C).

Among all the different additive manufacturing techniques, extrusion based three-dimensional printing has attracted increasing attention due to its ability to support low temperature processing and multi-material co-printing, features that have given raise to the development of three-dimensional bioprinting, meaning the three-dimensional printing of "living inks" normally known as bioinks, containing, besides the matrix, cells and biomolecules, which is currently continuously opening new frontiers in regenerative medicine.

1.4.2 Bioprinting
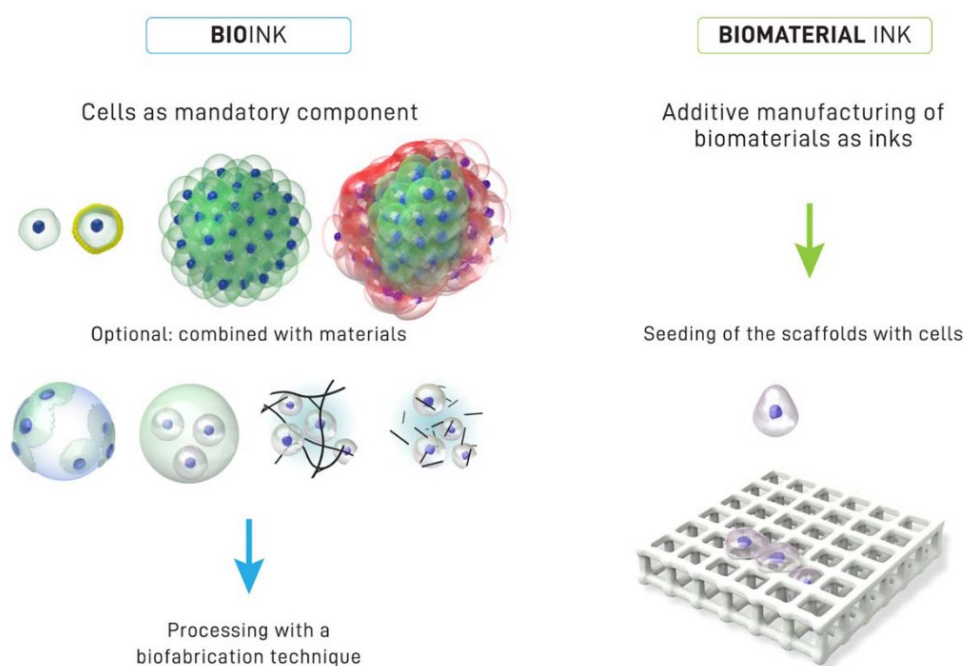
Fig. 1.7 Schematic representation of the differences between a bioink and a biomaterial ink (from *A definition of bioinks and their distinction from biomaterial inks*, Groll 2019).

Three-dimensional bioprinting involves the creation of living dynamic functional structures with the aim of regenerating a specific target tissue, exploiting a predesign precise deposition of bioinks. A bioink can be defined as an ink where cells are a mandatory component of the printing formulation in the form of single cells, coated cells and cell aggregates of one or several cell types, or in combination with materials, for example seeded onto microcarriers, embedded in microgels, formulated in a physical hydrogel, or formulated with hydrogel precursor.

Diversely, a biomaterial ink is made of a biomaterial used for printing and cell-contact occurs only post-fabrication. Bioprinting is rapid and inexpensive and allows to generate geometrically well-defined scaffolds with precise control over the composition in terms of cells and biomaterials, associated with spatial distribution, and architectural accuracy. Moreover, its ability for precise placement of high-density cells in the desired location and multiple types of cells in an orderly fashion can be exploited to mimic the heterogeneous architectures of the targeted native tissue.

Current three-dimensional bioprinting technologies for engineering functional human tissues and organs that recapitulate their native prototypes can be categorized based on four major classes: droplet-based, extrusion-based, laser-induced forward transfer, and stereolithography bioprinting.

Among these, one of the most interesting and explored techniques is extrusion-based bioprinting (EBB), which extrudes or dispenses continuous strands or fibres of biomaterials to form 3D scaffold structures in a layer-by-layer manner. The main advantages of EBB compared to other 3D printing methods consist in producing tissue scaffolds using a wide variety of biomaterials and cell types, even hydrogel polymers with suspended cells; allowing layer-by-layer deposition of biomaterials with physiological cell density in a designed way, presenting a relatively less process-induced cell damage compared to other techniques, and having great potential for regulating and conducting stem cell growth and differentiation for many applications. Despite some challenges such as limited strand resolution (typically greater than 100 μm) and restricted biomaterials choice, the stated advantages associated with economical aspects and commercial availability have made EBB the most popular technique amongst tissue engineers and researchers[43].

References

1.   Asghari, F., Samiei, M., Adibkia, K., Akbarzadeh, A. & Davaran, S. Biodegradable and biocompatible polymers for tissue engineering application: a review. *Artif. Cells, Nanomedicine Biotechnol.* **45**, 185–192 (2017).

2.   Cui, W., Zhou, Y. & Chang, J. Electrospun nanofibrous materials for tissue engineering and drug delivery. *Sci. Technol. Adv. Mater.* **11**, 014108 (2010).

3.   Walmsley, G. G. *et al.* Nanotechnology in bone tissue engineering. *Nanomedicine Nanotechnology, Biol. Med.* **11**, 1253–1263 (2015).

4.   Abdulghani, S. & Mitchell, G. R. Biomaterials for in situ tissue regeneration: A review. *Biomolecules* **9**, (2019).

5.   Pina, S. *et al.* Regenerative Medicine Applications. *Materials (Basel).* **12**, 1824 (2019).

6.   Zhou, H. & Lee, J. Nanoscale hydroxyapatite particles for bone tissue engineering. *Acta Biomater.* **7**, 2769–2781 (2011).

7.   Owen, S. C. & Shoichet, M. S. Design of three-dimensional biomimetic scaffolds. *J. Biomed. Mater. Res. - Part A* **94**, 1321–1331 (2010).

8.   Bačáková, L., Novotná, K. & Pařzek, M. Polysaccharides as cell carriers for tissue engineering: The use of cellulose in vascular wall reconstruction. *Physiol. Res.* **63**, (2014).

9.   Hwang, J. *et al.* Biomimetics: Forecasting the future of science, engineering, and medicine. *Int. J. Nanomedicine* **10**, 5701–5713 (2015).

10. Sprio, S. *et al. Biomimetic materials in regenerative medicine. Biomimetic Biomaterials: Structure and Applications* (Woodhead Publishing Limited, 2013). doi:10.1533/9780857098887.1.3.

11. Krogsgaard, M., Nue, V. & Birkedal, H. Mussel-Inspired Materials: Self-Healing through Coordination Chemistry. *Chem. - A Eur. J.* **22**, 844–857 (2016).

12. Liu, Y., He, K., Chen, G., Leow, W. R. & Chen, X. Nature-Inspired Structural Materials for Flexible Electronic Devices. *Chem. Rev.* **117**, 12893–12941

(2017).

13. Shao, Y. *et al.* Shape memory superhydrophobic surface with switchable transition between "Lotus Effect" to "Rose Petal Effect". *Chem. Eng. J.* **382**, 122989 (2020).

14. Liu, K., Du, J., Wu, J. & Jiang, L. Superhydrophobic gecko feet with high adhesive forces towards water and their bio-inspired materials. *Nanoscale* **4**, 768–772 (2012).

15. Pina, S., Oliveira, J. M. & Reis, R. L. Natural-based nanocomposites for bone tissue engineering and regenerative medicine: A review. *Adv. Mater.* **27**, 1143–1169 (2015).

16. Elsharkawy, S. & Mata, A. Hierarchical Biomineralization: from Nature's Designs to Synthetic Materials for Regenerative Medicine and Dentistry. *Adv. Healthc. Mater.* **7**, 1–19 (2018).

17. Saunders, B. E. A biomimetic study of natural attachment mechanisms— Arctium minus part 1. *Robot. Biomimetics* **2**, (2015).

18. Witte, F., Bartsch, I. & Willbold, E. Designing the biocompatibility of biohybrids. *Adv. Biochem. Eng. Biotechnol.* **126**, 285–296 (2012).

19. Festas, A. J., Ramos, A. & Davim, J. P. Medical devices biomaterials – A review. *Proc. Inst. Mech. Eng. Part L J. Mater. Des. Appl.* **234**, 218–228 (2020).

20. Liu, X., Holzwarth, J. M. & Ma, P. X. Functionalized Synthetic Biodegradable Polymer Scaffolds for Tissue Engineering. *Macromol. Biosci.* **12**, 911–919 (2012).

21. Tian, H., Tang, Z., Zhuang, X., Chen, X. & Jing, X. Biodegradable synthetic polymers: Preparation, functionalization and biomedical application. *Prog. Polym. Sci.* **37**, 237–280 (2012).

22. Bharadwaz, A. & Jayasuriya, A. C. Recent trends in the application of widely used natural and synthetic polymer nanocomposites in bone tissue regeneration. *Mater. Sci. Eng. C* **110**, 110698 (2020).

23. Murphy, C. A. *et al.* Biopolymers and polymers in the search of alternative

treatments for meniscal regeneration: State of the art and future trends. *Appl. Mater. Today* **12**, 51–71 (2018).

24. Frantz, C., Stewart, K. M. & Weaver, V. M. The extracellular matrix at a glance. *J. Cell Sci.* **123**, 4195–4200 (2010).

25. Seiffert, S. & Sprakel, J. Physical chemistry of supramolecular polymer networks. *Chem. Soc. Rev.* **41**, 909–930 (2012).

26. Feliciano, A. J., van Blitterswijk, C., Moroni, L. & Baker, M. B. Realizing tissue integration with supramolecular hydrogels. *Acta Biomater.* **124**, 1–14 (2021).

27. Spencer, A. R. *et al.* Bioprinting of a Cell-Laden Conductive Hydrogel Composite. *ACS Appl. Mater. Interfaces* **11**, 30518–30533 (2019).

28. Pacelli, S., Basu, S., Berkland, C., Wang, J. & Paul, A. Design of a Cytocompatible Hydrogel Coating to Modulate Properties of Ceramic-Based Scaffolds for Bone Repair. *Cell. Mol. Bioeng.* **11**, 211–217 (2018).

29. Martínez-Vázquez, F. J., Cabañas, M. V., Paris, J. L., Lozano, D. & Vallet-Regí, M. Fabrication of novel Si-doped hydroxyapatite/gelatine scaffolds by rapid prototyping for drug delivery and bone regeneration. *Acta Biomater.* **15**, 200–209 (2015).

30. Campodoni, E. *et al.* Mimicking Natural Microenvironments: Design of 3D-Aligned Hybrid Scaffold for Dentin Regeneration. *Front. Bioeng. Biotechnol.* **8**, 1–12 (2020).

31. Campodoni, E. *et al.* Polymeric 3D scaffolds for tissue regeneration: Evaluation of biopolymer nanocomposite reinforced with cellulose nanofibrils. *Mater. Sci. Eng. C* **94**, 867–878 (2019).

32. Panseri, S. *et al.* Biomimetic scaffold with aligned microporosity designed for dentin regeneration. *Front. Bioeng. Biotechnol.* **4**, 1–8 (2016).

33. Bello, A. B., Kim, D., Kim, D., Park, H. & Lee, S. H. Engineering and functionalization of gelatine biomaterials: From cell culture to medical applications. *Tissue Eng. - Part B Rev.* **26**, 164–180 (2020).

34. Catoira, M. C., Fusaro, L., Di Francesco, D., Ramella, M. & Boccafoschi, F.

Overview of natural hydrogels for regenerative medicine applications. *J. Mater. Sci. Mater. Med.* **30**, (2019).

35. Agbeboh, N. I. *et al.* Environmentally sustainable processes for the synthesis of hydroxyapatite. *Heliyon* **6**, e03765 (2020).

36. Simchi, A., Tamjid, E., Pishbin, F. & Boccaccini, A. R. Recent progress in inorganic and composite coatings with bactericidal capability for orthopaedic applications. *Nanomedicine Nanotechnology, Biol. Med.* **7**, 22–39 (2011).

37. Du, Y., Guo, J. L., Wang, J., Mikos, A. G. & Zhang, S. Hierarchically designed bone scaffolds: From internal cues to external stimuli. *Biomaterials* **218**, 119334 (2019).

38. Heness, G. & Ben-Nissan, B. Innovative bioceramics. *Mater. Forum* **27**, 104–114 (2004).

39. Campodoni, E. *et al.* Blending gelatine and cellulose nanofibrils: Biocomposites with tunable degradability and mechanical behavior. *Nanomaterials* **10**, 1–18 (2020).

40. Fernandez-Yague, M. A. *et al.* Biomimetic approaches in bone tissue engineering: Integrating biological and physicomechanical strategies. *Adv. Drug Deliv. Rev.* **84**, 1–29 (2015).

41. Xu, H., Casillas, J., Krishnamoorthy, S. & Xu, C. Effects of Irgacure 2959 and lithium phenyl-2,4,6-trimethylbenzoylphosphinate on cell viability, physical properties, and microstructure in 3D bioprinting of vascular-like constructs. *Biomed. Mater.* **15**, (2020).

42. Bose, S., Ke, D., Sahasrabudhe, H. & Bandyopadhyay, A. Additive manufacturing of biomaterials. *Prog. Mater. Sci.* **93**, 45–111 (2018).

43. Askari, M. *et al.* Recent progress in extrusion 3D bioprinting of hydrogel biomaterials for tissue regeneration: A comprehensive review with focus on advanced fabrication techniques. *Biomater. Sci.* **9**, 535–573 (2021).

CHAPTER 2

Additive-free gelatine-based devices for chondral tissue regeneration: technological process comparison among mould casting and three-dimensional extrusion-based printing

2.1 Introduction

In the human body chondral tissue has a structural and protection role. It is made of an extra-cellular matrix (ECM) mainly composed of collagen, proteoglycans and glycosaminoglicans populated by chondrocytes and chondroblasts, the two main cells type of the chondral tissue. It doesn't have blood vessels or nerves and nutrients and wastes are exchanged by diffusion. This traduces in a very slow turnover of the tissue.

The spread of cartilage injuries combined with their often-asymptomatic origin and the lack of intrinsic chondral tissue healing capacity make chondral regeneration a significant clinical challenge[1,2–5]. Many are the key points to consider when designing a tissue-to-be capable to reveal full biocompatibility, gradual resorbability, suitable mechanical properties and fine control of the inner and outer geometry resulting in a proper porosity[6,7]. It has been proven how a thorough design of the material composition and geometry can deeply influence the final device properties even arriving to lead and govern cells behaviour only by means of the mechanical and geometrical stimuli provided to them[3,8,9,10].

To this end, being able to design and develop a directly implantable biomaterial capable to *in-situ* elegantly direct cells spreading and growth in virtue of its mere composition, geometric structure and mechanical properties results to be of great appeal[7]. In this context, three-dimensional (3D) printing has recently been pointed out as the step-forward, compared to the well-known and commonly used mould casting technique, towards a better design and control of the desired regenerative material[6,11,12].

As reported by Ligon and collaborators[7], conventional techniques of scaffold fabrication such as phase inversion, solvent casting, solute leaching and

electrospinning often lack in the ability to incorporate fine internal architectural details and controlled porosity while ensuring reproducibility. Especially in tissue engineering, where the need for patient-specific medical devices is increasing, 3D printing looms as an interesting option by addressing these issues through a precise regulation of pore sizes and their uniform distribution throughout the scaffold[11,13,14]. Nevertheless, together with many advantages allowed by this technology, like precise control of the outer shape and inner geometry, come also different challenging aspects that need to be faced and overcome. Among these, the operating conditions (as nozzle diameter, extrusion rate, printing temperature) together with material-related factors like gel rheology[15,16,17–19]. For load-bearing tissues it is important to understand the correlations between structure and function to define tissue engineering design criteria. The viscoelastic properties of cartilage derives from its extracellular matrix (ECM) composition that is made of water, collagen, and glycosaminoglycans[4,20].
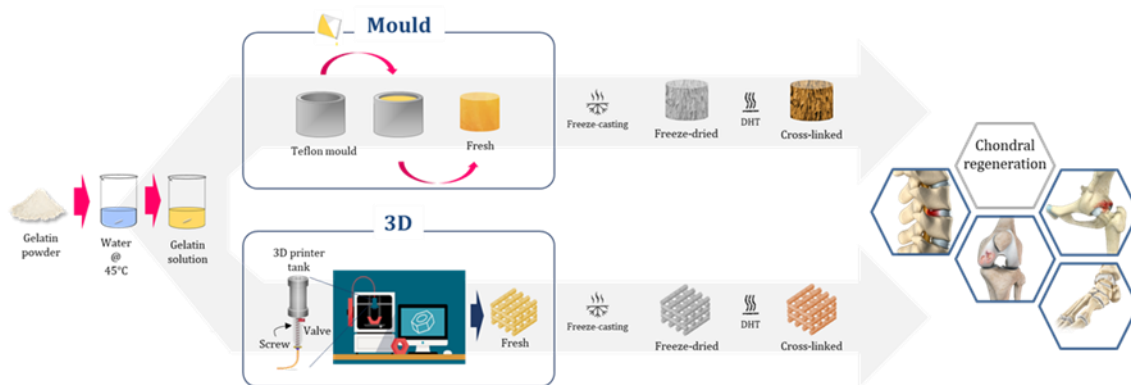
Fig. 2.1 Workflow of the two technological processes realized. The same gelatine slurry was processed by mould casting (up) and 3D printing (down), the realized scaffolds freeze-casted and crosslinked by dehydro-thermal treatment (DHT).

Starting from considering the above-mentioned features but keeping in mind the ongoing difficulties related to collagen printing, mainly due to its fibrous nature, we decided to opt for printing gelatine, a collagen-derived biopolymer with proven biocompatibility, trying to process it as-is, *i.e.*, without the addiction of any additive or crosslinker, nor during the processing nor post-processing steps. We focused, indeed, on the creation of a totally additive-free ink and 3D printed material, playing

with the ink composition and process condition and taking advantage of the physical crosslinking for the reticulation step[2,21], in order to reach the goal.

Within this work we addressed chondral regeneration by processing with two different technological processes, 3D printing and mould casting (Fig. 2.1), the same additive-free gelatine-based ink to develop scaffolds potentially suitable for chondral tissue engineering, carrying out a rheological, morphological, chemico-physical, mechanical and biological comparison among the resulting products in order to determine their potential suitability for *in-situ* chondral regeneration.

2.2 Materials and methods

2.2.1 Gel solution

Gelatine (Gel) powder with mesh 4 and bloom 280, extracted from pig skin, was received by Italgelatine (Italy). Gel aqueous solutions at different concentrations were prepared by dissolving Gel powder in ultra-pure water (0,055 µS/cm, 25 °C) at 45 °C under strong and constant magnetic stirring, till perfectly homogeneous and transparent solutions were obtained. In particular, for the 3D printing, three different Gel aqueous solutions of 90 mg/mL (Gel90), 120 mg/mL (Gel120) and 150 mg/mL (Gel150) were prepared. To make the 3D printed scaffold comparable with the mould casted, the concentrations of the seconds were adjusted considering the infill rate of the 3D printed scaffold to which they were going to be compared, as reported in Tab.2.1. In fact, as the infill rate of the 3D printed samples is not of 100% as for the mould casted samples, due to the reticulated structure generated, in order to make comparisons with the same amount of gelatine in the samples (for samples with the same apparent volume) the concentrations of the solutions for mould casting has been reduced by multiplying the concentration of the 3D printing solution for the corresponding infill rate. In the following, the codes of the samples referred to the 3D printing solution will be kept also for the mould casting solution even if for them the infill rates and the concentrations are different. The Gel solutions prepared at 45°C become viscoelastic solid-like gels once let cool down at 25°C.

Tab. 2.1 Gel solutions concentrations for the realization, respectively, of the 3D printed and mould casted scaffolds. The mould casting solutions were adapted considering the 3D printed scaffolds infill.

CODE	3D printing		Mould casting	
	Infill rate	Solution concentration	Infill rate	Solution concentration
Gel90 f50	50%	90 mg/mL	100%	45 mg/mL
Gel90 f70	70%		100%	63 mg/mL
Gel120 f50	50%	120 mg/mL	100%	60 mg/mL
Gel120 f70	70%		100%	84 mg/mL
Gel150 f50	50%	150 mg/mL	100%	75 mg/mL
Gel150 f70	70%		100%	105 mg/mL

2.2.2 Rheology

The rheological behaviour of the Gel solutions was investigated at 45 °C by measuring their viscosity with a ramp test in controlled stress mode and at 25 °C, when they are in the gel state, by measuring their viscoelastic properties with small amplitude oscillation shear (SAOS) tests. All the measurements were performed with a rotational rheometer (C-VOR 120, Bohlin Instruments, UK). The ramp test was performed using a cone/plate CP4/40 (Ø = 40 mm, conicity = 4 °) geometry by increasing the shear stress from 0.05 Pa up to 10 Pa with a sweep time of 300 s. Before to start the test, the samples were let at rest for 3 min to reduce possible influence on the measurement induced by the solutions handling. Such measurements were performed using a solvent trap to avoid water evaporation during the test. Amplitude and frequency sweep tests were carried out using a plate/plate PP20 (Ø = 20 mm) geometry with a large gap of 6 mm. The amplitude sweep tests were conducted by applying stresses ranging from 0,1 Pa up to $5,73 \cdot 10^4$ Pa at the frequency of 1 Hz, while the frequency sweep test was conducted by decreasing the frequency from 10 to 0,01 Hz with an applied constant stress of 5 Pa that in each case resulted to be inside the linear viscoelastic region (LVER). Paraffin oil with low viscosity (Carlo Erba) to cover

the edges in contact with air was used to prevent the samples from drying out during the viscoelastic measurements.

2.2.3 Scaffold shaping processes

Mould-casted scaffolds were obtained by pouring the obtained Gel solutions in Ø= 6 mm and h= 6 mm polytetrafluoroethylene (PTFE) moulds that were then freeze-casted. The freeze-casting process consisted of a pre-freezing step with a controlled freezing ramp of 50 °C/h down to -40 °C, followed by two heating ramps, respectively of 5 °C/h from -40 °C to -5 °C and of 3 °C/h up to 20 °C. The whole process was carried out under vacuum (P=0.086 mbar). Finally, the scaffolds were crosslinked by means of a dehydrothermal (DHT) treatment performed for 48 h in a vacuum oven at 160 °C with a pressure of 10^{-2} mbar[22,23,24,25].

The 3D scaffolds design was performed by using a dedicated parametric three-dimensional drawing and design software. Then, to produce the real objects, a slicing software was used. 3D printed scaffolds were obtained by employing the Gel solutions as inks for a screw extrusion-based 3D printer (DeltaWasp 2040, Wasp, Italy). Each solution was poured, at 45°C, in an 81 mL (Ø= 4 cm; h= 6,5 cm) steel sink and let cool down to room temperature overnight to allow the complete gelation. The whole extrusion process was carried out at room temperature (25 °C) at 3,5 bar pressure. For the scaffolds realization, the 3D printer was equipped with a Ø= 0,41 mm conic nozzle. The as-produced 3D printed scaffolds were then freeze-dried and crosslinked by DHT treatment following the same protocols previously reported for the mould-casted scaffolds and next punched to obtain 6 mm diameter and 6 mm height cylindrical samples.

2.2.4 Morphological characterization

Scaffolds morphology was evaluated through environmental scanning electron microscopy (ESEM, Quanta 600 FEG, FEI Company, Hillsboro, OR) and digital optical microscopy (Hirox RH-2000, 3D Digital Microscope, Hirox Europe). Samples for ESEM observations were prepared by fixing the scaffolds onto aluminium stubs by means of

carbon tape and then applying an Au coating by sputtering (QT150T, Quorum Technologies Ltd, UK).

Scaffolds total and macro porosities were assessed by means of density-based and water-squeezing methods, respectively[3,26]. With the first method, the scaffolds total porosity was determined based on their weight, apparent (i.e. geometric) volume and theoretical density. In particular, the apparent density (ρ_a) of the cylindrical scaffolds was calculated through the equation:

$$\rho_a = \frac{W}{\pi \times \left(\frac{D}{2}\right)^2 \times H}$$

where W is the dry scaffold weight, D the diameter and H the height. The obtained ρ_a was then divided by the material theoretical density (ρ_t), *i.e.* the density of the gelatine, and the ratio inserted in the equation that gives the total porosity:

$$Total\ porosity_\% = 100 - \left(\frac{\rho_a}{\rho_t} \times 100\right)$$

with a replicate number of three (n= 3) and values expressed as mean ± standard error.

The water-squeezing method was instead used to assess the macro-porosity by measuring the water amount absorbed by the scaffold before and after squeezing. Since the water contained into macro pores is more easily released than the one contained into micro pores, an evaluation of the macro pores volume percentage could be made as (assuming 1 g/mL for the water density):

$$Macropores\ volume_\% = \frac{W_{swollen} - W_{squeezed}}{W_{swollen}} \times 100$$

To perform the test, scaffolds were soaked in phosphate buffered saline (PBS) (Sigma Aldrich, Saint Louis, Missouri, USA), rather than water, at 37°C for one hour before to be weighed ($W_{swollen}$), squeezed and weighed again ($W_{squeezed}$).

2.2.5 Chemico-physical characterization

Swelling test[26,3,27] was performed by soaking the samples in PBS solution with 0,1% w/v of NaN$_3$ at 37 °C under shaking and weighing the swollen samples at different

times (0,5; 1,5; 3; 6; 24; 48 h) after letting them rest for a matter of second on a non-absorbent surface. The swelling ratio (S_r) was calculated as:

$$S_r = \frac{W_{swollen} - W}{W}$$

where $W_{swollen}$ was the swollen sample weight and W the dry sample weight before the soaking.

Degradation[26] test was performed by soaking the samples in a PBS solution with 0,1% w/v NaN$_3$ at 37 °C under shaking, as for the swelling test, taking out them from the medium at regular time intervals (at 7 and 21 days), washing them three times in milliQ water and freeze-drying. Samples where then weighed and degradation ratio ($D_{\%}$) calculated as:

$$D_{\%} = \frac{W - W_f}{W_f} \times 100$$

where W was the dried sample initial weight while W_f was the freeze-dried sample weight at a specific time point.

2.2.6 Mechanical characterization

The scaffolds mechanical properties were evaluated by using a dynamic mechanical analyser Q800 (TA Instruments, IT) in uniaxial submersion-compression mode. Measurements were carried out in submersion in PBS at 37 °C and tests performed after sample overnight immersion in PBS at 37 °C under shaking. Prior to start the measurement, a preload force of 10^{-4} N was always applied to the sample to ensure the entire scaffold surface was properly in contact with the compression plate.

The Young's modulus was evaluated by means of a stress-strain test[26,3] consisting in an isothermal period of 5 min at 37 °C followed by a force ramp rate of 0,1 N/min from 0 N to 1 N, then a force ramp rate of 0,5 N/min from 1 N to 5 N to end with a force ramp rate of 1 N/min from 5 N to 18 N.

A creep test[26,3] was carried out to evaluate the recovery ability of the samples. The analysis was performed at 37 °C in submersion, with a creep time of 15 min, a recovery time of 15 min and an applied stress of $6 \cdot 10^{-2}$ MPa.

The viscoelastic behaviour of the scaffold was assessed by means of a multifrequency test[26], performed in submersion at 37 °C in a frequency range from 1 to 10 Hz, at a constant amplitude of 75 µm (n = 5).

2.2.7 Preliminary biological study

Human Chondrocytes cell line (CHON-002) purchased from American Type Culture Collection (ATCC® CRL™-2847) were cultured in standard medium composed by Dulbecco's Modified Eagle Medium/F-12 Nutrient Mixture (DMEM/F-12) with Glutamine (GlutaMAX) (Gibco), supplemented with 10% Foetal Bovine Serum (FBS) and 0,1 mg/mL G418 Sulphate (50 mg/mL) (Gibco). The cultures were kept in incubator at 37 °C, 5% CO_2 atmosphere and controlled humidity conditions. The cells were detached from culture flasks by trypsinization and centrifugated. The cell number and viability were defined with Trypan Blue Dye Exclusion test.

Both Gel120 f70 mould casted and 3D printed scaffolds, 6 mm height and 6 mm diameter, sterilized by γ-ray irradiation (25 kGy), were pre-soaked in culture medium for 24 hours before seeding ~ $2{,}5\cdot10^4$ cells/scaffold by carefully dropping 20 µL of cell suspension on each scaffold upper surface. After allowing cell adhesion for 30 minutes, 1,5 mL/well of culture medium was added to the scaffolds and gently changed every 2-3 days. The cultures were kept for 7 days at 37 °C with 5% CO_2 atmosphere and controlled humidity conditions. All cell handling procedures were performed under laminar flow hood and in sterility conditions.

Quantitative cell viability and proliferation analysis was performed via MTT Assay[28,29]. In detail, MTT reagent [3-(4,5-dimethylthiazol-2-yl)-2,5-diphenyltetrazolium bromide] was firstly dissolved in PBS 1X (5 mg/mL). The scaffolds were incubated with 10% well-volume MTT solution for 2 hours at 37 °C and 5% CO_2 atmosphere conditions. Later, each scaffold was incubated with dimethyl sulfoxide for 15 min. In this assay, the metabolically active cells react with the tetrazolium salt in the MTT reagent to produce a formazan dye that can be observed at λ_{max} of 570 nm, using a Multiskan FC Microplate Photometer (Thermo Scientific). This absorbance is directly proportional to the number of metabolically active cells. For each type of material, two scaffolds were analysed at each time point (1, 3 and 7 days of culture). Results were expressed as Mean ± Standard Error of the Mean plotted

on graph. Statistical analysis was made by two-way ANOVA analysis of variance followed by Sidak's multiple comparisons test by the GraphPad Prism software (version 6.0), with statistical significance set at p ≤ 0,05.

Qualitative cell viability was analysed by Live/Dead assay kit (Invitrogen) according to manufacturer's instructions[28,29,30]. Briefly, the samples were washed with PBS 1x for 5 min and incubated with Calceinacetoxymethyl (Calcein AM) 2 µM plus Ethidium homodimer-1 (EthD-1) 4 µM for 15 min at 37 °C in the dark, the samples were rinsed in PBS 1x. Images were acquired by an inverted Nikon Ti-E fluorescence microscope (Nikon). One sample per group was analysed at D1 and D3.

An additional qualitative analysis to highlight the scaffold colonization by the cells was performed by cell nuclei detection. Briefly the scaffolds were washed in PBS 1X for 5 minutes and fixed in 4% (w/v) paraformaldehyde (PFA) (Sigma) for 15 minutes. 4'-6-diamidino-2-phenylindole (DAPI) (Invitrogen, 600 nM) staining was performed to highlight cell nuclei[31]. The samples were visualized with inverted Ti-E fluorescence microscope (Nikon). One sample per group was analysed at D1, D3 and D7.

2.3 Results and discussion

2.3.1 Rheology of Gel solutions

Gel solutions at different concentrations were prepared by dissolving gelatine powder in ultrapure water at 45 °C under vigorous magnetic stirring, till the obtainment of perfectly homogeneous and transparent solutions. Three different concentrations (90, 120, and 150 mg/mL) were chosen for the realization of 3D printed scaffolds, then adapted for the mould casting as described in Tab.1. These concentrations were chosen for the potential printability features like good extrudability, acceptable filament swelling, proper model fidelity and shape maintenance.

The rheological properties of 3D printing inks are crucial for the success of the process. They affect the printability, performance, and results of the print[32,33]. The rheological behavior of the three Gel solutions, Gel90, Gel120 and Gel150, was evaluated both as liquid at 45 °C with a viscosity test and, since the printing process was designed to be operated at room temperature, as solid hydrogels at 25 °C with amplitude and frequency sweep tests. The latter were performed to evaluate their viscoelastic properties like the dynamic complex modulus G^* and the loss angle δ derived from the combination of elastic (storage) modulus G' and viscous (loss) modulus G''.

Through the viscosity test performed at 45°C, the Newtonian behavior of all the Gel solutions was assessed. Moreover, a substantial increment in the Gel150 dynamic viscosity in respect to Gel90 and Gel120 was recorded (Fig. 2.2). The dynamic viscosity increases from 15,7 mPa·s for Gel90, to 20,7 mPa·s for Gel120, to 33,4 mPa·s for Gel150, with a non-linear trend with respect to concentration (see inset in Fig. 2.2).
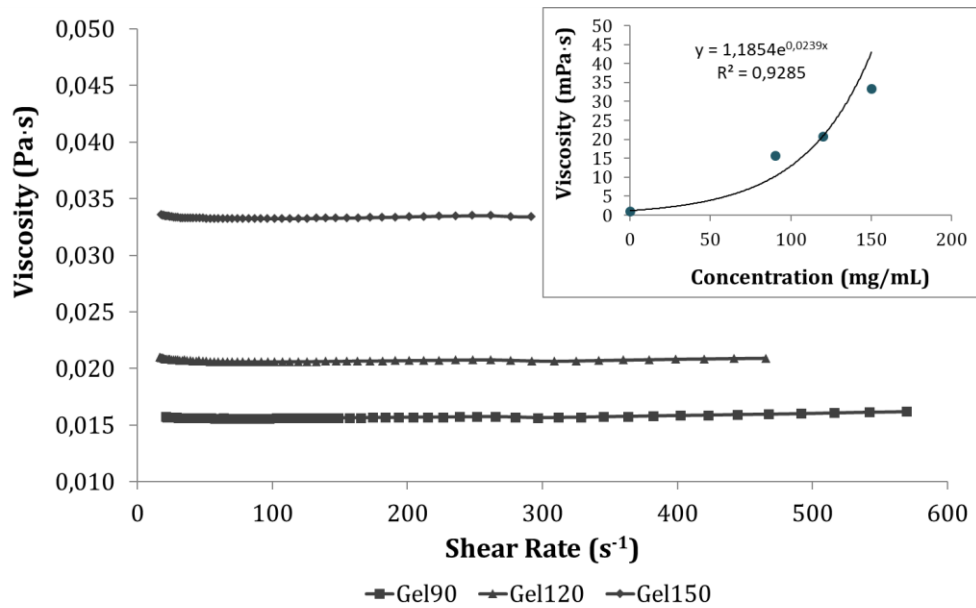
Fig. 2.2 Demonstration of the three different Gel solutions Newtonian behaviour, tested at 45°C; in the inset is shown the non-linear increase of viscosity with the concentration.

The amplitude sweep test and the frequency sweep test (Fig. 2.3) were performed on the solid hydrogels at 25 °C, in order to evaluate their complex modulus G^* ($G^* = G' + iG''$) and loss angles. The amplitude stress sweep test at 1 Hz shows that all the three gels remain in the linear viscoelastic region up to almost 500 Pa. For each Gel, the elastic modulus is almost an order of magnitude higher than the viscous one, and their values increases with the concentration of gelatine, consistently with the viscosity. For the most concentrated sample (Gel150) the elastic modulus is about 7 kPa, that resulted to be a value excessively high for the 3D printing process, while the value of 2,2 kPa of Gel120 and of 1,5 kPa of Gel90 resulted to be suitable for the application.
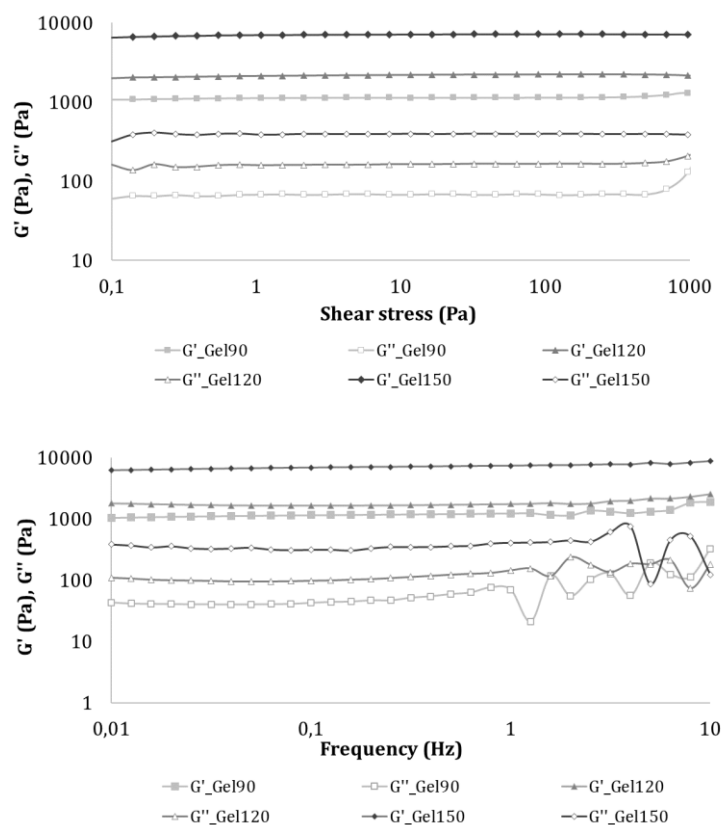
Fig. 2.3 Amplitude stress sweep tests at 1 Hz (up) and frequency sweep tests (down) for the three gels at 25°C.

To be conservative, the frequency sweep test was conducted keeping the shear stress fixed at 5 Pa for all the frequencies investigated. Such test shows that the two moduli are almost constant with the frequency, as expected for hydrogels. In addition, they allowed us to confirm the prevalence of the elastic component on the viscous one of the Gel solutions in the gel state and to assess a non-linear dependence of viscosity and G* values on Gel solutions concentration. Indeed, to a linear increment of the gel concentration from Gel90 to Gel150, a significant higher increase in viscosity and G* values passing from Gel120 to Gel150 was recorded, with resulting strongly different performances in terms of extrusion. Based on the rheology results and after preliminary extrusion test on the obtained Gel solutions, due to its extremely difficult printability, in line with its rheological behaviour, Gel150 was ruled out from further experiments, thus only Gel90 and Gel120 were used in the scaffold shaping processes.

2.3.2 Scaffolds shaping processes

Mould-casted scaffolds were obtained by pouring the as-obtained Gel solutions in Ø=6 mm PTFE moulds, then freeze-casted. PTFE was chosen among all the possible materials thanks to its extremely low friction coefficient, non-reactive nature and good thermal conductivity[34], in order to allow a good directional freeze-casting of the Gel solutions, not influenced by any possible interaction with the mould, nor chemical or physical, and with an effective conduction of the heat exchange during the whole process. Strictly controlling the freezing and heating ramps rate and time of the freeze casting is indeed possible to control and direct size, shape and orientation of the ice crystals, meant to be the pores within the material, thus controlling the final scaffold morphology[22,23,24]. The whole freeze casting process of the Gel mould casted scaffolds was designed to obtain a final structure characterized by ordered longitudinal aligned pores[28].

The 3D scaffolds design was performed by using a dedicated parametric three-dimensional drawing and design software, combined with a slicing software for the concrete production of the obtained virtual object. Since the realization of a 3D printing scaffold made just of gelatine, without any extra crosslinker or additive, requires the printing of full borders around the main geometrical structure to support and anchor it, we opted for printing a Ø=35 mm and h=10 mm cylindrical scaffold from which Ø=6 mm and h=6 mm cylindrical scaffolds were carefully cut out. This approach, aimed at excluding the border contribution, was pursued to better compare the mesh, infill rate and Gel solution concentration of the 3D samples versus the corresponding mould casted same-sized samples.

For the printing process, 25 °C printing temperature combined with an extrusion pressure of 3,5 bar and a Ø=0,41 mm tip was selected as the best conditions, able to combine a precise, constant, and continuous material flow, shape maintenance and model fidelity with an extremely simple and low-cost process. Higher printing temperatures resulted in a total loss of shape maintenance, while higher extrusion pressures resulted in an excessive swelling of the printing filament with a consequent strong loss in model fidelity. A tip of Ø =0,41 mm was selected as the best dimension to ensure high resolution printing while dealing with all the previous cited parameters. Different infill percentages, ranging from 50% to 70%, with a reticuled

mesh were chosen to be further investigated. From some preliminary tests (data not shown), going down to less than 50% of infill was indeed proven to be useless, since the pore dimension resulted to be excessive to promote any cell colonization, while, on the contrary, going up to more than 70% of infill was proven to be pointless since the model fidelity would be extremely decreased after freeze-casting, because of the excessive closeness of the filaments (data not shown). The 3D printed scaffolds were then freeze casted at the same conditions of the previously reported mould casted ones.

Since our interest was in assessing the potential differences in terms of physical, chemical, mechanical and biological properties of gelatine processed by 3D printing and mould casting, to improve the chemical stability and preserve the mechanical performance of the produced scaffolds in wet conditions, a physical crosslinking procedure, named dehydro-thermal (DHT) treatment, was selected. This, to improve their behaviour in physiological environments without adding any extra components, and thus variables, to the pure polymer. DHT treatment is widely implied in reticulation of collagen and collagen-derivatives like gelatine, with demonstrated improvements on their stability and mechanical properties, if well balanced with the treatment-related polymer degradation unavoidably occurring at the pressure and temperature required for the successful crosslinking of the material[35,36,2]. Accordingly with literature, the parameters for the crosslinking of both the 3D printed and mould casted scaffolds were then set at 48 h in a vacuum oven at 160 °C with a pressure of 10^{-2} mbar[2,35,36].

2.3.3 Morphological characterization

Morphological characterizations were performed on the resulting scaffolds, after freeze-casting and DHT, aiming to determine the outcomes of the two different shaping processes. Due to the different dimensions of their most relevant morphological features, such as pores shape and dimension, two different characterizations techniques were used to highlight them: ESEM for the mould casted samples and optical microscopy for the 3D printed ones (Fig. 2.4).
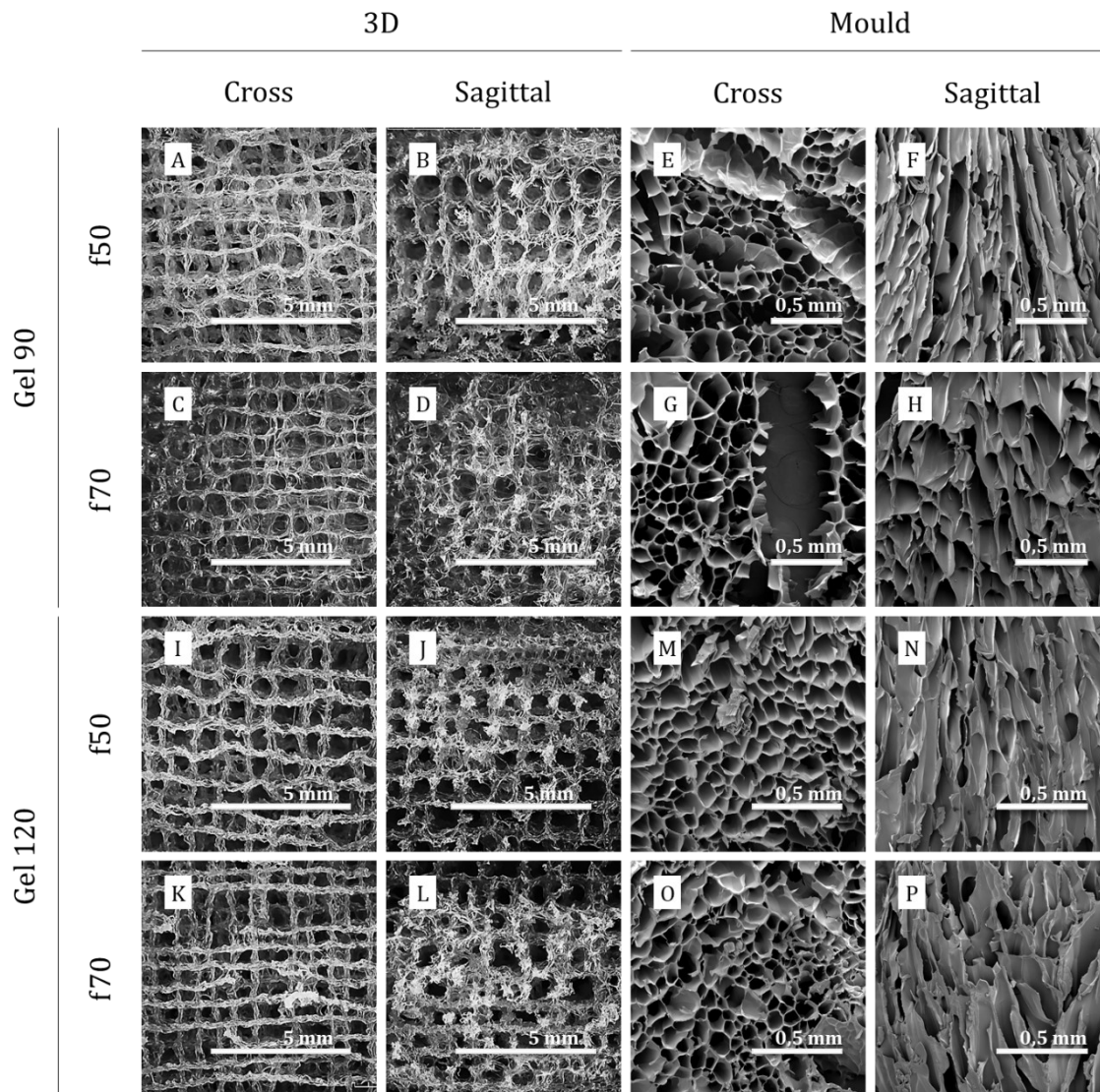
Fig. 2.4 Cross and sagittal section of 3D printed and mould casted scaffolds, after freeze casting, respectively acquired by optical microscope and ESEM.

What was immediately clear from the morphological characterization was the directional mould-casting process, performed to obtain well aligned and ordered porosity, was successful. As it is clearly observable from both the cross and the sagittal section of the mould casted samples, there were no relevant differences among the concentrations used (Fig. 2.4). The moulds obtained by Gel90 were, nevertheless, presenting significant and extensive cracks, probably due to the higher amount of water in the Gel solution (Fig. 2.4). Moreover, it is visible that, while for the mould casted scaffolds there were no differences in the pores dimensions or geometry depending on the Gel solution concentration, that was not alike for the 3D printed

scaffolds, for which a higher Gel solution concentration resulted in a better shape maintenance and model fidelity, especially at higher infill percentages. This was probably ascribable, as for the cracks in the mould-casted scaffolds, to the higher water amount in Gel90, that introduced a strong distortion effect on the sample during the freeze-casting process. Gel90 f70 resulted indeed in scaffolds with smaller and round-shaped pores, likely due to the mesh lines touching and merging before being stabilized in the freeze-casted structure.

The above mentioned morphological features emerged also in the porosity size evaluation performed by images analysis (Fig. 2.5 C), in which mould-casted scaffolds showed no significant differences in pores size at any conditions (from 121,77 μm ± 47,67 of Gel90 f50 to 157,02 μm ± 51,75 of Gel120 f50); on the other hand, Gel90 samples showed a way more similar porosity to the mould-casted scaffolds than not to the Gel120 printed ones, with the same printing model used (with a porosity of 113,93 μm ± 14,71 for Gel90 f50 and 116,93 μm ± 26,02 for Gel90 f70 versus 939,28 μm ± 210,62 for Gel120 f50 and 684,56 μm ±130,14 for Gel120 f70). Gel120 printed scaffolds porosity was instead consistent with the one designed and expected, with a bigger porosity for Gel120 f50 and a reduced one for Gel120 f70 (Fig. 2.5 C).

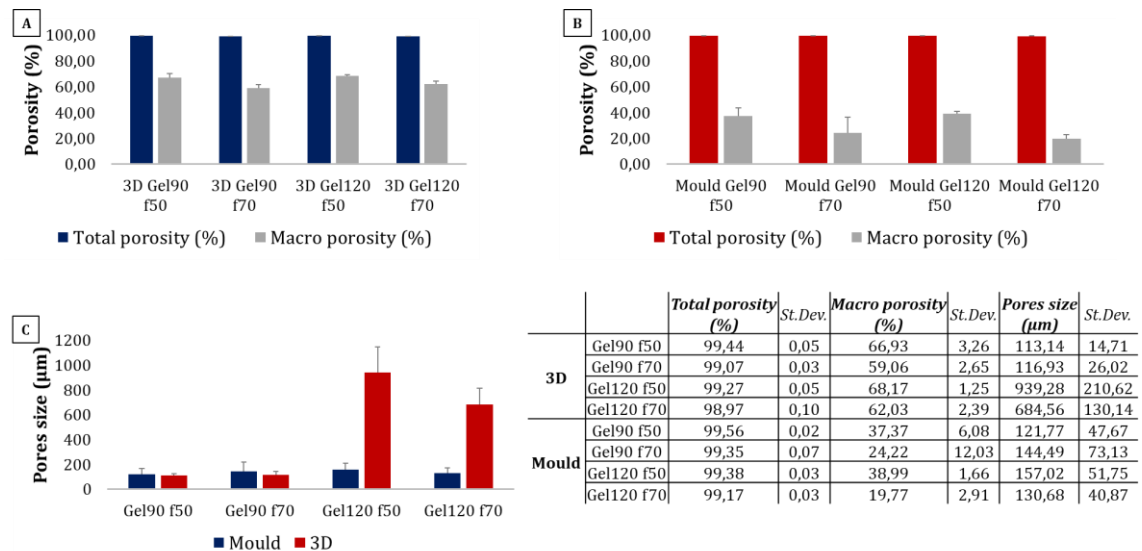|		Total porosity (%)	St.Dev.	Macro porosity (%)	St.Dev.	Pores size (μm)	St.Dev.
3D	Gel90 f50	99,44	0,05	66,93	3,26	113,14	14,71
	Gel90 f70	99,07	0,03	59,06	2,65	116,93	26,02
	Gel120 f50	99,27	0,05	68,17	1,25	939,28	210,62
	Gel120 f70	98,97	0,10	62,03	2,39	684,56	130,14
Mould	Gel90 f50	99,56	0,02	37,37	6,08	121,77	47,67
	Gel90 f70	99,35	0,07	24,22	12,03	144,49	73,13
	Gel120 f50	99,38	0,03	38,99	1,66	157,02	51,75
	Gel120 f70	99,17	0,03	19,77	2,91	130,68	40,87

Fig. 2.5 Total and macro porosities of 3D printed (A) and mould casted (B) scaffolds, and their corresponding pore sizes (C).

Density method[26] allowed to calculate the total porosity of the realized scaffolds, that resulted to be almost 99%, independently from the process used (Fig. 2.5 A and B). The water-squeezing method[3,26] was employed to estimate the macro-porosity of the scaffolds, that resulted to be almost double for the 3D printed scaffolds (Fig. 2.5 A and B), thanks to their better pores geometry and interconnection, as proven also by the morphological characterization. Both processes allowed, therefore, to obtain highly porous scaffold crucial for proper cells colonization, anchoring and spreading as well as for their nourishment and waste collection and expulsion. Nevertheless, while with the mould casting process the porosity resulted to be random and mostly small and anisotropic, with the 3D printing the resulting scaffold showed a good model fidelity, with a controllable and tailorable isotropic porosity of one order of magnitude higher, feature that can be of great relevance for *in vivo* tissue development.

2.3.4 Chemical-physical characterization

The swelling test[3,26,27] demonstrated a clear difference among the 3D printed and the mould casted scaffolds (Fig. 2.6 A and B). For the 3D printed ones, the infill rate emerged as the most relevant parameter affecting the swelling, with f50 showing a swelling ratio significantly higher than the f70, while for the mould casted samples the concentration of the Gel solution (Tab. 2.1) appeared to be the most determining parameter, with a gradual but significant swelling ratio decrease from Gel90 f50 to Gel120 f70. For the 3D printed scaffolds this resulted to be consistent with their building process and resulting morphology, while the different behaviour of the mould casted can be arguably ascribable to the reduction of water with the solution concentration increment. This makes, indeed, more difficult the growth of long longitudinal aligned crystals during the freeze-casting process, generating a sparingly interconnected porosity, less likely to efficiently absorb the medium.
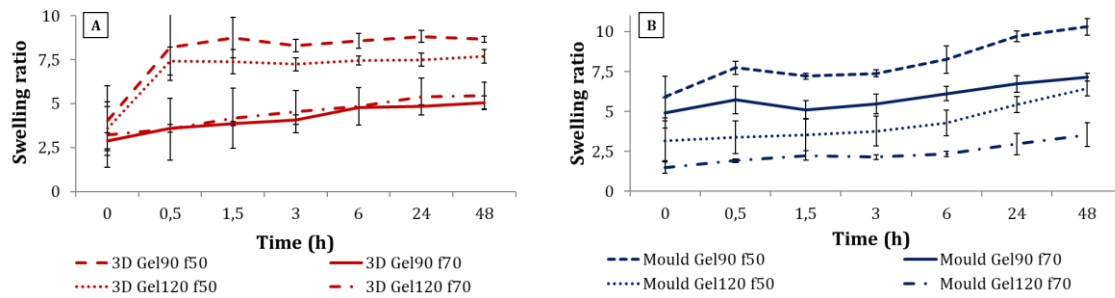
Fig. 2.6 Swelling ratios for 3D printed (A) and mould casted (B) scaffolds represented as mean with st.dev. bars.

The degradation test[26] was performed to evaluate the suitability of the realized scaffolds to be implied in physiological environment, adequately withstanding the cellular colonization and growth before to start degrading to be resorbed. Both the casted and printed scaffolds proved good performances with degradation ratios under 15% at 21 days, nearly constant from 7 to 21 days for the most of 3D printed scaffolds (Fig. 2.7 A and B). The slightly higher degradation ratio of the 3D printed ones (Fig. 2.7 A) is likely attributable to their higher macro-porosity and better porosity interconnection, allowing fluids to better flow through the scaffolds structure, fostering matter exchange with the medium.
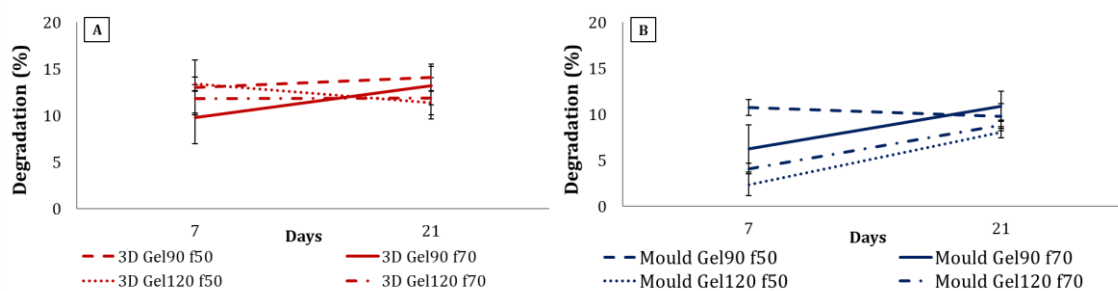
		7 days	St.Dev.	21 days	St.Dev.
	Gel90 f50	13,04	2,94	14,09	1,43
3D	Gel90 f70	9,76	2,82	13,22	2,05
	Gel120 f50	13,40	0,75	11,35	1,26
	Gel120 f70	11,78	1,50	11,85	2,23

		7 days	St.Dev.	21 days	St.Dev.
	Gel90 f50	10,74	0,86	9,80	1,34
Mould	Gel90 f70	6,30	2,55	10,86	1,64
	Gel120 f50	2,35	1,18	8,06	0,60
	Gel120 f70	4,12	0,59	8,80	0,58

Fig. 2.7 Degradation of 3D printed and mould casted scaffolds at 7 and 21 days represented as mean with st.dev. bars.

2.3.5 Dynamic Mechanical Analysis

Since the last aim of a biomaterial is to be *in-vivo* implanted, testing its mechanical properties in *in-vivo* like conditions become crucial to better understand and predict its performances. All the samples tested were overnight pre-conditioned in PBS at 37°C and then tested in uniaxial submersion-compression mode at the same conditions. The Young moduli (E), determined as angular coefficient of the stress-strain response from 0 to 10% strain (*n*=9 ± std. dev.) showed a clear improvement of the compression resistance of the materials for both the 3D printed and the mould casted samples moving from f50 to f70[3,26]. The mould casted ones generally demonstrated higher Young moduli values. The higher values of the 3D Gel90 f50 and f70 confirmed what previously discussed during the morphological evaluation, with a behaviour more similar to the mould casted Gel90 f50 and f70 than to the 3D Gel120 f50 and f70, attributable to their minor shape maintenance and less defined geometry (Fig 2.8).
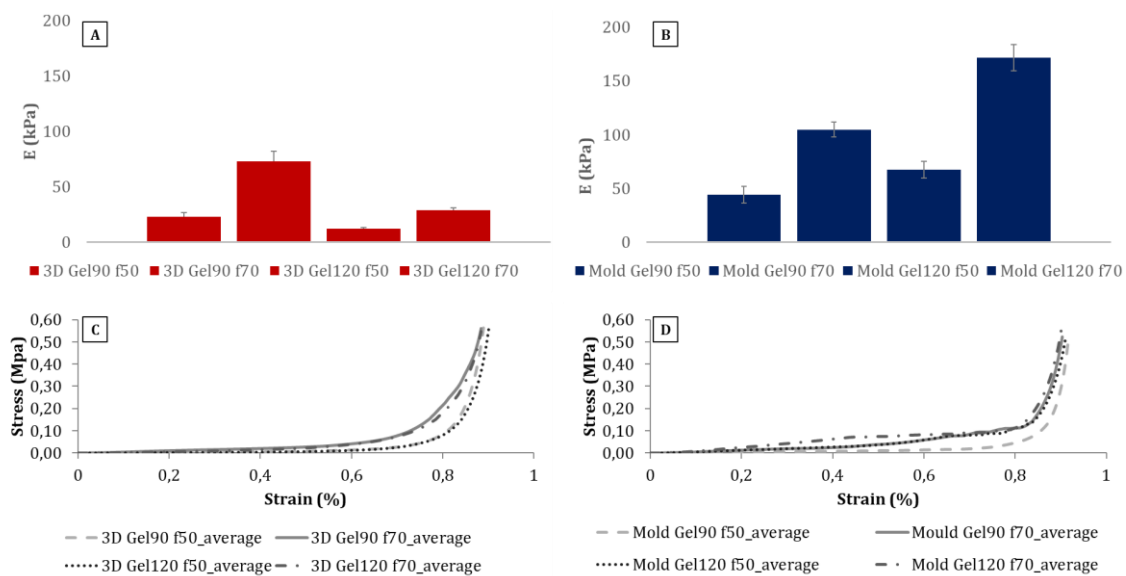

Fig. 2.8 Young's modulus and stress-strain curves of 3D printed (A, C) and mould casted (B, D) scaffolds.

Considered the higher fidelity to the model and better morphology reached with the 3D Gel120 samples, for a further evaluation and comparison of the mechanical properties of the 3D printed and mould casted scaffolds we decided to focus on the Gel120 version of both.

Hence, the recovery ability of the scaffolds was then assessed by a creep test[26] performed setting a creep time of 15 min and a recovery time of 15 min with an applied stress of $6 \cdot 10^{-2}$ MPa (Fig. 2.9). It was clearly possible to see the higher tendency of the 3D printed to quickly deform, reaching the 80% of deformation, as well as their extremely good recovery capability, of about 100% immediately after the compression force removal. The mould casted showed instead a higher resistance to deformation, remaining under the 60%, coupled with a slightly lower recovery ability, although still near to 100%.
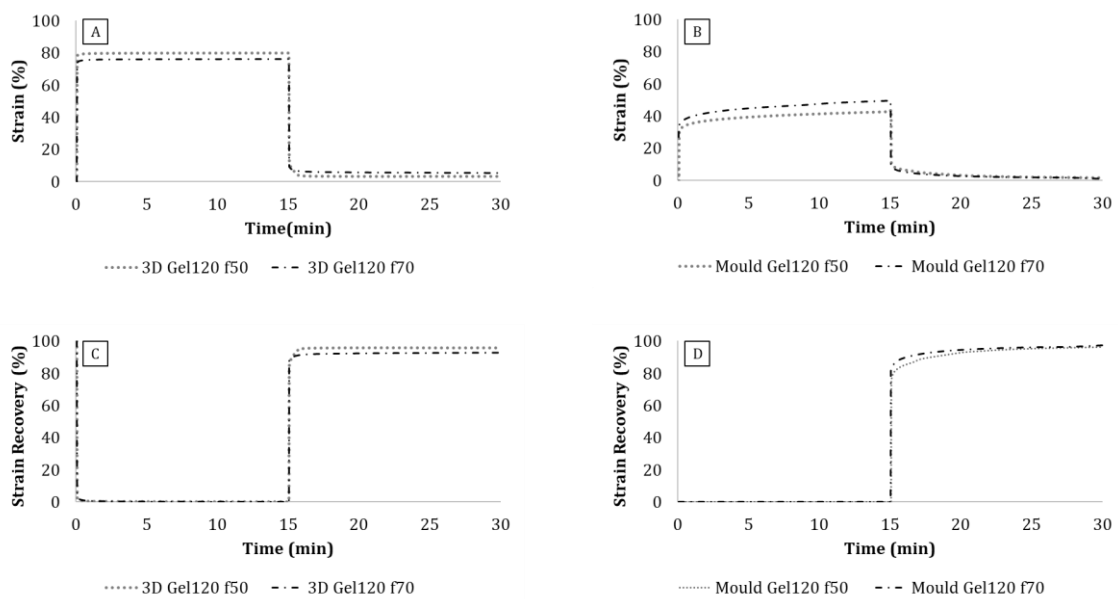
Fig. 2.9 Compression resistance (A, B) and recovery ability (C, D) evaluation and comparison of the 3D printed and mould casted scaffolds.

The viscoelastic behaviour was finally determined as storage modulus E' and loss modulus E'' by evaluating them through a multifrequency test[26] in a frequency range from 1 to 10 Hz. The loss modulus E'' resulted to be nearly not significant compared to the storage modulus E', pointing out, as expected, the predominance of the elastic behaviour for both the materials (Fig. 2.10). Moreover, the higher values of the 3D printed E' compared to the mould casted confirmed the propensity of this kind of scaffolds to better withstand deformation, as already highlighted also by the creep test.
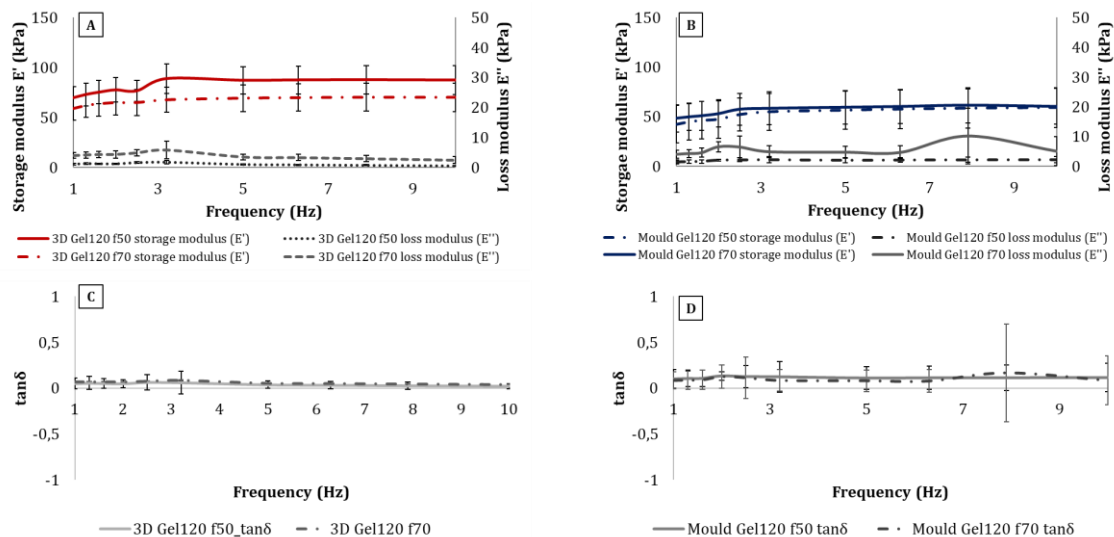
Fig. 2.10 Evaluation of the storage modulus, loss modulus and tanδ of 3D printed and mould casted scaffolds through multifrequency test.

2.3.6 Biological characterization

A preliminary study with human chondrocytes was performed to verify the suitability of both Gel120 f70 mould casted and 3D printed materials as scaffolds for cell colonization and viability.

The *in vitro* investigation was performed on cell-seeded scaffolds, where cells were seeded onto the scaffold upper surface. Biological quantitative and qualitative tests on scaffolds were carried out comparing the differential affection of the two material types on cell behaviour. In detail MTT assay highlighted a statistically significant increase over the time of cell proliferation, demonstrating the absence of cytotoxic effect of both Gel120 f70 mould and 3D printed scaffolds with no differences between the two groups (Fig. 2.11 A).

Confirming these positive results, the qualitative analysis of the upper surface by Live/Dead Assay of the scaffolds suggested that both materials were biocompatible and did not compromise the cell viability (Fig. 2.11 B, C, D and E). In fact, a very high number of live cells were seen compared to a very low ratio of dead cells in both mould casted and 3D printed materials (Fig. 2.11 B, C, D and E).
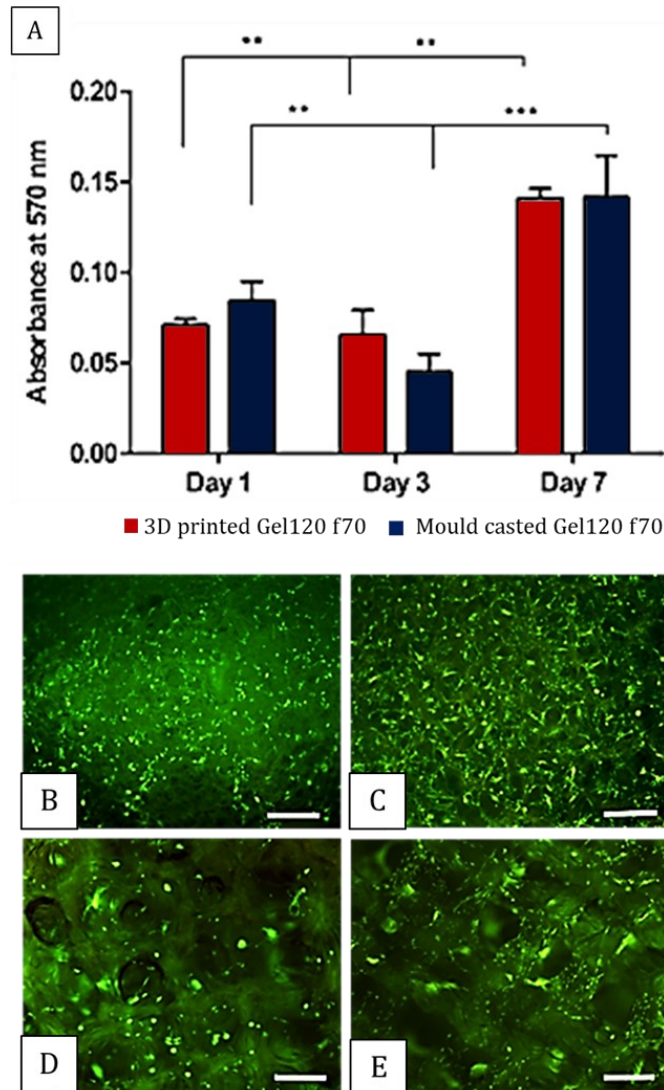
Fig. 2.11 Cells viability analysis. A) MTT assay was performed after 1, 3, and 7 days of cell culture. The results were reported in the graph as mean ± standard error of the mean. ** p-value ≤ 0,01, *** p-value ≤ 0,001. B) Live&/Dead assay (Calcein stains live cells in green, ethidium homodimer-1 stains dead cells in red) on cells seeded on Gel120 f70 mould-casted (B day 1; C day 3) and Gel120 f70 3D printed scaffolds (D day 1, E day 3). Scale bars: 500 μm.

Moreover, the analysis of the upper surface by DAPI staining confirmed an increase in cell density over the time in both the material types despite the very different scaffold morphology (Fig. 2.12 A to F). In the Gel120 f70 mould-casted scaffold, cells remained more anchored to the upper surface creating a cell layer well visible at day 7 (Fig. 2.12 C to G). In the 3D printed scaffold, instead, cells deeper penetrated in the interstices of the sample guaranteeing a better cell colonization of whole biomaterial, index of a more real and mimetic attitude of *in vivo* situation (Fig. 2.12 F to H). This difference was confirmed by the analysis of the inner section of the

two scaffolds: after 7 days the cells, seeded onto the upper surface, migrated through the porous structure and cells were seen well attached to the middle-lower level of the scaffold only in the 3D printed scaffold as shown by the section reconstruction in (Fig. 2.12 I and J).

Fig. 2.12 Scaffold colonization analysis by nuclei detection with DAPI at D1 (A, D), D3 (B, E) and D7 (C, F and I,J). In detail mould Gel120 f70: A-C and I, 3D Gel120 f70: D-F and J. Scale bars: A-F 200 µm; I,J 500 µm. White arrows indicate some groups of cells in the inner scaffold surfaces.

2.4. Conclusions

A morphological, chemico-physical, mechanical and biological properties evaluation of additive-free gelatine-based ink processed in two different ways, 3D printing and mould casting, was performed.
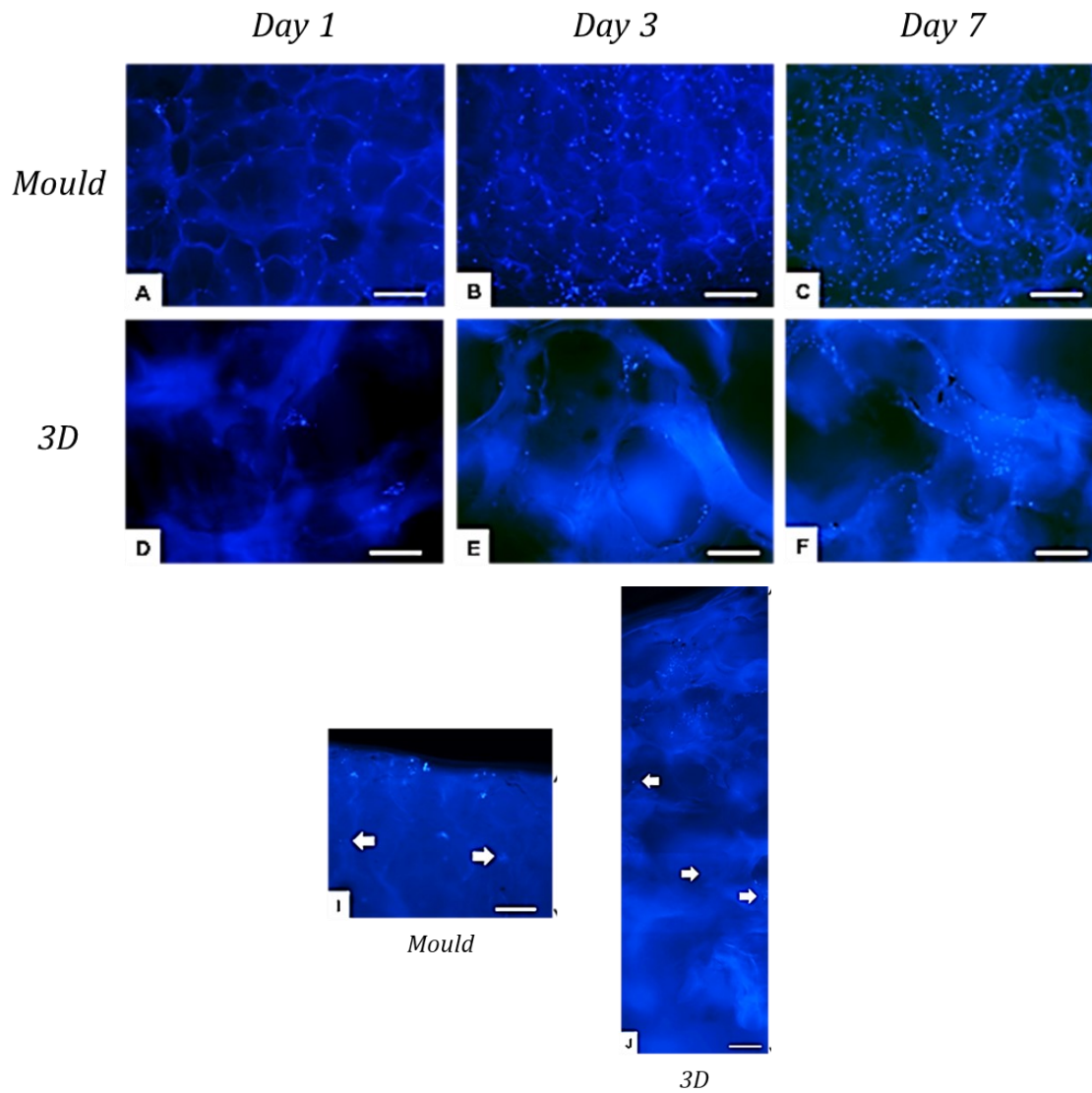
Interesting results from the 3D printing approach were recorded. It was reached a good printability and shape maintenance, proper geometry control in terms of alignment and model fidelity, no delamination and suitable medium uptake and degradation rate to allow an appropriate cell colonization and growth.

For the mould casting, the morphology design resulted to be more difficult to lead, with the alignment ensuing as the only parameter possible to control in the building process, through a thorough set-up of the freeze-casting process, and, partially, working on the Gel solution concentration.

From the mechanical characterization it was possible to infer the greater ability of the 3D printed scaffolds to face heavy deformations with complete recover, contrarily to the higher resistance to deformation of the mould casted. Cells spreading and attachment resulted to be less homogeneous on the mould casted scaffolds, with cells attaching and spreading mainly on the outer part, attributable to a smaller porosity, likely less interconnected, especially in the most concentrated ones. All these qualities outlined the products of the two building processes can be suitable for distinct applications in chondral regeneration, depending on the features required to fulfil the regenerative need. The greater ability of the 3D printed scaffolds to recover after huge deformations, promoting contextually a significant fluid exchange, and their favoured homogeneous cell colonization, could be exploited for regeneration of load bearing chondral regions were a fast tissue turn-over is prompted. On the contrary, the higher stiffness of the mould casted scaffolds together with their lower proclivity to allow a fast deep cell colonization could be used to tune their degradation thus a possible *in-situ* drug release contextually.

All in all, we were able to realize gelatine-based scaffolds, with no need of additive, nor for the processing nor for the crosslinking, showing a good biocompatibility and different exploitable features, potentially suitable for diverse application in chondral regeneration.

References

1.   Tschon, M. *et al. Assessment of the in vivo biofunctionality of a biomimetic hybrid scaffold for osteochondral tissue regeneration. Biotechnology and Bioengineering* (2020). doi:10.1002/bit.27584.

2.   Shankar, K. G. *et al.* Investigation of different cross-linking approaches on 3D gelatine scaffolds for tissue engineering application: A comparative analysis. *Int. J. Biol. Macromol.* **95**, 1199–1209 (2017).

3.   Gostynska, N. *et al.* 3D porous collagen scaffolds reinforced by glycation with ribose for tissue engineering application. *Biomed. Mater.* **12**, (2017).

4.   Huey, D. J., Hu, J. C. & Athanasiou, K. a. Remains Elusive. *Science (80-.).* **6933**, 917–921 (2012).

5.   Chia, H. N. & Wu, B. M. Recent advances in 3D printing of biomaterials. *J. Biol. Eng.* **9**, 1–14 (2015).

6.   Turnbull, G. *et al.* 3D bioactive composite scaffolds for bone tissue engineering. *Bioact. Mater.* **3**, 278–314 (2018).

7.   Abdulghani, S. & Mitchell, G. R. Biomaterials for in situ tissue regeneration: A review. *Biomolecules* **9**, (2019).

8.   Bobbert, F. S. L. & Zadpoor, A. A. Effects of bone substitute architecture and surface properties on cell response, angiogenesis, and structure of new bone. *J. Mater. Chem. B* **5**, 6175–6192 (2017).

9.   Zadpoor, A. A. Bone tissue regeneration: The role of scaffold geometry. *Biomater. Sci.* **3**, 231–245 (2015).

10.   Nagiah, N. *et al.* Spatial alignment of 3D printed scaffolds modulates genotypic expression in pre-osteoblasts. *Mater. Lett.* **276**, 128189 (2020).

11.   Weber, F. E. Reconsidering Osteoconduction in the Era of Additive Manufacturing. *Tissue Eng. - Part B Rev.* **25**, 375–386 (2019).

12.   Bose, S., Koski, C. & Vu, A. A. Additive manufacturing of natural biopolymers and composites for bone tissue engineering. *Mater. Horizons* **7**, 2011–2027

(2020).

13. Gu, B. K., Choi, D. J., Park, S. J., Kim, Y. & Kim, C. *Cutting-Edge Enabling Technologies for Regenerative Medicine. Cutting-Edge Enabling Technologies for Regenerative Medicine. Advances in Experimental Medicine and Biology* vol. 1078 (2018).

14. Bose, S., Ke, D., Sahasrabudhe, H. & Bandyopadhyay, A. Additive manufacturing of biomaterials. *Prog. Mater. Sci.* **93**, 45–111 (2018).

15. Li, N. *et al.* 3D printing to innovate biopolymer materials for demanding applications: A review. *Mater. Today Chem.* **20**, (2021).

16. Liu, J. *et al.* Current advances and future perspectives of 3D printing natural-derived biopolymers. *Carbohydr. Polym.* **207**, 297–316 (2019).

17. Cernencu, A. I. *et al.* Bioinspired 3D printable pectin-nanocellulose ink formulations. *Carbohydr. Polym.* **220**, 12–21 (2019).

18. Schwab, A. *et al.* Printability and Shape Fidelity of Bioinks in 3D Bioprinting. *Chem. Rev.* **120**, 11028–11055 (2020).

19. Ribeiro, A. *et al.* Assessing bioink shape fidelity to aid material development in 3D bioprinting. *Biofabrication* **10**, (2018).

20. Kwon, H., Paschos, N. K., Hu, J. C. & Athanasiou, K. Articular cartilage tissue engineering: The role of signaling molecules. *Cell. Mol. Life Sci.* **73**, 1173–1194 (2016).

21. Oryan, A., Kamali, A., Moshiri, A., Baharvand, H. & Daemi, H. Chemical crosslinking of biopolymeric scaffolds: Current knowledge and future directions of crosslinked engineered bone scaffolds. *Int. J. Biol. Macromol.* **107**, 678–688 (2018).

22. Franks, F. Freeze-drying of bioproducts: Putting principles into practice. *Eur. J. Pharm. Biopharm.* **45**, 221–229 (1998).

23. Li, W. L., Lu, K. & Walz, J. Y. Freeze casting of porous materials: Review of critical factors in microstructure evolution. *Int. Mater. Rev.* **57**, 37–60 (2012).

24.   Wegst, U. G. K., Schecter, M., Donius, A. E. & Hunger, P. M. Biomaterials by freeze casting. *Philos. Trans. R. Soc. A Math. Phys. Eng. Sci.* **368**, 2099–2121 (2010).

25.   Panseri, S. *et al.* Biomimetic scaffold with aligned microporosity designed for dentin regeneration. *Front. Bioeng. Biotechnol.* **4**, 1–8 (2016).

26.   Campodoni, E. *et al.* Polymeric 3D scaffolds for tissue regeneration: Evaluation of biopolymer nanocomposite reinforced with cellulose nanofibrils. *Mater. Sci. Eng. C* **94**, 867–878 (2019).

27.   Sandri, M. *et al.* Fabrication and pilot in vivo study of a collagen-BDDGE-elastin core-shell scaffold for tendon regeneration. *Front. Bioeng. Biotechnol.* **4**, 1–14 (2016).

28.   Campodoni, E. *et al.* Mimicking Natural Microenvironments: Design of 3D-Aligned Hybrid Scaffold for Dentin Regeneration. *Front. Bioeng. Biotechnol.* **8**, 1–12 (2020).

29.   Campodoni, E. *et al.* Blending gelatine and cellulose nanofibrils: Biocomposites with tunable degradability and mechanical behavior. *Nanomaterials* **10**, 1–18 (2020).

30.   O'donnell, B. T. *et al.* Adipose tissue-derived stem cells retain their adipocyte differentiation potential in three-dimensional hydrogels and bioreactors. *Biomolecules* **10**, 1–16 (2020).

31.   Le Guéhennec, L. *et al.* In vitro and in vivo biocompatibility of calcium-phosphate scaffolds three-dimensional printed by stereolithography for bone regeneration. *J. Biomed. Mater. Res. - Part A* **108**, 412–425 (2020).

32.   Wolf, B., Lam, S., Kirkland, M. & Frith, W. J. Shear thickening of an emulsion stabilized with hydrophilic silica particles. *J. Rheol. (N. Y. N. Y).* **51**, 465–478 (2007).

33.   Ding, H., Geng, J., Lu, Y., Zhao, Y. & Bai, B. Impacts of crosslinker concentration on nanogel properties and enhanced oil recovery capability. *Fuel* **267**, 117098 (2020).

34. Dhanumalayan, E. & Joshi, G. M. Performance properties and applications of polytetrafluoroethylene (PTFE)—a review. *Adv. Compos. Hybrid Mater.* **1**, 247–268 (2018).

35. Chen, X. *et al.* Effect of the application of a dehydrothermal treatment on the structure and the mechanical properties of collagen film. *Materials (Basel).* **13**, (2020).

36. Krishnakumar, G. S. *et al.* Evaluation of different crosslinking agents on hybrid biomimetic collagen-hydroxyapatite composites for regenerative medicine. *Int. J. Biol. Macromol.* **106**, 739–748 (2018).

CHAPTER 3

Three-dimensional bioprinting of biomimetic nano-hydroxyapatite functionalized gelatine methacryloyl-based bioinks for bone tissue engineering

3.1 Introduction

The natural bone is a composite material consisting of a defined ratio of organic matrix, mainly made of collagen type I, and inorganic phase, hydroxyapatite (HA), with HA crystals orderly embedded within the collagen matrix[1,2–4].

Traditionally, bone has been viewed as a relatively static tissue, as a mere collection of calcified tubes only serving as a scaffold for other organs. In the past decade however a more complex picture of bone physiology has emerged. It is now clear that bone integrity and normal function depends upon, but also affects, other organs. For instance, it is now known that bone plays a role in the maintenance of the hematopoietic stem cell niche, in the control of serum calcium and in the control of phosphate absorption by the kidney[5–7].

The synthesis of new substituting materials mimicking natural bone, as an alternative to autograft and allograft bone replacements, still remains one of the most interesting objective of the technological research. Conventional tissue biofabrication involves seeding cells and biomolecules within a scaffold that possesses a porous structure to mimic properties of extracellular matrix (ECM). The scaffold-based strategies have been successfully used for engineering various tissue constructs, such as bone, skin, and cartilage[8–16]. Nevertheless, these approaches often fail to imitate complex structures of native tissues and are incapable of placing multiple types of cells in desired positions or in an orderly fashion. Three-dimensional (3D) printing, also known as rapid prototyping or additive manufacturing, has been pointed out as the possible solution to solve these problems[17–24].

Among all the additive manufacturing technologies, in particular, three-dimensional bioprinting is raising increasing attention. In three-dimensional bioprinting relies indeed the possibility to combine technology and biology to better

reproduce bone tissue complexity in order to obtain patient-specific and anatomically shaped constructs. This, by creating the perfect micro- and macro-environment featured by the correct matrix to embed the osteogenesis related cells required for the engineered tissue development and the correct cues and stimuli to properly lead its growth and maturation[16,25–31].

Focussing more specifically on the bone tissue, what plays a major role in providing these stimuli to the cells is the inorganic phase[32,33]. Thanks to a better knowledge and understanding of the functional role of the active groups present in the natural bone tissue, increasing attention has been given to the development of new biomimetic non-stoichiometric apatites, which can provide higher rate of biodegradability and bioactivity compared to stoichiometric hydroxyapatite. Two aspects substantially influence the bioactivity of hydroxyapatite at physiological conditions: its crystallinity grade and the addition of doping groups which can be exploited to make it comparable to that of natural bone tissues[2,34,35].

Within this work, we aimed to target bone-tissue regeneration towards the technology of 3D bioprinting (Fig. 3.1).
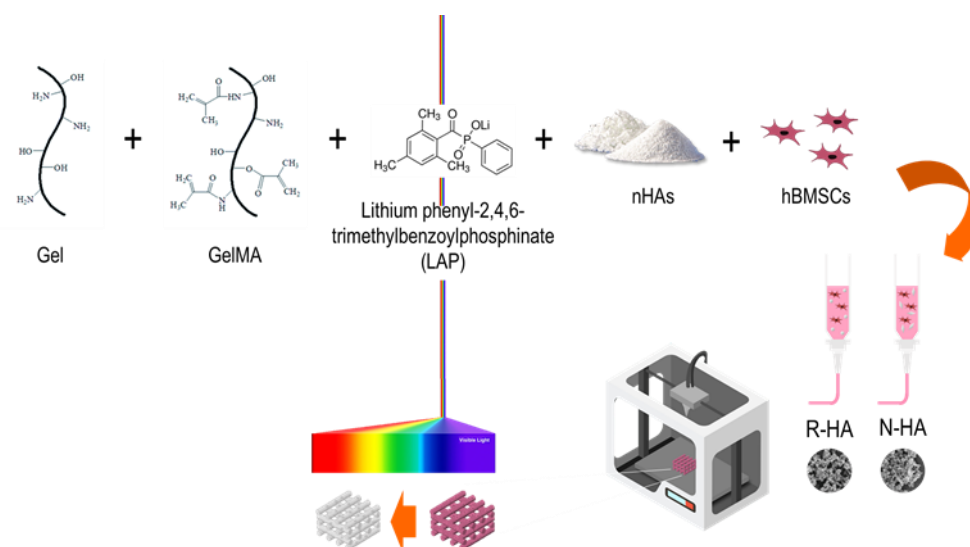
Fig. 3.1 Workflow schematic representation of N-HA (A) and R-HA (B) bioinks formulation and 3D printed scaffolds realization.

To reach this goal we aimed for bioprinting hBMSCs towards the realization of a hydrogel-based bioink made of an EC-like matrix, into which embed the cells, a nature-inspired biomimetic inorganic phase to provide cells with the correct stimuli

to differentiate and a proper crosslinker to confer the scaffolds an appropriate degradation-rate. More specifically, as main matrix component, we opted for gelatine functionalized with methacryloyl groups (GelMA), because of its previously proven biocompatibility[36–39], but also and mainly thanks to the possibility to crosslink it with a relatively little-known photoiniziator, lithium phenyl-2,4,6-trimethylbenzoilphospinate, better known as LAP, able to perform a crosslinking reaction within the visible light spectra, providing unquestionable benefits over the commonly used UV-photoiniziators[37,37,38,40–45]. GelMA as is cannot, however, provide the cells with the correct cues to differentiate, and in this context, we decided to evaluate the effect on them of two chemically, physically, and morphologically different inorganic phases. Then, we moved towards the test of the so obtained bioinks in all the aspects of the bioprinting process, from extrusion to scaffolds maturation.

3.2 Materials and methods

3.2.1 nHAs synthesis and characterization

Two different nano-hydroxyapatites (nHAs), respectively Mg-doped and $MgCO_3$-doped, were synthetized according to the protocol reported by Landi et al.[35,46]. Briefly, the magnesium-doped hydroxyapatite (Mg-HA, from now on referred as N-HA) was synthetized through the classical neutralization method based on the controlled dripping of 49,6 mL 1.2 M H_3PO_4 solution (Sigma Aldrich, 85% pure) in 82,7 mL of 1.2 M $Ca(OH)_2$ (Sigma Aldrich, 95% pure) aqueous suspension containing 8,48 g of $MgCl_2 \cdot 6H_2O$ (0,42% doping rate), maintained at 40°C under magnetic stirring. The magnesium- and carbonate- doped hydroxyapatite ($MgCO_3$-HA, from now on referred as R-HA) was similarly prepared adding to the synthesis the simultaneous controlled dripping into $Ca(OH)_2$ suspension of 46,0 mL 0,8 M solution of $NaHCO_3$ (Sigma Aldrich), performing the reaction at 25°C. The precipitation products were aged for 24h at 25°C, washed through centrifugation for three times, lyophilized, sieved at 150 μm, then micronized at 3 μm.

Powders morphology was assessed by electron scanning microscopy (SEM, Carl Zeiss Sigma NTS Gmbh Öberkochen, Germany). Samples preparation for morphological evaluation included powders fixation onto aluminium stubs by carbon tape followed by Au coating applied by sputtering (QT150T, Quorum Technologies Ltd, UK).

Inductively coupled plasma-optical emission spectrometry (ICP-OES) analysis (ICP-OES 5100, vertical dual view apparatus, Agilent Technologies, Santa Clara, CA, USA) was performed to determine nHAs chemical composition and stoichiometry deviations.

X-ray diffraction (XRD) analysis was employed to evaluate the nHAs crystallographic identity and crystallinity.

Thermo-gravimetric analysis (TGA) was used to calculate the residual mass of the nHAs, and in particular to indirectly calculate the carbonation of R-HA.

Attenuated total reflection – Fourier Transform Infrared Spectroscopy (ATR-FTIR) served as proof of nHAs identity and to prove the actual carbonation of R-HA.

3.2.2 nHAs 2D cytotoxicity and biological activity evaluation

Cytotoxcicity of nHAs was indirectly assessed by N-HA and R-HA leachate treatment of 2D human bone marrow mesenchymal stem-cells (hBMSCs).

After obtaining patient consent and approval from the Regional Committee for Medical and Health Research Ethics (REK) in Norway (2013/1248/REK), hBMSCs were isolated from a donor at the Department of Plastic Surgery, Haukeland University Hospital, Bergen, Norway.

Cells were sub-cultured and expanded in T75 culture flasks (Nunc, Thermo Fisher Scientific) to reach the desired amount of cells, under humidified 5% CO_2 at 37° C in Dulbecco's modified Eagle's medium (DMEM; Life Technologies, Gibco, Carlsbad, CA, U.S.A.) with 10% foetal bovine serum (FBS; HyClone, GE Healthcare, Utah, U.S.A.) and 1% penicillin-streptomycin (P/S; Thermo Fisher Scientific, Gibco™, 10 000 U/mL) (BM). 0,5 µL/mL growth factor solution (FGF) were added to the BM for the expansion steps. FGF solution was prepared by diluting 10 µg/mL of FGF powder in PBS (Gibco, Thermo Fisher Scientific, Waltham, MA, US) with 0,1% (1 mg_{BSA}/mL_{PBS}) bovine serum albumin (BSA, Sigma-Aldrich). For the expansion, trypsin (Lonza, Basel, Switzerland) was used to detach the cells from the flasks bottom, after medium removal and a double wash with PBS. To stop the trypsinisation reaction, the same amount of BM was used. Cell number and viability of hBMSCs were assessed after each expansion step using 0.4% trypan blue stain (Invitrogen) and a Countess™ Automated Cell Counter (Invitrogen). Passage four cells were used in the experiments.

N-HA and R-HA leachates were prepared by magnetic stirring of 1% nHAs powder in DMEM at 37°C over-night, then the obtained leachate was sterile filtered (0,2 µm sterile filter). After filtration, the leachate was completed as basic medium (BM) or osteogenic medium (OM) with the addition of L-ascorbic acid (L-AA; MW: 289.54; 35 µL 500 mM in 100 mL) (Sigma-Aldrich), dexamethasone (Dex; MW: 392.46; 20 µL 50 µM in 100 mL) (Sigma-Aldrich) and β-glycerolphosphate (β-Gly; MW: 216.04; 500 µL 2M in 100 mL) (Sigma-Aldrich) and used as conditioning medium. Cells cultured with simple BM and OM were used as control. For all the tests, cells were seeded in 12-well plates with a cell density of 3 x 10^3 cells/cm^2.

hBMSCs were cultured for 21 days, treating them with N-HA and R-HA leachate from d1, and viability (d1, d7, d14, d21), proliferation (d1, d7, d14, d21), differentiation

gene expression (d7, d21), differentiation factors expression (d7, d21) and biomineralization (d21) evaluated.

These aspects were tested, respectively, through live and dead (LD, Live/Dead® Viability/Cytotoxcicity Kit for mammalian cells, Molecular Probes™, Invitrogen detection technologies) test, Cell Counting Kit-8 (CCK-8, Dojindo Molecular Technologies, Inc., Thermo Fisher Scientific), immunofluorescence staining and AlizarinRed S test (Sigma-Aldrich).
LD, CCK-8, and immunofluorescence staining were performed in the dark to avoid samples exposure to the light.

For LD, on timepoints, cells were incubated in a working solution containing EthD-1 (red stain for dead cells) and Calcein-AM (green stain for living cells) in PBS for 30 min at room temperature (25°C) and then imaged with a fluorescence microscope (Nikon Eclipse Ti, Tokyo, Japan).

Proliferation was assessed using CCK-8. To perform the test, 150 μL of CCK-8 solution (100 μL$_{CCK-8}$/mL$_{MEDIUM}$) were used to replace BM and cells were incubated at 37°C for 1h. Then 100 μL of CCK-8 solution were collected from each well to be moved into a 96-wells plate in order to be read by the microplate reader (FLUOstar OPTIMA, BMG LABTECH, Germany). For each sample, five replicates were performed.

Calcium deposition was assessed by Alizarin Red S staining. hBMSCs coltured in N-HA and R-HA leachate, and in BM as control, were fixed at day 21 with 4% pFA for 1h. After fixation, cells were stained with 2% Alizarin Red S (pH 4.1; Sigma-Aldrich) solution for 15 min at RT, and then washed and dried overnight. After washing and air-drying, images were taken with an optical microscope (Nikon, Tokyo, Japan). For quantification, the colour was extracted with 100 mM cetylpyridinium chloride (Sigma-Aldrich), and the absorbance was measured with a microplate reader (BMG Labtech, Offenburg, Germany) at 540 nm.

3.2.3 Bioprinting

3.2.3.1 Bioink formulation

0,5 g gelatine from porcine skin (Sigma-Aldrich) were dissolved in 8 mL of DMEM with 1% P/S at 80°C in water bath under magnetic stirring for 30 minutes, covered to avoid evaporation. Temperature was lowered to 45°C and 0,5 g GelMA (Sigma-Aldrich) added to the mixture and stirred until perfect dissolution. Temperature was then lowered to 37°C and 1 mL of DMEM with 1% P/S was used to homogeneously suspend 10 mg nHA before addition to the mixture. At last, 1 mL of sterile filtered lithium phenil-2,4,6-trimethylbenzoilphosphinate (LAP, >98%, TCI) solution 10 mg/mL was added after nHA was perfectly dispersed in the mixture. The ink was then let mix for 1h at 37°C, covered to avoid evaporation. The ink final composition was Gel 5% w/w$_{tot}$; GelMA 5% w/w$_{tot}$; nHA 1% w/w$_{solid\ content}$; LAP 1% w/w$_{solid\ content}$. Considered the photosensitive nature of LAP, all the steps involving LAP were always perform in the dark, to avoid unintentional partial pre-crosslinking of the ink. The ink was then thermally conditioned. In detail, it was stock at 4°C overnight, heated up at 37°C for 30 minutes, mixed with cells, loaded into the printing cartridge, cooled down to 4°C for 18 minutes, then heated up to the printing temperature of 26°C. The same cells used for the 2D experiments were used for the 3D study. Passage four cells were employed. For the realization of the bioink, after number and viability check, cells were centrifuged and resuspended in 0,5 mL of DMEM with 1% P/S, and the mixing step performed with a luer-lock connected double syringes system. For the bioinks creation a concentration of 5 mln$_{cells}$/mL$_{ink}$ was employed.

3.2.3.2 Scaffolds design, realization, and processing

The printing process was performed with an Envisiontec 3D-Bioplotter® and design and slicing realized with a dedicated parametric three-dimensional drawing and design software. The scaffold was designed with a squared base of 1 cm x 1 cm, 90° straight perpendicular line mesh, 1,2 mm strands distance, 4 layers height and it was realized with a $\emptyset_{in}$ = 0,41 mm metal needle using an average pressure of 1.3 bar at an average speed rate of 13 mm/s.

The printing process was performed into 6-well plates placed onto 4°C printing bed, in dark and sterile conditions. Immediately after printing, scaffolds were crosslinked with a dental curing lamp for 30 seconds with a perpendicular exposure at 0,5 cm distance. Scaffolds were then moved into 24-well plates and cultured in BM with addition of Normocin™ (Invivogen) for 21 days.

3.2.4 Rheology

The rheological behaviour of the inks was investigated at 27 °C by measuring their viscosity with a ramp test in controlled stress mode. All the measurements were performed with a rotational rheometer (C-VOR 120, Bohlin Instruments, UK). The ramp test was performed using a plate/plate PP20 (Ø = 20 mm) geometry by increasing the shear stress from 0.005 Pa up to 5000 Pa with a sweep time of 500 s. Before to start the test, the samples were let at rest for 3 min to reduce possible influence on the measurement induced by the solutions handling. The measurements were performed using a solvent trap to avoid water evaporation during the test.

3.2.5 Printability

Inks printability was assessed through three main tests: filament drop, filament spreading and buildability[47–50]. For the tests, inks without cells were used. The same printing set-up used for the realization of the actual scaffolds was employed.

For the filament drop test, after ink thermal conditioning, the filament extrusion profile of each ink, extruded at the same pressure, was evaluated. For filament spreading test, 5 cm x 5 cm 2 layers height scaffolds were printed, and through a high-contrast perpendicular picture of the printed structure evaluated the model fidelity by a dedicated image elaboration software. Buildability of each ink was assessed by printing two different three-dimensional structures: a 10 mm x 20 mm cylinder and a 10 mm x 20 mm cone.

3.2.6 3D bioprinted scaffolds biological characterization

The 3D bioprinted scaffolds were designed and realized as previously described, then cultured in BM and OM. Then viability, proliferation, differentiation genes and factor expression were evaluated as for the 2D culture, with slight changes to adapt the protocols to the 3D samples.

For LD, on timepoints, the scaffolds were incubated in a working solution containing EthD-1 (red stain for dead cells) and Calcein-AM (green stain for living cells) in PBS for 45 min at room temperature (25°C) and then imaged with a fluorescence microscope (Nikon Eclipse Ti, Tokyo, Japan).

Proliferation was assessed using CCK-8. To perform the test, 200 μL of CCK-8 solution (100 $\mu L_{CCK-8}/mL_{MEDIUM}$) were used to replace the culture medium and cells were incubated at 37°C for 2h. Then 100 μL of CCK-8 solution were collected from each well to be moved into a 96-wells plate in order to be read by the microplate reader (FLUOstar OPTIMA, BMG LABTECH, Germany). For each sample, five replicates were performed.

Differentiation factors expression, in particular runt homology domain X2 (RunX2) at D7 and osteocalcin (Ocn) at D21, was assessed by immunofluorescence (IF) staining. Cells were fixed with 4% paraformaldehyde (pFA, Sigma-Aldrich) for 1h at 25°C, wash twice with PBS, permeabilized with 0.3% Triton X-100 in PBS and blocked with 0.1% Triton X-100, 1% BSA and 10% normal goat serum (NGS) in PBS. After washing once with a solution of 1% NGS, 0.1% Triton-X-100 and 1% BSA in PBS, cells were incubated under shaking with rabbit polyclonal anti-RunX2 (Abcam, Cambridge, UK, dilution 1:200 in 1% NGS and 1% BSA in PBS) for 3 days at 4 °C. Three washing steps of 1h each and one overnight at 4°C under shaking with 0.1% Triton-X-100 and 1% BSA in PBS were carried out before applying goat anti-rabbit Alexa Fluor 488 IgG as secondary antibody (Life Technologies, Carlsbad, CA, USA, dilution 1:400 in 1% BSA in PBS). The actin cytoskeleton was simultaneously stained using phalloidin tetramethyl rhodamine B isothiocyanate peptide from Amanita phalloides (Sigma-Aldrich, dilution 1:500 in 1% BSA in PBS). After washing with PBS, the nuclei were stained with 4′,6-diamidino-2-phenylindole (DAPI) (Sigma-Aldrich, dilution 1:2000 in PBS) for 15 minutes. Images were taken using a confocal microscope (Leica TCS SP8 STED 3X, Leica microsystems, Germany).

3.3 Results and discussion

3.3.1 nHAs physical-chemical and morphological characterization

The two nHAs, Mg-doped and Mg^{2+} and CO_3^{2-} doped, meaning N-HA and R-HA, were synthetized differently doped and respectively at 40°C and room temperature in order to obtain two chemically, physically, and morphologically different, nature inspired and biomimetic inorganic phases[35,46]. More specifically, we aimed to produce a mono-substituted crystalline and needle-like hydroxyapatite (N-HA) and a bi-substituted amorphous and round-shaped one (R-HA). The two different morphologies were selected to evaluate both the effects on the cells and on the printing process. We indeed wanted to evaluate if the needle-like shape of the N-HA could provide an alignment within the filament during the printing process, improving the extrusion and contextually the model fidelity compared to the round-shaped R-HA (Fig.3.2 respectively A and B). Despite the marked amorphousness of the R-HA does not allow to label the obtained inorganic phase as proper hydroxyapatite but frames it more properly as an amorphous calcium phosphate (ACP), for ease of terminology it will still be referred as $MgCO_3$-HA as well as R-HA in the text.
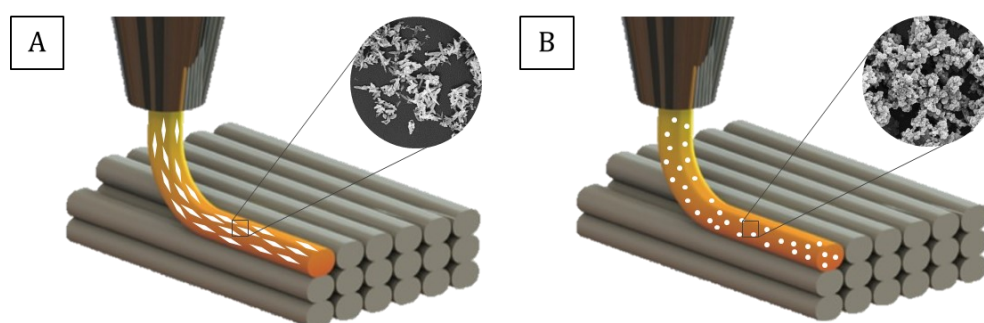

Fig. 3.2 Schematic representation of N-HA (A) and R-HA (B) filament deposition through extrusion based three-dimensional printing.

To evaluate the designed properties were obtained, after the synthesis the nHAs were characterized towards XRD, TGA, SEM, ATR-FTIR and ICP.

X-ray diffraction was employed to confirm the crystallinity degree and HAs identity. HA identity was successfully proved by HA peaks recognition for N-HA (Fig. 3.3). As planned, N-HA showed a higher crystallinity degree compared to the R-HA, designed to be, and resulted, amorphous.
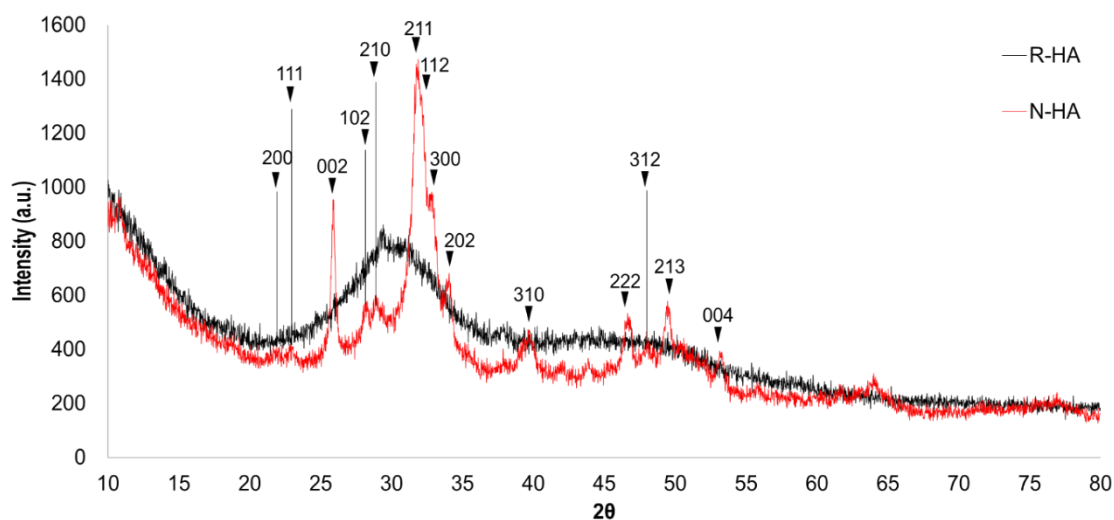
Fig. 3.3 XRD spectra of R-HA (black) and N-HA (red).

ATR analysis clearly showed the phosphate bands within 950–1050 cm^{-1} and 550–600 cm^{-1}, together with the presence of both the absorbed and the occluded water, being respectively referred to the broad band around 2650-3650 cm^{-1} and to the peak at 1660 cm^{-1}. Moreover, the typical signals of β-carbonation, meaning the substitution in the phosphate site, were detected as shown by the CO_3^{2-} stretching signals around 1420 and 1480 cm^{-1} and bending peak around 870 cm^{-1}. In agreement with the synthesis design, the carbonation of R-HA resulted to be way higher compared to N-HA, in which it was possible to detect a slight carbonation due the environmental conditions into which the synthesis was conducted (Fig. 3.4).
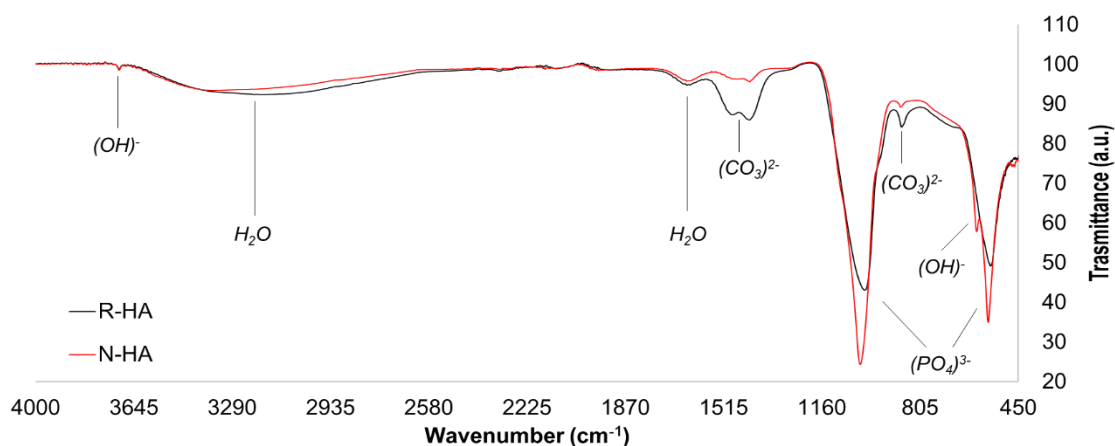
Fig. 3.4 ATR spectrum of R-HA (black) and N-HA (red).

The higher crystallinity of N-HA compared to R-HA was confirmed by the thermogravimetric analysis (Fig. 3.5), which also confirmed the successful R-HA carbonation, with CO_2 loss within the range 600°C-800°C, after the initial water loss within 25°C-100°C.
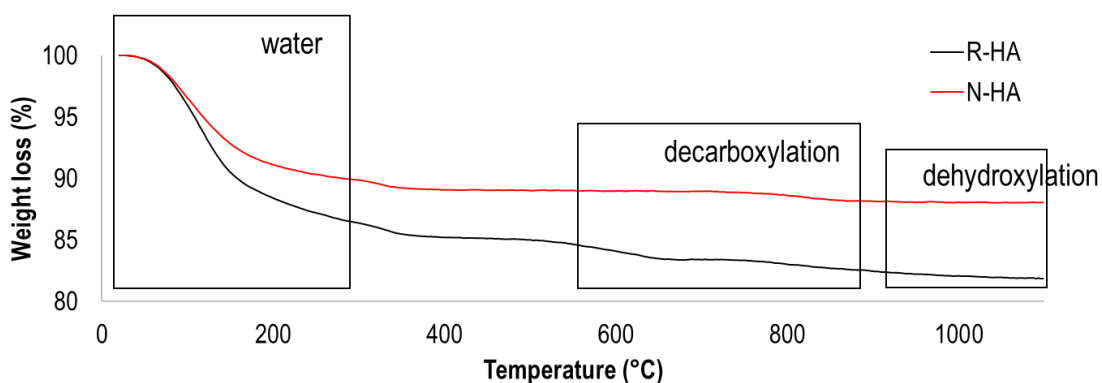
	CO₂ weight loss (%)	Residual (%)
N-HA	1,00	94,86
R-HA	2,46	90,45

Fig. 3.5 TGA profile of R-HA (black) and N-HA (red) with the respective CO_2 percentual weight loss and percentual residual mass reported in the annexed table.

The effective ions substitution was confirmed by the ICP analysis, where the typical Ca/P ratio of stoichiometric HA of 1,67 was shifted towards 1,78 for the N-HA, as proof of the successful Mg doping, and an even higher 1,85 for R-HA, consistently with the synergetic interaction of Mg and CO_3 towards the doping during the synthesis (Tab. 3.1).

Tab. 3.1 Ca/P and (Ca+Mg)/P ratios of N-HA and R-HA determined by ICP.

	Ca/P	(Ca+Mg)/P
N-HA	1,51±0,01	1,78±0,01
R-HA	1,55±0,00	1,85±0,00

SEM was used to assess morphology and particles dimensions (Fig. 3.6). As planned, N-HA resulted to be more crystalline and needle-like, with particles of almost 200 nm, while R-HA was proved to be amorphous and round-shaped, with particles of almost 80 nm. The two different morphologies were obtained thanks to the combined action of different temperature synthesis, and different combination of doping ions. The higher temperature (40°C) used for N-HA synthesis and the employment of the single doping ion Mg promoted the formation of a biomimetic poorly crystalline Mg-hydroxyapatite, but still clearly presenting the typical peaks of hydroxyapatite (Fig. 3.3) and the hydroxyapatite characteristic needle-like morphology. In R-HA instead, the use of a lower temperature (25°C) for the synthesis and the employment of two different doping ions, performing a concerted action in promoting the reciprocal inclusion in the crystal latex, resulted in a round-shaped amorphous calcium phosphate.
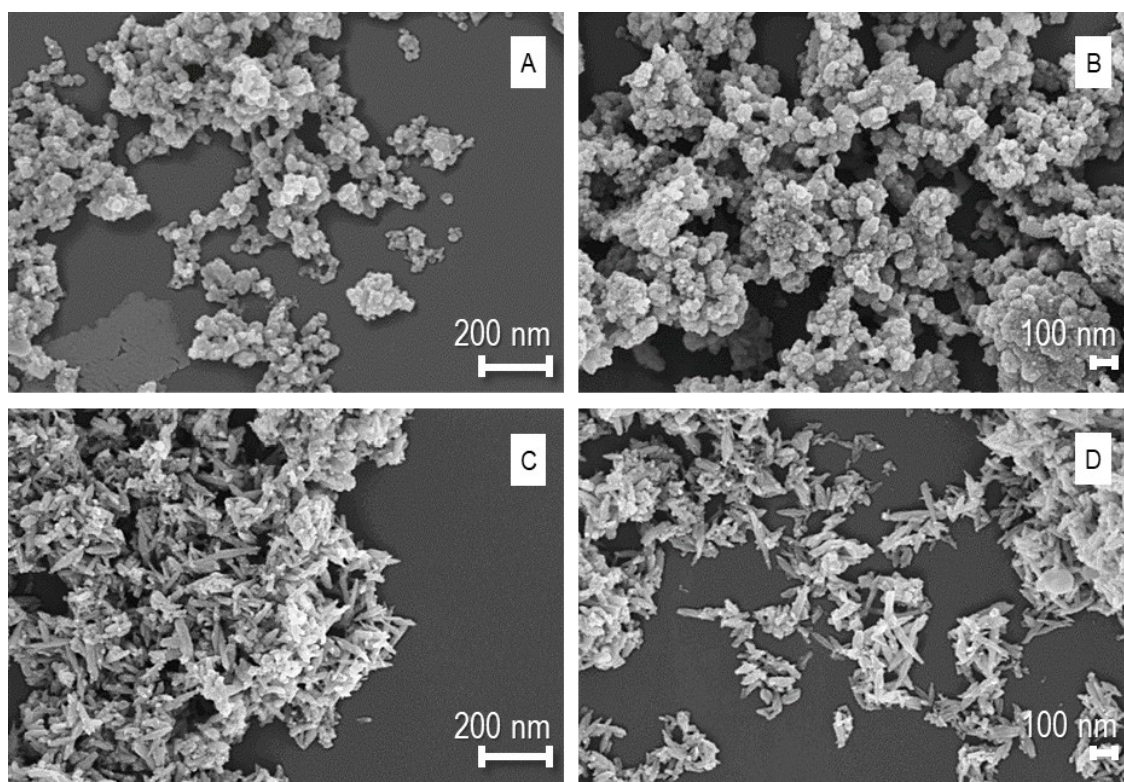

Fig. 3.6 Electron scanning microscopy of the needle-like N-HA (C, D) and the round-shaped R-HA (A, B) at different magnifications.

3.3.2 nHAs 2D cytotoxicity and biological activity evaluation

Before the realization of the bioinks, the cytotoxicity of the nHAs was tested as indirect cytotoxicity, using N-HA and R-HA leachate as conditioning medium to treat 2D culture of hBMSCs up to 7 days.

Viability and proliferation were assessed in BM as well as in OM. In BM viability at D7 resulted to be appropriate for all the conditions (Fig. 3.7 A, B, C), but better performances in terms of cells attachment and spreading were recorded for N-HA and R-HA leachate treated samples (Fig. 3.7 B and C respectively). A similar result was seen in OM, with smaller differences, though, between the CTRL and the nHAs leachate treated samples (Fig. 3.7 respectively D, E and F). Any significant difference was instead recorded among the two different kinds of nHAs.
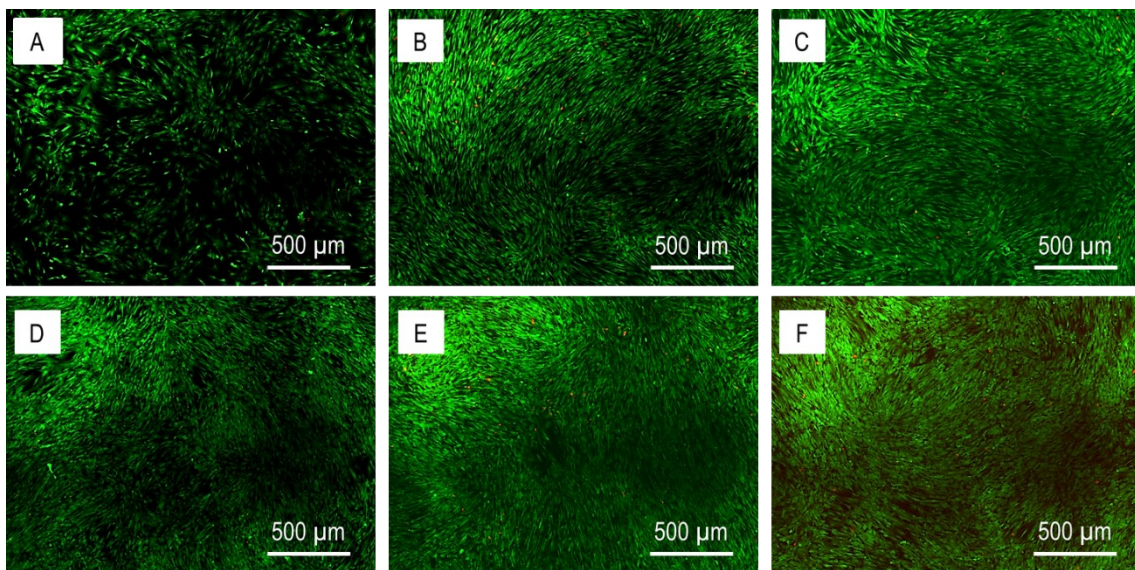
Fig. 3.7 L/D assay of 2D hBMSc culture in BM (A,B,C) and OM (D,E,F) at D7.

Proliferation confirmed viability data. A good proliferation was recorded both in BM and OM, with a faster proliferation rate recorded in OM compared to BM. In BM, nHAs leachate treated samples showed a slight better performance compared to the CTRL, wihile in OM no significant differences were recorded among the CTRl and the nHAs leachate treated samples. As for viability, also no differences were detected among the two different nHAs (Fig. 3.8 A, B).
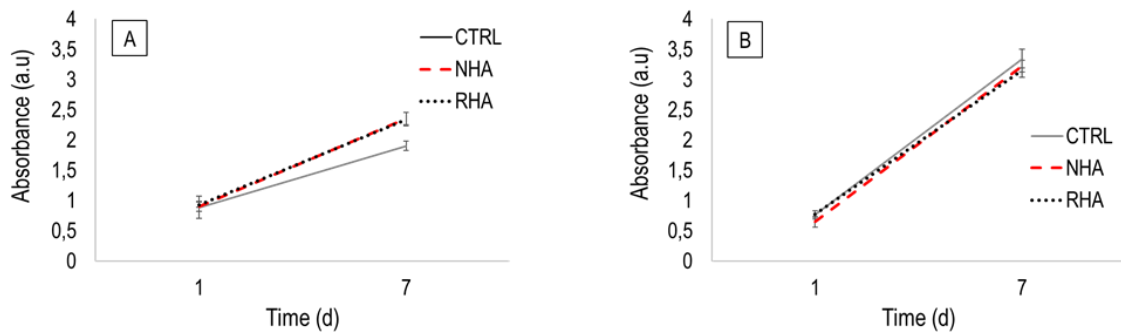
Fig. 3.8 Proliferation profile of hBMSCs 2D coltured with normal BM and OM (grey solid line A, B) compared to hBMSCs 2D coltured with BM and OM N-HA leachate (dashed red line A, B) and BM and OM R-HA leachate (dotted black line A, B)

As following step we wanted to evaluate their ability to induce biomineralized matrix production in cells.

Fig 3.9 Evaluation of biomineralization induction promote by N-HA and R-HA leachate at D21

The results showed a clear influence of the N-HA leachate treatment on biomineralization induction evaluated ad D21, with a consistent trend in BM and OM. In 2D colturing condition indeed, N-HA resulted to be promoting biomineralization in a more effective way compared to R-HA, independently of the me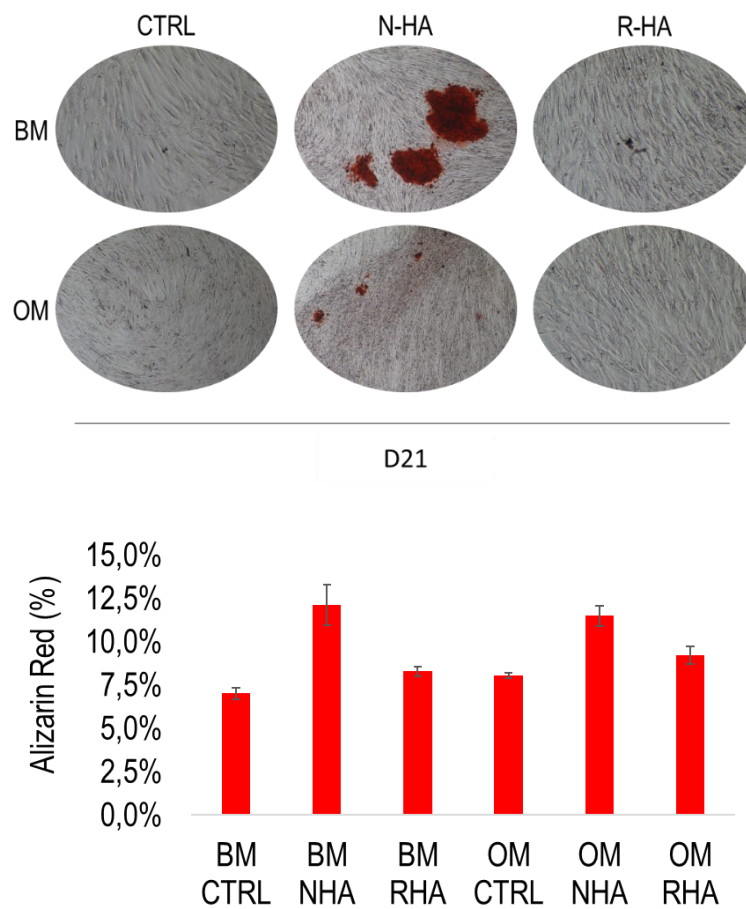dium (Fig. 3.9). Similar results on hBMSCs were reported by Sun and collaborators for fluoridate hydroxyapatite (F-HA)[51].

3.3.3 Bioinks formulation

Once proved the cytocompatibility of the produced nHAs as well as assess their ability to induce biomineralization in 2D conditions, we aimed for their inclusion in the bioink as nature inspired biomimetic inorganic phase in charge of providing cells with the correct cues and stimuli to differentiate and produce biomineralized extra-cellular matrix (ECM).

As matrix for the bioinks was selected, among all the possibilities, gelatine functionalized with methacryloyl groups (GelMA). This because of its collagen-derived nature, element naturally present and predominant in the natural occurring ECM[1,34], proven biocompatibility[36,38,39,52], but also and mainly for the possibility of crosslinking it with a relatively little known photoiniziator, litium-phenyl-2,4,6-trimethylbenzoylphospinate (LAP), endowed of the ability to perform a crosslinking reaction within the visible light region, providing unquestionable advantages over the more commonly used UV-photoiniziators[37,40,41,43,44,53]. Partially degraded non-modified gelatine was employed to improve the bioinks printability and reduce their cost. In particular, non-modified gelatine was dissolved in DMEM added with 1% P/S but not with 10% FBS in order to help avoiding contaminations and heated up at 80°C under magnetic stirring, covered to avoid evaporation, until perfect dissolution. On purpose, this process partially degrades gelatine structure, making it the perfect consistence to be used as sacrificial bioink-component to improve at best the printing process. Then, the bioink temperature was lowered to 45°C, to dissolve GelMA quickly and properly without denaturing it, so to preserve the supramolecular structure and composition of the effective matrix component. As last, temperature was once again lowered to 37°C, the physiological temperature, before adding 1% nHA (one kind of nHA for each bioink) dissolved in 1 mL of DMEM. In control sample, just 1 mL of

DMEM was added to compensate the volume. The bioink temperature was lowered to 37°C to preserve the nHAs structure before the printing process. Excessive temperature can indeed increase nHAs crystallinity degree, promote ions release and morphology changes[32,54–56]. nHAs dissolution in DMEM before the addition to the bioink was used to improve nHAs dispersion and bioink homogeneity. As last, 1 mL of LAP solution, previously prepared as sterile filtered mother solution at the concentration of 1 mg/mL, was added to the mixture, and the bioinks let mix for 1h at 37°C, to provide a proper mixing time, crucial to obtain the best printability. Due to LAP photosensitivity and its ability to perform crosslinking reactions within the visible light, all the preparation steps including LAP were strictly performed in the dark, to avoid any possible pre-crosslink of the hydrogel, that would impair the whole printing process, modifying the pre-hydrogel consistence before the extrusion. Once the bioink was perfectly mixed, it was transferred into a syringe and kept at 4°C overnight. After, it was heated up at 37°C for half an hour, mixed with cells using a double-syringes luer-locked system, and loaded into the printing cartridges. 37°C was determined to be the perfect temperature to make the bioinks fluid enough to be mixed with cells minimizing the stress by keeping them at physiological temperature during the whole preparation process. Moreover, at this temperature, any of the bioinks components would be altered. After this step, a thermal conditioning of the bioinks at 4°C for 18 minutes followed by 30 min at 26°C was performed to reach the perfect printability point. It is indeed well-known hydrogels memory and the influence of temperature on their behaviour[57–59].

3.3.3.1 Rheology

Viscometry test was performed on the inks to evaluate nHAs effect on the overall viscosity. Inks viscosity can be used as a good pre-screening parameter to evaluate the flow behaviour before the actual printing process[49,60,61].
At 27°C, all the inks showed a shear thinning behaviour, meaning a viscosity decrease contextually to a shear rate increment, the desired behaviour for a successful printing process, especially for bioinks, where the requirement for an excessive extrusion pressure will impair cells viability. Interestingly, it was possible to record a viscosity decrease linked to the nHAs addition to the inks, both for R-HA and N-HA, with a slight

better performance for N-HA compared to R-HA. This behaviour might be ascribable to a physical impairment of the temperature-dependent physical reversible crosslinking of GelMA, due to the nHAs particle presence but also to an alignment of the particles within the ink, more evident for N-HA ink, due to its needle like morphology (Fig. 3.10 and 3.6).
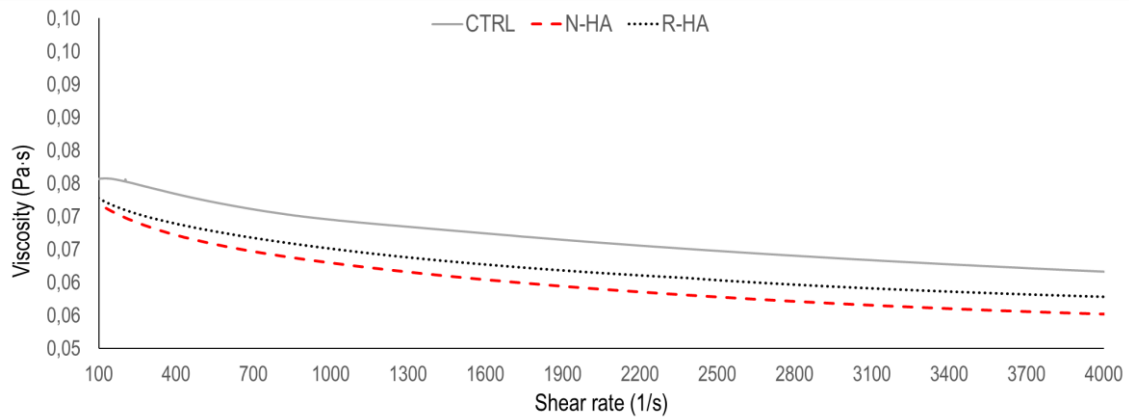
Fig. 3.10 Flow curves of CTRL, N-HA and R-HA inks.

3.3.3.2 Printability

Printability of the bioinks, most specifically in terms of extrudability, buildability, and model fidelity was evaluated (Fig. 3.11)[47,48,50,62]. All the tests were performed in absence of cells, as it was for rheology. Despite the huge number of methods reported in literature to evaluate printability of a given ink, with multiple variation even within the same typology of test, we opted for three main tests to assess the quality of our printing process: filament drop for extrudability, buildability for height maintenance and filament spreading for the model fidelity (Fig. 3.11)[37,47,49].
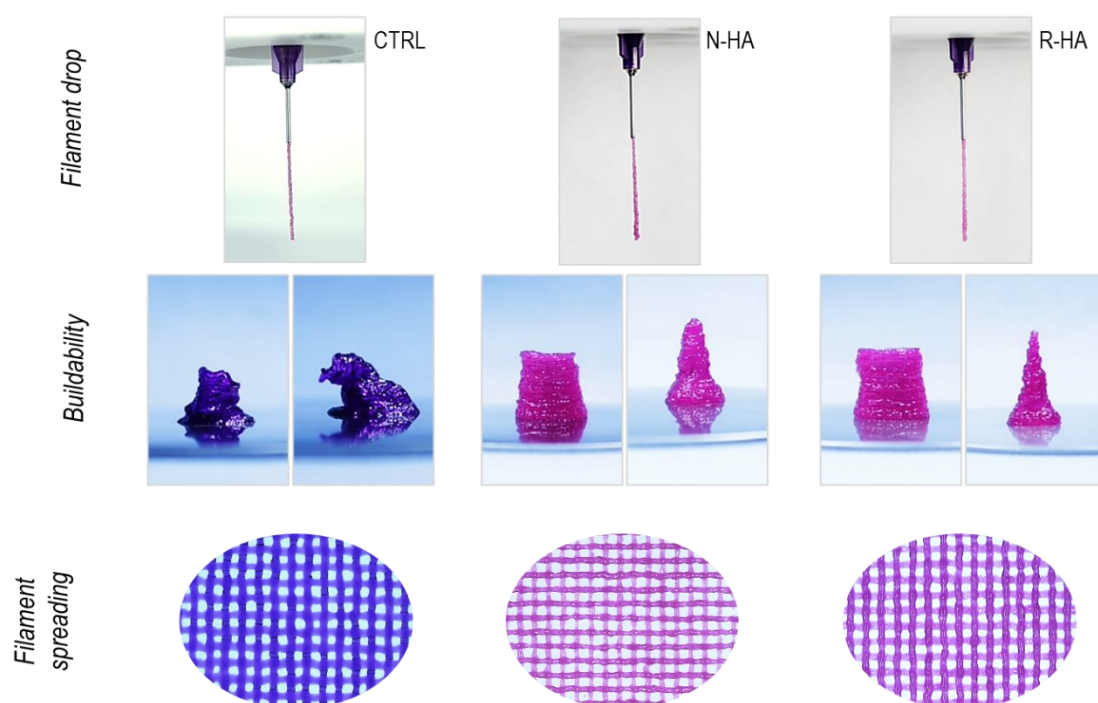
Fig. 3.11 Printability evaluation of CTRL, N-HA and R-HA inks, with filament drop, buildability and filament spreading tests.

A basic requirement of printability is the capability to achieve extrusion. The amount of pressure required to extrude a given bioink using a given printing system can be referred to as that system's extrudability. Extrudability primarily affects cell viability and total print time. Extrudability for the developed bioinks was assessed by a filament drop test. An appropriate ink flow, consistent with the nozzle diameter, not

swelling, curling or dripping, is important to obtain high model fidelity. This depends on many different parameters, like the use of an appropriate needle or nozzle type and diameter for the ink meant to be printed, as well as the correct extrusion pressure, speed deposition and ink printing temperature and pre-thermal conditioning. Filament drop can be employed as qualitative test to pre-screen the inks before the actual printing, extruding a filament in the air and observing its behaviour. A straight uniform filament, fitting the nozzle diameter, with a constant behaviour throughout extrusion can be considered a good starting parameter for a subsequent appropriate printing. For the bioinks prepared the filament drop test resulted to be appropriate, with a behaviour fitting all the theoretical expectations.

After, buildability was tested (Fig. 3.11). The ability of a bioink to maintain its height upon deposition of multiple layers is also a key factor in its printability. The larger a construct becomes, the more critical this aspect of shape fidelity is. As more layers are added to a single construct, the weight experienced by the lower layers increases[50]. To evaluate this aspects, two geometrically different structures were used for the test: a 10 mm x 20 mm cylinder and a 10 mm x 20 mm cone. What was possible to assess, was the structures printed with the control ink, meaning the matrix in absence of nHAs, were poorly buildable, collapsing quite early during the printing process, that was never able to be ended with success over the different attempts performed. On the contrary, the addition of only 1% of nHAs, was proven to be crucial for implementing the buildability power of the ink. Both N-HA and R-HA significantly improved the buildability, allowing construction of both the geometrical shapes with good accuracy and minimum defects.

Model fidelity and printing accuracy were then evaluated by means of a filament spreading test (Fig. 3.11 and Fig. 3.12). More precisely, a two-layer construct was printed, and the pores size and shape fidelity compared to the designed model quantify through a dedicated software for images elaboration.
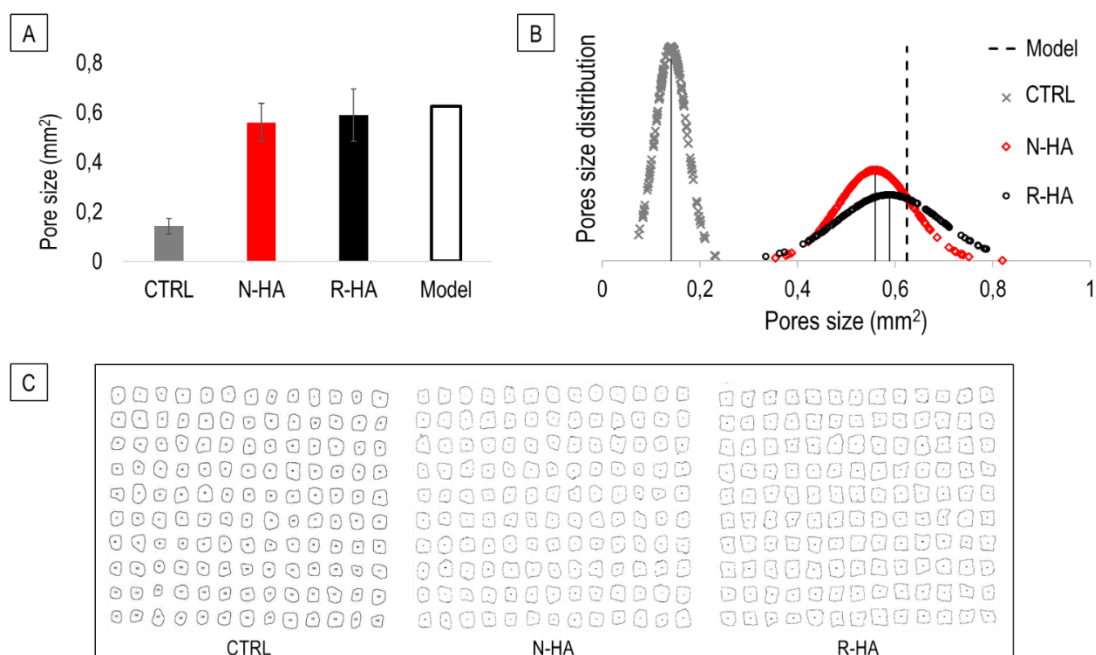
Fig. 3.12 Filament spreading profiles for CTRL, N-HA and R-HA inks. CTRL, N-HA and R-HA 3D printed scaffolds pores size comparison with the model (A, B), pores size normal distribution (B) and pores shape profile (C).

The outcomes were consistent with the buildability. CTRL sample showed a poor model fidelity, with irregular pores in size and shape. On the contrary, addition of 1% nHAs significantly improved shape fidelity, with no significant differences among N-HA and R-HA.

3.3.4 Three-dimensional bioprinted scaffolds biological characterization

Once assessed the cytocompatibility of the synthetized nHAs, their ability of inducing biomineralization and their performance in terms of printability when included into an ink, we moved to the effective 3D bioprinting of hBMSCs. For the printing, a concentration of 5 mln/mL of cells was chosen, based on some interesting work present in literature proving the importance of cells concentration in three-dimensional bioprinting[36,63–67]. LAP concentration of 1 mg/mL and light exposure parameters in terms of time and distance, were selected after multiple pilot studies performed to find the perfect combination between stiffness, degradation rate and cells viability.

Cells viability was assessed by LD assay at D1, D7, D14 and D21 (Fig. 3.13). A similar behaviour in the different samples, meaning CTRL, N-HA and R-HA was observed towards the different time points. In BM as well as in OM, at D1, was possible to see an even cells distribution within the filaments and the structure, confirmation of an appropriate cell mixing during the bioink preparation, with just few dead cells, proof of a correct combination of LAP concentration and light exposure. At D7, in both BM and OM, in all the samples, was possible to notice a higher number of dead cells, probably connected with the stress undergone by the cells during the printing process. Nevertheless, in all the medium conditions, the alive cells appeared elongated, proof of an early-stage cells spreading. At D14 significant differences were encountered between BM and OM cultured scaffolds. In BM viability was good and cell spreading was improved compared to D7, but cells resulted to be still quite distant among each other while in OM cells heavily colonized the filaments, protruding towards each other, and creating connections, with almost no dead cells detectable. This difference was maintained at D21. Viability was still good in BM, but the spreading wasn't significantly improved compared to D14. In OM instead, cells started to leave the filament and creating networks between the filaments, consistently colonizing the scaffolds.
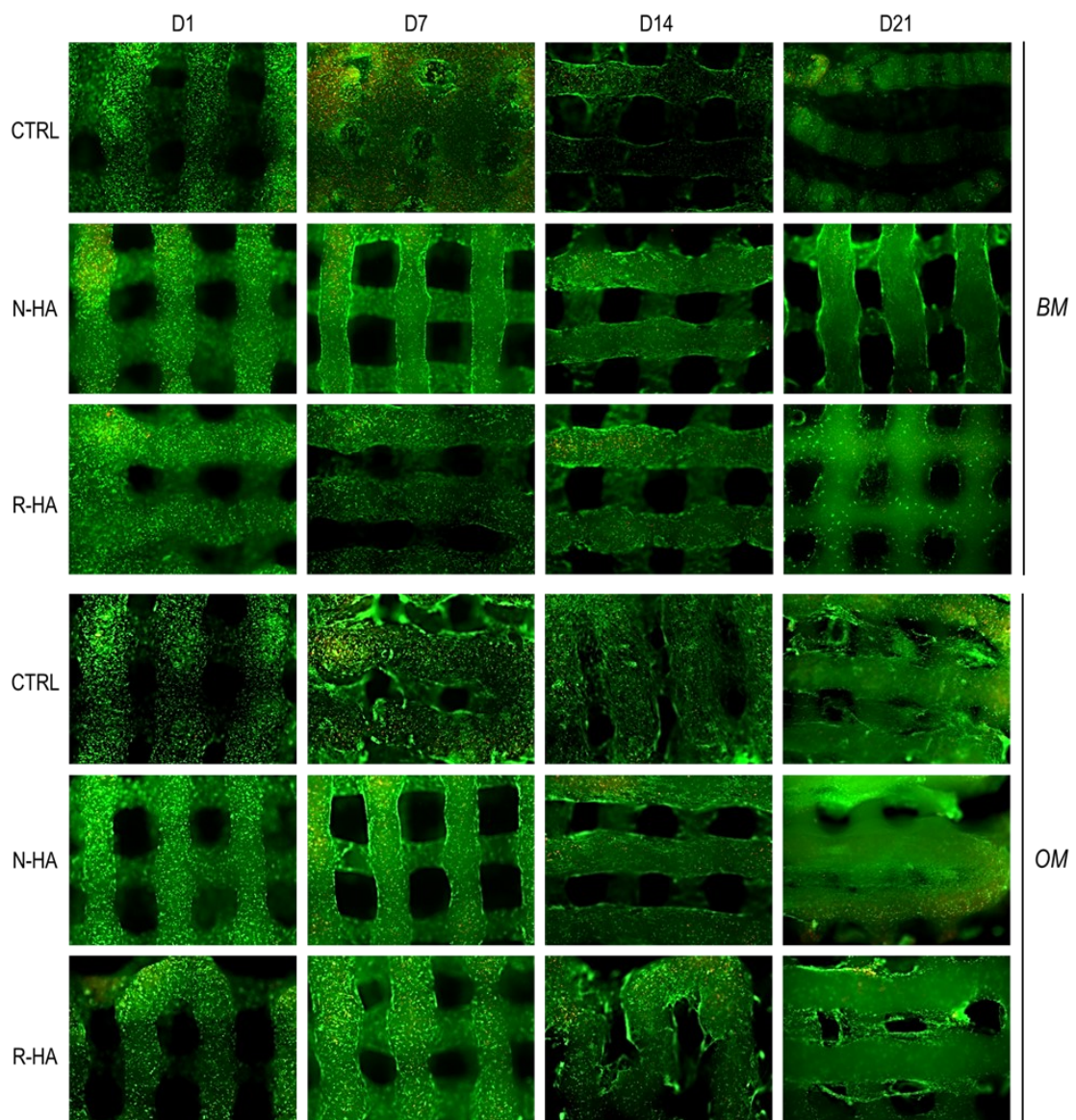
Fig. 3.13 LD assay of 3D bioprinted CTRL, N-HA and R-HA hBMSCs loaded bioinks coltured in BM and OM, at D1, D7, D14 and D21.

Proliferation confirmed the viability data (Fig. 3.14). At D7 it was encountered a decrese in cells proliferating activity, apparently less evident (Fig. 3.14 A) or even not recorded (Fig. 3.14 B) for the CTRL samples, so that the reason might be ascribable to a higher printing-related mechanical stress underwent by the cells loaded into nHAs functionalized bioinks because of the presence of the inorganic phase. At D14 though, proliferation was increased for all samples in all the conditions, with an apparent boostering effect due to the N-HA presence in BM. At D21 proliferation for nHAs samples resulted to be better (Fig. 3.14 A) or, at worst, equal (Fig. 3.14 B) to the

CTRL samples, indicating a positive effect of the bioinks functionalization with nHAs towards this aspect.
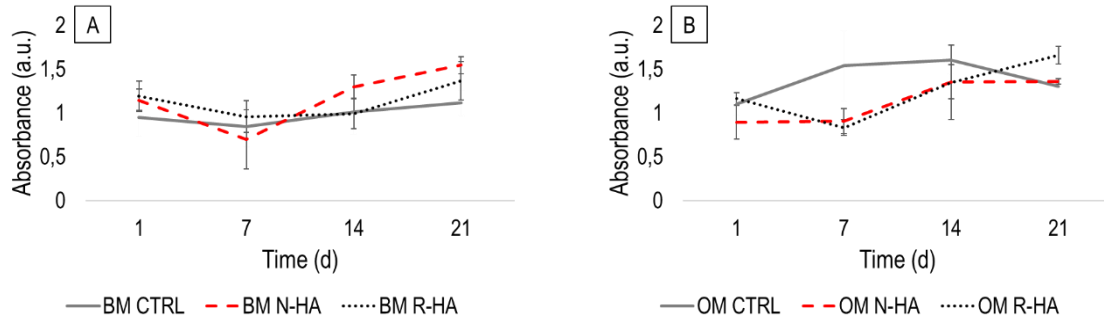
Fig. 3.14 Proliferation profile of hBMSCs within CTRL (continuous grey line), N-HA (red dashed line) and R-HA (black dotted line) 3D bioprinted scaffolds, coltured in BM (A) and OM (B).

Moreover, with the chosen parameters of LAP concentration and light exposure, the 3D bioprinted structures were perfectly maintaining their shape and consistence up to 21 days, both in BM and OM (Fig. 3.15).
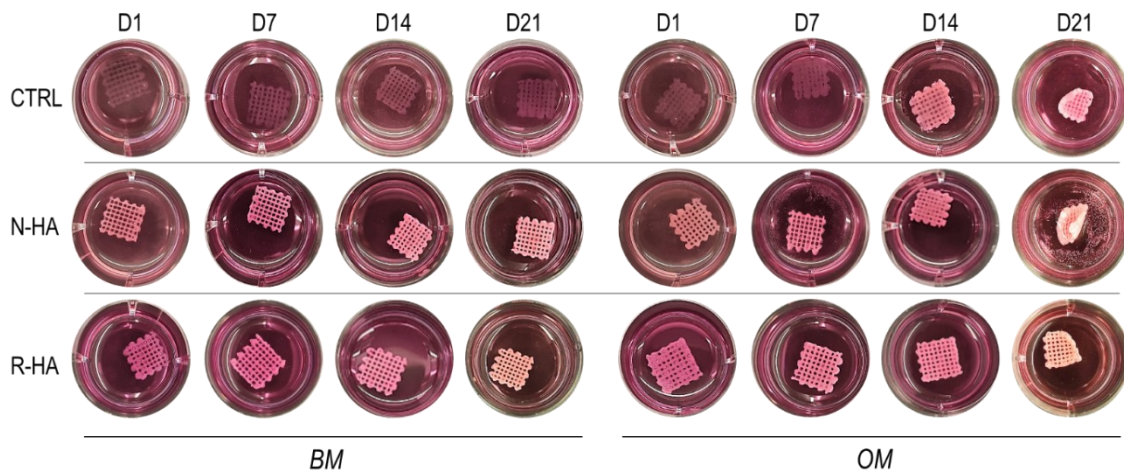
Fig. 3.15 Stability of CTRL, N-HA and R-HA 3D bioprinted scaffolds at D1, D7, D14 and D21 in BM and OM.

It was interestingly possible to observe a change in colour among D7 and D14 in the CTRL sample in OM (Fig. 3.15), ascribable to the strong cell spreading and scaffold

colonization proven also by the LD assay and proliferation test, same reason to which it was possible to ascribe the evident scaffolds curling in OM at D21 for all the samples. The fact the colour change was detectable in the CTRL sample while not in the N-HA or R-HA sample is attributable to the transparent colour of the CTRL compared to the white starting colour of the samples containing nHAs.

Immunostaining was then performed to assess the expression of the runt homology domain-X2 (RunX2) transcription factor as early differentiation marker at D7 (Fig. 3.16) and the small non-collagenous protein hormone osteocalcin (Ocn) as late differentiation marker at D21 (Fig. 3.17).

Fig. 3.16 Immunostaining of CTRL, N-HA and R-HA 3D bioprinted scaffolds at D7 for evaluation of the early differentiation marker RunX2 (green). Red and blue staining correspond respectively to cells cytoskeleton and nuclei.

At D7, it was possible to detect RunX2 expression in all the samples, CTRL included, localized in the nuclei and cytoplasm. Despite RunX2 normally colocalizes with the nuclei, the dynamics of RunX2 distribution and compartmentalization between the cytoplasm and nucleus is little understood. The activity of RunX2 is regulated by tissue-specific expression and post-translational modifications, as well as modules that control its subcellular localization. It has been proved that microtubule stabilization perturbs nuclear localization of the lineage-specific

transcription factor RunX2[51,63,68,69]. Its localization in both the nuclei and the cytoplasm might so be attributable to this change in microtubule organization, maybe triggered by the printing process[68]. Nevertheless, additional studies are required to prove this connection. The presence of this early differentiation marker in the CTRL samples instead might be attributable mechanical stress undergone by the cells during the printing process, which provoked stimuli that triggered the hBMSCs differentiation[70].
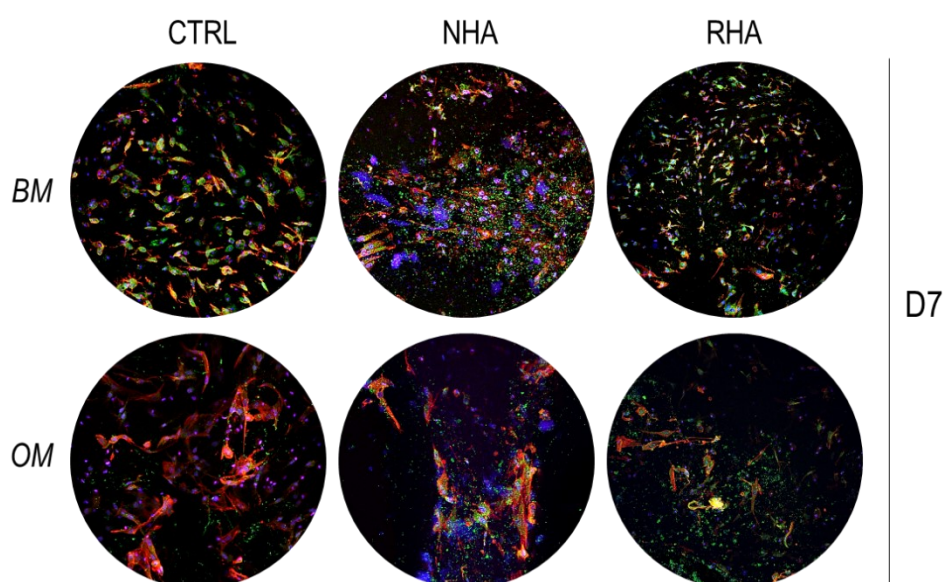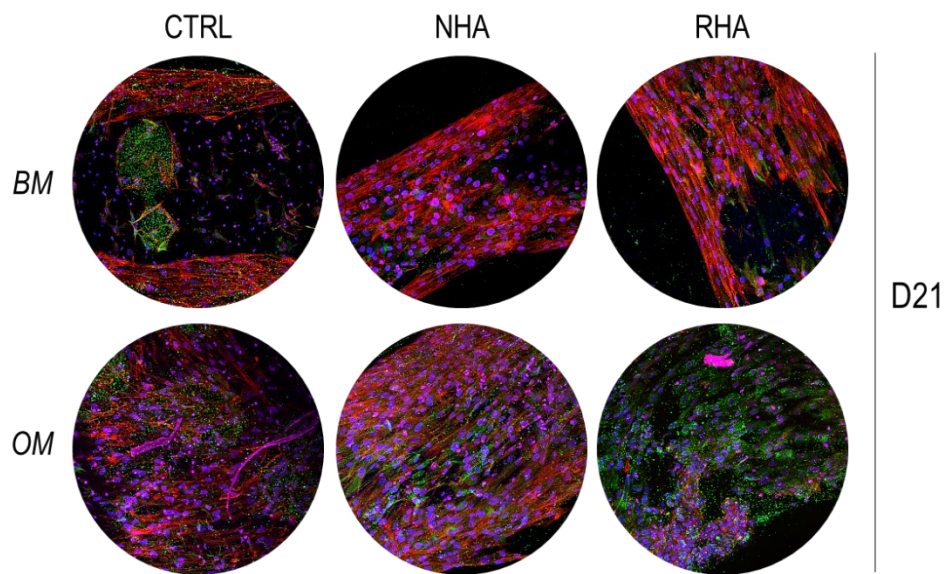

Fig. 3.17 Immunostaining of CTRL, N-HA and R-HA 3D bioprinted scaffolds at D21 for evaluation of the late differentiation marker osteocalcin (green). Red and blue staining correspond respectively to cells cytoskeleton and nuclei.

As for RunX2, Ocn was detected in all the samples (Fig. 3.17), CTRLs included. Ocn is the most abundant non-collagenous bone protein, secreted solely by osteoblasts and thought to play a role in the body's metabolic regulation. This means Ocn detection correlates with osteoblasts presence, clearly indicating a successful differentiation process. In its carboxylated form it binds calcium directly and thus concentrates in bone while in its uncarboxylated form, osteocalcin is secreted and acts as a hormone in the body, signalling in the pancreas, fat, muscle, testes, and brain[69,71,72].

Once again, Ocn expression was recorded in all the analysed samples, CTRLs included. Since also RunX2 expression was observed in the CTRLs samples, it is reliable that the differentiation process continued towards reaching Ocn expression in later time points, more specifically, in this case, at D21.

Since the expression of both the target differentiation markers was detected in all the samples, starting with RunX2 at D7 to Ocn at D21, with no appreciable differences between the CTRLs and the samples containing nHAs, it is so far not possible to correlate specifically their expression with the presence of the inorganic phase into the bioinks. Based on the collected data, it is more reliable assuming that, for the nHAs concentration used, the contribution of the inorganic phase in the differentiation process is not discernible from the general differentiation most likely provoked by the printing process itself, that would explain the presence of differentiation markers also in the CTRLs sample. Another factor that might have played a role in these outcomes, is the cells stage. Since passage-four cells from a human donor were used as starting cells for the creation of the bioinks, a general differentiation might also be occurred due to this aspect. However, further studies are required to better understand into these aspects.

3.4. Conclusions

In conclusions, three-dimensional bioprinting of biomimetic nano-hydroxyapatite functionalized GelMA-based bioinks for bone tissue engineering was successfully performed. More specifically, three GelMA based bioinks for hBMSCs bioprinting were successfully developed. Two morphologically and physiochemically differently designed nature inspired and biomimetic inorganic phases were profitably synthetized, their cytocompatibility proved and their ability to induce biomineralization assessed. Rheology demonstrated the shear thinning behaviour of the developed bioinks and the ability of the nHAs to reduce the bioink viscosity, promoting extrudability, a key parameter for a successful bioprinting. An appropriate balance between GelMA, nHAs and LAP concentration as well as a suitable visible light exposure to obtain cytocompatible and stable three-dimensional bioprinted scaffolds was obtained. The nHAs inclusion into the bioinks formulation resulted into a significant improvement of the overall printability and the derived scaffolds were proven to be stable up to 21 days. Viability and proliferation of hBMSCs within the bioinks were proved to be really promising in all the condition tested, with significant improvements in proliferation related to the nHAs presence. Early and late cells differentiation was proved to be occurring in the samples, even if not strictly related with the nHAs presence, and most probably generally induced by the mechanical stress undergone by the cells during the printing process as well as by the relatively late passage of the cells used into the bioinks formulation. A deeper investigation of this aspect is though required to have a better understanding of the obtained outcomes. As next step, attention will be given to the differentiation aspects, testing multiple markers and different cells types. Moreover, evaluation of the mechanical performances of the scaffolds with and without nHAs within the different time points will be performed, so to assess the influence of the inorganic phases as well as of the cell growth spreading and differentiation on this aspect. Nevertheless, this work paves the way to an innovative bioinspired three-dimensional bioprinting of hBMSCs, featuring as really promising for bone tissue engineering and regeneration.

References

1.   Sprio, S., Sandri, M., Panseri, S., Cunha, C. & Tampieri, A. Hybrid scaffolds for tissue regeneration: Chemotaxis and physical confinement as sources of biomimesis. *J. Nanomater.* **2012**, (2012).

2.   Tampieri, A. *et al.* Biologically inspired synthesis of bone-like composite: Self-assembled collagen fibers/hydroxyapatite nanocrystals. *J. Biomed. Mater. Res. - Part A* **67**, 618–625 (2003).

3.   Weiner, S. & Wagner, H. D. The material bone: Structure-mechanical function relations. *Annu. Rev. Mater. Sci.* **28**, 271–298 (1998).

4.   Weiner, S. An Overview of Biomineralization Processes and the Problem of the Vital Effect. *Rev. Mineral. Geochemistry* **54**, 1–29 (2003).

5.   Calvi, L. M. *et al.* Osteoblastic cells regulate the haematopoietic stem cell niche. *Nature* **425**, 841–846 (2003).

6.   Schinke, T. *et al.* Impaired gastric acidification negatively affects calcium homeostasis and bone mass. *Nat. Med.* **15**, 674–681 (2009).

7.   White, K. E. *et al.* Autosomal dominant hypophosphataemic rickets is associated with mutations in FGF23. *Nat. Genet.* **26**, 345–348 (2000).

8.   Wegst, U. G. K., Schecter, M., Donius, A. E. & Hunger, P. M. Biomaterials by freeze casting. *Philos. Trans. R. Soc. A Math. Phys. Eng. Sci.* **368**, 2099–2121 (2010).

9.   Amy CY Lo, F. S. Collagen-Based Scaffolds for Cell Therapies in the Injured Brain. *J. Stem Cell Res. Ther.* **05**, (2015).

10.   Macaya, D. J., Hayakawa, K., Arai, K. & Spector, M. Astrocyte infiltration into injectable collagen-based hydrogels containing FGF-2 to treat spinal cord injury. *Biomaterials* **34**, 3591 (2013).

11.   Gonzalez-Fernandez, T. *et al.* Pore-forming bioinks to enable spatio-temporally defined gene delivery in bioprinted tissues. *J. Control. Release* **301**, 13–27 (2019).

12.	Furlani, F. *et al.* Biomimetic, Multiresponsive, and Self-Healing Lactose-Modified Chitosan (CTL)-Based Gels Formed via Competitor-Assisted Mechanism. *ACS Biomater. Sci. Eng.* 5539–5547 (2019) doi:10.1021/acsbiomaterials.9b01256.

13.	Mao, A. S. & Mooney, D. J. Regenerative medicine: Current therapies and future directions. *Proc. Natl. Acad. Sci. U. S. A.* **112**, 14452–14459 (2015).

14.	Luo, H. *et al.* Advances in tissue engineering of nanocellulose-based scaffolds: A review. *Carbohydr. Polym.* **224**, 115144 (2019).

15.	Wang, B. *et al.* Hybrid scaffolds enhanced by nanofibers improve in vitro cell behavior for tissue regeneration. *Cellulose* **25**, 7113–7125 (2018).

16.	Daly, A. C. & Kelly, D. J. Biofabrication of spatially organised tissues by directing the growth of cellular spheroids within 3D printed polymeric microchambers. *Biomaterials* **197**, 194–206 (2019).

17.	Xia, Z., Jin, S. & Ye, K. Tissue and Organ 3D Bioprinting. *SLAS Technol.* **23**, 301–314 (2018).

18.	Wang, S., Hashemi, S., Stratton, S. & Arinzeh, T. L. The Effect of Physical Cues of Biomaterial Scaffolds on Stem Cell Behavior. *Adv. Healthc. Mater.* **10**, 1–23 (2021).

19.	Weber, F. E. Reconsidering Osteoconduction in the Era of Additive Manufacturing. *Tissue Eng. - Part B Rev.* **25**, 375–386 (2019).

20.	Li, C. *et al.* "The return of ceramic implants": Rose stem inspired dual layered modification of ceramic scaffolds with improved mechanical and anti-infective properties. *Mater. Sci. Eng. C* **93**, 873–879 (2018).

21.	Gu, B. K., Choi, D. J., Park, S. J., Kim, Y. & Kim, C. *Cutting-Edge Enabling Technologies for Regenerative Medicine. Cutting-Edge Enabling Technologies for Regenerative Medicine. Advances in Experimental Medicine and Biology* vol. 1078 (2018).

22.	Bose, S., Ke, D., Sahasrabudhe, H. & Bandyopadhyay, A. Additive manufacturing of biomaterials. *Prog. Mater. Sci.* **93**, 45–111 (2018).

23. Slots, C. *et al.* Simple additive manufacturing of an osteoconductive ceramic using suspension melt extrusion. *Dent. Mater.* **33**, 198–208 (2017).

24. Freeman, F. E. *et al.* Biofabrication of multiscale bone extracellular matrix scaffolds for bone tissue engineering. *Eur. Cells Mater.* **38**, 168–187 (2019).

25. Huang, T. *et al.* 3D-printed scaffolds of biomineralized hydroxyapatite nanocomposite on silk fibroin for improving bone regeneration. *Appl. Surf. Sci.* **467–468**, 345–353 (2019).

26. Malda, J. *et al.* 25th anniversary article: Engineering hydrogels for biofabrication. *Adv. Mater.* **25**, 5011–5028 (2013).

27. Castilho, M. *et al.* Multitechnology Biofabrication: A New Approach for the Manufacturing of Functional Tissue Structures? *Trends Biotechnol.* **38**, 1316–1328 (2020).

28. Melchels, F. P. W. *et al.* Additive manufacturing of tissues and organs. *Prog. Polym. Sci.* **37**, 1079–1104 (2012).

29. Pina, S. *et al.* Regenerative Medicine Applications. *Materials (Basel).* **12**, 1824 (2019).

30. Groll, J. *et al.* A definition of bioinks and their distinction from biomaterial inks. *Biofabrication* **11**, (2019).

31. Groll, J. *et al.* Biofabrication: Reappraising the definition of an evolving field. *Biofabrication* **8**, (2016).

32. Olszta, M. J. *et al.* Bone structure and formation: A new perspective. *Mater. Sci. Eng. R Reports* **58**, 77–116 (2007).

33. Guarino, V. *et al.* Needle-like ion-doped hydroxyapatite crystals influence osteogenic properties of PCL composite scaffolds. *Biomed. Mater.* **11**, (2016).

34. Tampieri, A. *et al.* Design of graded biomimetic osteochondral composite scaffolds. *Biomaterials* **29**, 3539–3546 (2008).

35. Landi, E. *et al.* Biomimetic Mg- and Mg,CO3-substituted hydroxyapatites: synthesis characterization and in vitro behaviour. *J. Eur. Ceram. Soc.* **26**, 2593–

2601 (2006).

36. Spencer, A. R. *et al.* Bioprinting of a Cell-Laden Conductive Hydrogel Composite. *ACS Appl. Mater. Interfaces* **11**, 30518–30533 (2019).

37. Tigner, T. J., Rajput, S., Gaharwar, A. K. & Alge, D. L. Comparison of Photo Cross Linkable Gelatine Derivatives and Initiators for Three-Dimensional Extrusion Bioprinting. *Biomacromolecules* **21**, 454–463 (2020).

38. Zhou, F. *et al.* Rapid printing of bio-inspired 3D tissue constructs for skin regeneration. *Biomaterials* **258**, 120287 (2020).

39. Spencer, A. R. *et al.* Electroconductive Gelatine Methacryloyl-PEDOT:PSS Composite Hydrogels: Design, Synthesis, and Properties. *ACS Biomater. Sci. Eng.* **4**, 1558–1567 (2018).

40. Vaudreuil, N. *et al.* Photopolymerizable biogel scaffold seeded with mesenchymal stem cells: safety and efficacy evaluation of novel treatment for intervertebral disc degeneration. *J. Orthop. Res.* **37**, 1451–1459 (2019).

41. Xu, H., Casillas, J., Krishnamoorthy, S. & Xu, C. Effects of Irgacure 2959 and lithium phenyl-2,4,6-trimethylbenzoylphosphinate on cell viability, physical properties, and microstructure in 3D bioprinting of vascular-like constructs. *Biomed. Mater.* **15**, (2020).

42. Noè, C., Tonda-Turo, C., Chiappone, A., Sangermano, M. & Hakkarainen, M. Light processable starch hydrogels. *Polymers (Basel).* **12**, 1359 (2020).

43. Nguyen, A. K., Goering, P. L., Elespuru, R. K., Das, S. S. & Narayan, R. J. The photoinitiator lithium phenyl (2,4,6-Trimethylbenzoyl) phosphinate with exposure to 405 nm light is cytotoxic to mammalian cells but not mutagenic in bacterial reverse mutation assays. *Polymers (Basel).* **12**, 1–13 (2020).

44. Monteiro, N. *et al.* Photopolymerization of cell-laden gelatine methacryloyl hydrogels using a dental curing light for regenerative dentistry. *Dent. Mater.* **34**, 389–399 (2018).

45. Nguyen, A. K., Goering, P. L., Reipa, V. & Narayan, R. J. Toxicity and photosensitizing assessment of gelatine methacryloyl-based hydrogels

photoinitiated with lithium phenyl-2,4,6-trimethylbenzoylphosphinate in human primary renal proximal tubule epithelial cells. *Biointerphases* **14**, 021007 (2019).

46. Landi, E. *et al.* Biomimetic Mg-substituted hydroxyapatite: From synthesis to in vivo behaviour. *J. Mater. Sci. Mater. Med.* **19**, 239–247 (2008).

47. Ribeiro, A. *et al.* Assessing bioink shape fidelity to aid material development in 3D bioprinting. *Biofabrication* **10**, (2018).

48. Hölzl, K. *et al.* Bioink properties before, during and after 3D bioprinting. *Biofabrication* **8**, (2016).

49. Schwab, A. *et al.* Printability and Shape Fidelity of Bioinks in 3D Bioprinting. *Chem. Rev.* **120**, 11028–11055 (2020).

50. Gillispie, G. *et al.* Assessment methodologies for extrusion-based bioink printability. *Biofabrication* **12**, (2020).

51. Sun, J., Wu, T., Fan, Q., Hu, Q. & Shi, B. Comparative study of hydroxyapatite, fluor-hydroxyapatite and Si-substituted hydroxyapatite nanoparticles on osteogenic, osteoclastic and antibacterial ability. *RSC Adv.* **9**, 16106–16118 (2019).

52. Schuurman, W. *et al.* Gelatine-methacrylamide hydrogels as potential biomaterials for fabrication of tissue-engineered cartilage constructs. *Macromol. Biosci.* **13**, 551–561 (2013).

53. Kuang, B., Yang, Y. & Lin, H. Infiltration and In-Tissue Polymerization of Photocross-Linked Hydrogel for Effective Fixation of Implants into Cartilage-An in Vitro Study. *ACS Omega* **4**, 18540–18544 (2019).

54. Campodoni, E. *et al.* Development of innovative hybrid and intrinsically magnetic nanobeads as a drug delivery system. *Nanomedicine* **11**, 2119–2130 (2016).

55. Bassett, D. C., Marelli, B., Nazhat, S. N. & Barralet, J. E. Stabilization of amorphous calcium carbonate with nanofibrillar biopolymers. *Adv. Funct. Mater.* **22**, 3460–3469 (2012).

56. Zhou, L. *et al.* Biomimetic mineralization of anionic gelatine hydrogels: Effect of degree of methacrylation. *RSC Adv.* **4**, 21997–22008 (2014).

57. Zhang, X. *et al.* Optically- and thermally-responsive programmable materials based on carbon nanotube-hydrogel polymer composites. *Nano Lett.* **11**, 3239–3244 (2011).

58. Ryan, K. R., Down, M. P. & Banks, C. E. Future of additive manufacturing: Overview of 4D and 3D printed smart and advanced materials and their applications. *Chem. Eng. J.* **403**, 126162 (2021).

59. Huang, R., Zheng, S., Liu, Z. & Ng, T. Y. *Recent Advances of the Constitutive Models of Smart Materials - Hydrogels and Shape Memory Polymers*. *International Journal of Applied Mechanics* vol. 12 (2020).

60. Abdollahiyan, P., Oroojalian, F., Mokhtarzadeh, A. & de la Guardia, M. Hydrogel-Based 3D Bioprinting for Bone and Cartilage Tissue Engineering. *Biotechnol. J.* **15**, 1–16 (2020).

61. Ojansivu, M. *et al.* Wood-based nanocellulose and bioactive glass modified gelatine-alginate bioinks for 3D bioprinting of bone cells. *Biofabrication* **11**, 35010 (2019).

62. Erkoc, P. *et al.* Photocurable pentaerythritol triacrylate/lithium phenyl-2,4,6-trimethylbenzoylphosphinate-based ink for extrusion-based 3D printing of magneto-responsive materials. *J. Appl. Polym. Sci.* **137**, 1–10 (2020).

63. Rathan, S. *et al.* Fiber Reinforced Cartilage ECM Functionalized Bioinks for Functional Cartilage Tissue Engineering. *Adv. Healthc. Mater.* **8**, 1–11 (2019).

64. Levato, R. *et al.* From Shape to Function: The Next Step in Bioprinting. *Adv. Mater.* **32**, (2020).

65. Mandrycky, C., Wang, Z., Kim, K. & Kim, D. H. 3D bioprinting for engineering complex tissues. *Biotechnol. Adv.* **34**, 422–434 (2016).

66. Bernal, P. N. *et al.* Volumetric Bioprinting of Complex Living-Tissue Constructs within Seconds. *Adv. Mater.* **31**, (2019).

67. Matai, I., Kaur, G., Seyedsalehi, A., McClinton, A. & Laurencin, C. T. Progress in

3D bioprinting technology for tissue/organ regenerative engineering. *Biomaterials* **226**, 119536 (2020).

68. Pockwinse, S. M. *et al.* Microtubule-dependent nuclear-cytoplasmic shuttling of Runx2. *J. Cell. Physiol.* **206**, 354–362 (2006).

69. Feng, X., Wu, Y., Bao, F., Chen, X. & Gong, J. Comparison of 3D-printed mesoporous calcium silicate/polycaprolactone and mesoporous Bioacive glass/polycaprolactone scaffolds for bone regeneration. *Microporous Mesoporous Mater.* **278**, 348–353 (2019).

70. Adhikari, J. *et al.* Effects of Processing Parameters of 3D Bioprinting on the Cellular Activity of Bioinks. *Macromol. Biosci.* **21**, (2021).

71. Ferron, M. & Lacombe, J. Regulation of energy metabolism by the skeleton: Osteocalcin and beyond. *Arch. Biochem. Biophys.* **561**, 137–146 (2014).

72. Hosseini, S. *et al.* C-terminal amidation of an osteocalcin-derived peptide promotes hydroxyapatite crystallization. *J. Biol. Chem.* **288**, 7885–7893 (2013).

CHAPTER 4

In-vivo injectable and in-situ crosslinkable gelatine-PEDOT:PSS electroconductive hydrogels for neural tissue regeneration

4.1 Introduction

Hydrogels are highly hydrated networks widely used for most diverse applications, spanning from biomedicine to soft electronics[1–3]. Some of their most advanced and studied applications can be found within the biomedical field, as injectable sensors and scaffolds for regenerative medicine[1,2,4–6]. It has already been discussed how regenerative medicine relies on creation of suitable networks able to mimic natural tissues properties, like biochemical milieu, spatial composition, and mechanical performances[2,7].

In humans, neural tissue is responsible for regulation and control of the body functions through electrochemical stimuli. It is divided into central neural system (CNS) and peripheral neural system (PNS) and it is featured by a very poor regenerative potential[8]. As for all the other human tissues, collagen is the main component or the extra-cellular matrix (ECM) of the neural tissue[9].

Unfortunately, as previously mentioned, collagen is highly structured, expensive, and difficult to handle since it is insoluble in physiological conditions of pH, temperature and osmolarity. As consequence, once again, among all the possible naturally occurring polymers possible to be exploited for the purpose[10–14], we found in gelatinee, the best candidate to rely-on for the creation of a biomimetic engineered tool suitable for neural tissue regeneration.

Recently, great efforts were devoted to develop electroconductive biomaterials suitable for regeneration of electroconductive tissues, like nervous and muscular tissues[15–20]. More in detail, conductive materials emerged as able to enhance cell adhesion, cell growth, differentiation of neural stem cells towards neurons and astrocytes, and formation of neuronal networks[21–24]. Indeed, nervous tissue is frequently damaged by trauma and diseases and display poor self-healing ability[11,25].

Thus, different conductive polymers, meaning polymers able to conduct electrons, among which poly(3,4-ethylenedioxythiophene) (PEDOT), poly-pyrrole, and poly-aniline, were extensively studied[15,26–30]. Despite these polymers can be exploited to fabricate mainly films[31,32], they were also combined with different materials in order to design hybrid conductive biomaterials for regenerative medicine of electrically conductive tissues[15,19,20,33–42].

With this work we develop an original method to form electroconductive biomaterials in form of hydrogels that can be injected into the lesion with a minimally invasive approach and with a controlled and tunable gelation timing. The hydrogels are based on gelatine and PEDOT conjugated with poly(styrene-sulfonate) (PEDOT:PSS) in order to enhance its solubility and stability in water. Reticulation is promoted by the natural crosslinker genipin, without the need of any gelatine chemical modification like methacrylation, and of UV-curing. Biocompatibility towards cell models and performance of this set of materials was evaluated, confirming the interesting role conductive hydrogels could play within electroconductive tissues regeneration, especially in neural regeneration (Fig. 4.1).
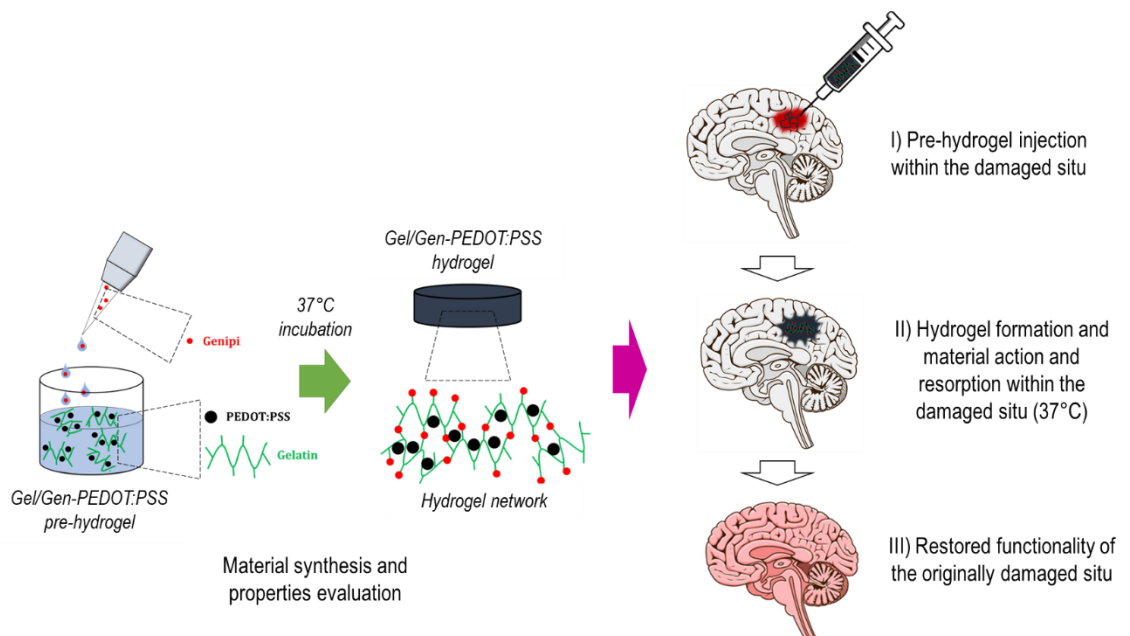

Fig. 4.1 Schematic stream process representation of the PEDOT:PSS injectable inks conceptualization and development.

4.2 Materials and methods

4.2.1 Materials

Food grade gelatine from pig skin, bloom 280, was purchased by Italgelatinee S.p.A. (Italy). Genipin was purchased from Wako Chemicals (U.S.A.). Poly(3,4-ethylenedioxythiophene)-poly(styrenesulfonate) (PEDOT:PSS), 1.1% in H_2O, neutral pH, high-conductivity grade, was purchased from Sigma Aldrich (U.S.A.). Sodium azide and Dulbecco's Phosphate Buffered Saline Modified (DPBS), without calcium chloride and magnesium chloride, liquid, sterile-filtered, suitable for cell culture were purchased from Sigma Aldrich (U.S.A.). All reagents and chemicals were of high purity grade.

4.2.2 Preparation of gelatine and gelatine-PEDOT:PSS hydrogels

The gelatine-based hydrogel was prepared by mixing gelatine powder with deionized water, heating up to 45°C under magnetic stirring to solubilize it, then genipin solution of 10 mg/mL prepared deionized water by sonicating for 30 minutes prior its use was added to the mixture and finally 10 mL of the resulting solution were transferred in a petri dish ($\varnothing$ = 60 mm) and incubated at 37°C for 24 hours (Fig. 4.2). To the aim of finding a sample able to gel in physiological conditions, different compositions were investigated, in particular with gelatine ranging from 5 to 10% (w/w respect to the total weight of the sample) and genipin from 0.02 to 1% (w/w respect to gelatine).

For the electroconductive hydrogels, PEDOT:PSS solution was added to gelatine solution, in concentration ranging from 0 to 0.3% (w/w respect to the total weight of the sample), prior to genipin addition. The amount of water was adjusted in order to fabricate hydrogels with the same concentration (w/w) of gelatine. The final composition of hydrogels resulted to be: gelatine 10% (w/w respect to the total weight of the sample), genipin 1% (w/w respect to gelatine) and PEDOT:PSS equal to 0, 0.1 and 0.3% (w/w respect to the total weight of the sample).

4.2.3 Rheological characterization

Rheological measurements were performed using a Bohlin C-VOR 120 rotational rheometer equipped with a thermostatic unit (KTB 30). Rheological tests were performed in oscillatory shear conditions on crosslinked hydrogels (after incubation for 24 hours at 37°C). After samples preparation (according to Paragraph 2.2), the resulting hydrogel (thickness = 2.7 mm) was then punched with a 20 mm diameter punch prior to be transferred on the rheometer plate.

Gelation kinetics was evaluated by cone/plate CP4/40 (conicity 4°, $\varnothing = 40$ mm) stainless steel plates and a gap of 0,150 mm. Time sweep experiments were performed in strain-controlled conditions, with deformation, γ, of 0.01, kept constant throughout the experiment, frequency (ν) of 3 and 5 Hz and time of 6 hours. Upon addition of genipin, samples were mixed under stirring for about 10 s to uniform samples and poured on the plate. The values of storage G' (elastic response) and loss G'' (viscous response) moduli were recorded as a function of time. Time sweep experiments were performed at 37°C.

In all cases, except for stress sweep tests, silicone oil (viscosity 50 cSt, purchased from Sigma, USA) was used to seal the interface between the two plates to improve thermal control and limit solvent evaporation.

4.2.4 Dynamic Mechanical Analysis

Dynamic mechanical analysis (DMA) was performed on crosslinked hydrogels. After samples preparation (according to Paragraph 2.2), the resulting hydrogel (thickness = 5.2 mm) was then punched with a 15 mm diameter punch prior to be transferred on the DMA plate. Stress-strain curves were collected by using Dynamic Mechanical Analyzer DMA Q800 (TA instruments, Italy) in compressive mode. Tests were performed at 37°C and in vapor saturated environment to prevent solvent evaporation.

4.2.5 Electrochemical Impedance Spectroscopy

Electrochemical impedance spectroscopy (EIS) measurements were performed on crosslinked hydrogels. After samples preparation (according to Paragraph 2.2), the resulting hydrogel (thickness = 1.2 mm) was punched with a 6 mm diameter punch prior to be transferred between two gold flaps of a symmetrical electrochemical cell. The electrochemical cell was manufactured by fixing two gold flaps to a plastic bar by exploiting an insulating adhesive tape (Fig 4.4).

EIS measurements were performed with an AUTOLAB PGSTAT302N-FRA32M electrochemical workstation (Metrohm, the Netherlands) controlled by Nova 2.1 software. EIS measurements were performed in the frequency range between 10^5 and 10^{-2} Hz, with signal amplitude of 10 mV, with an applied potential equal to 0 V and at room temperature. The obtained Nyquist plots were fitted using Z-View software (Scribner Associates).

This experimental setup was used both for the as-prepared hydrogels (0, 0.1 and 0.3 % w/w PEDOT:PSS) and for hydrogels fabricated by using PEDOT:PSS sterilized by exploiting different techniques, namely *i*) autoclaving and *ii*) gamma radiation at 25 kGy of both liquid and freeze-dried (and subsequently re-hydrated with the same amount of water before hydrogel synthesis) PEDOT/PSS.

The same set of experiments were also performed on hydrogels fabricated by using Phosphate Buffered Saline as solvent.

4.2.6 Swelling and degradation tests

Swelling and degradation tests were performed on crosslinked hydrogels. After samples preparation (according to Paragraph 2.2), the resulting hydrogel was then punched with a 6 mm diameter punch. Resulting hydrogels (thickness = 2.4 mm) were transferred into wells of a 24-well plate containing 2 mL of DPBS supplemented with 0.1 % w/V of sodium azide, to avoid mold and bacteria contamination. The resulting multi-well plate was then placed at T = 37 °C under shaking. At selected time points – specifically 1, 3, 7, 14 and 21 days – hydrogels were removed from wells and weighed to evaluate hydrogels swelling. Data are reported as % of mass gained with respect to the initial weight of three samples (± standard deviation, SD), calculated as:

$$S = \left(\frac{W_t}{W_0} - 1\right) \times 100$$

where W_0 is the hydrogels weight at time 0, whereas W_t is the weight of the same at a selected time.

At the above-mentioned selected time points hydrogels were also freeze-dried and weighted to investigate hydrogels degradation. Data are reported as % of mass lost with respect to the initial weight of three samples (± standard deviation, SD), calculated as:

$$D = \left(1 - \frac{W_t}{W_0}\right) \times 100$$

where W_0 is the scaffolds weight at time 0, whereas W_t is the weight of the same at a selected time.

4.2.7 Sample processing, primary rat neocortical astrocytes culturing and viability testing

All single hydrogels components, *i.e.* gelatine powder, genipin powder and freeze-dried PEDOT/PSS, were sterilized by gamma radiation at 25 kGy. Samples were prepared according to Paragraph 2.2 in sterile conditions. In this case, after mixing the components 1 mL of the mixture was casted in order to cover the area of each 24 wells (diameter = 20 mm, Thermo Fisher multiwell). Electroconductive hydrogels were fabricated with PEDOT:PSS final concentration equal to 0.3% w/w respect to the total weight of the sample. Once casted, sample were maintained in a thermostable and humified cell incubator at 37 °C for 24 hours. Subsequently, hydrogels were overnight conditioned with 1.5 ml of PBS for each well before cell plating.

Primary rat neocortical astrocytes were prepared at the FABIT Department of the University of Bologna, in concordance with the Italian and European law of protection of laboratory animals and the approval of the local bioethical committee (ethical Italian protocol number ID 1338/2020 PR, released in February, valid for 5 years) as previously reported[43]. Cells were maintained up to three weeks in culture with Dulbecco's Modified Eagle Medium (DMEM, Sigma Aldrich, U.S.A.) supplemented with 15% of foetal bovine serum (FBS, Life Technologies, U.S.A.). At confluency they

were dispersed using trypsin-EDTA 0.25% (Life Technologies, U.S.A.) and the cell suspension was plated on hydrogels at a concentration of 8×10^3 cells per sample and maintained in culture medium containing 10% FBS.

Astrocytes viability and biocompatibility of hydrogels were analyzed via Alamar Blue (AB) assay according to the Interchim technical sheet (66941P) and to previously reported protocols[44]. Time course of astrocytic viability on substrates was evaluated from 2 days *in vitro* (DIV) to 18 DIV after re-plating cells on the substrates. Analyses of the AB fluorescence and correlation with viability was performed as previously described[45]. Data were collected from three separate experiments performed in triplicate and are expressed as mean ± Standard Error S.E. of the percentage of reduced AB. Statistical analysis and graph elaboration were performed using GraphPad Prism 9.0.0 (GraphPad Software, San Diego, CA). Unpaired Student's *t* test was performed to evaluate differences between two groups. Differences were considered significant for *p*-values less than 0.05.

4.3. Results and discussion

4.3.1 Genipin-assisted gelation of gelatine and gelatine-PEDOT:PSS

In order to promote gelatine gelation in a suitable time at physiological temperature, genipin was exploited as crosslinking agent. Genipin is a naturally occurring crosslinking agent able to bind primary amine groups of a large variety of biomolecules and which behaves in temperature and time dependent manner, as previously reported for other polymers[46–50]. Genipin was mixed with a gelatine solution, forming a colorless liquid mixture. Upon incubation at the physiological temperature of 37°C, for 24 hours, genipin promoted the formation of a dark blue hydrogel (Fig. 4.2 A and B). The addition of PEDOT:PSS to the mixture did not impair the crosslinking process, allowing instead the interaction between the conductive polymer and the guanidinium groups of gelatine backbone, providing the formation of a homogeneous black liquid mixture[51]. The conductive polymer was embedded within gelatine network and the final hydrogel displayed a black/dark blue color (Fig. 4.2 A and B). Comparable black hydrogels based on UV-crosslinked methacryloyl gelatine and PEDOT:PSS were previously reported[19,20], nevertheless, UV-crosslinking usually display low biocompatibility. Conversely, the approach developed within this work is suitable to devise injectable hydrogels avoiding additional steps of gelatine methcrylation and UV-curing.
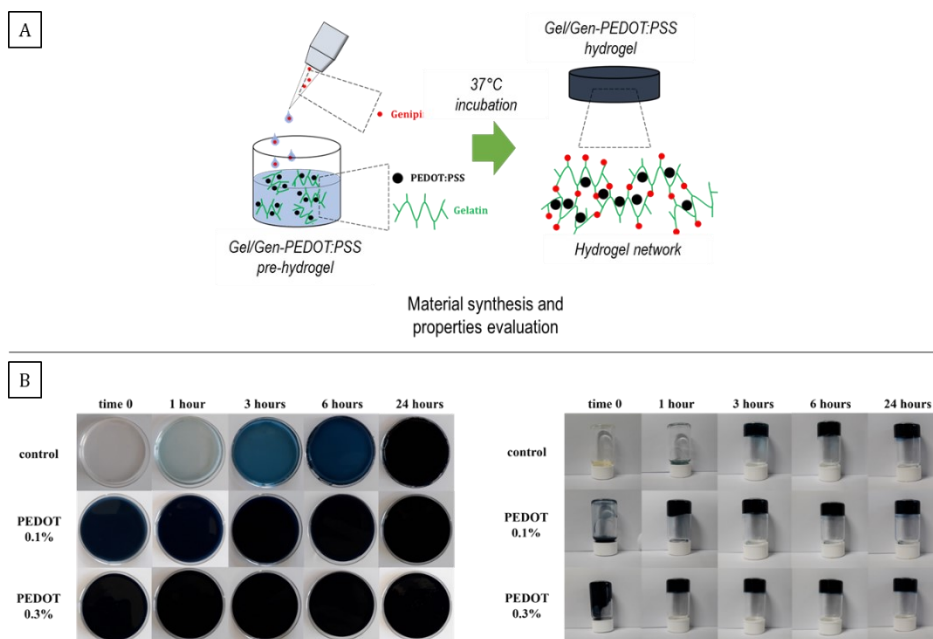
Fig. 4.2 Schematic representation of gelatine-based PEDOT:PSS hydrogels synthesis (A) visual analyses of gelatine-based matrices at different timeframes, starting from immediately after genipin addition (time 0) and after 1, 3, 6 and 24 hours. On the right the upside-down test for a visual evaluation of the gelation time.

The gelation process was investigated by rheological tests. More in detail, the loss tangent $(tan\delta = \frac{G''}{G'})$ was recorded as a function of time at different frequencies (Fig. 4.3). The progressive decay of loss tangents suggested the transition from a viscous solution towards a hydrogel upon time. Gelation times were calculated as the intersection of loss tangents at different frequencies[52–54].
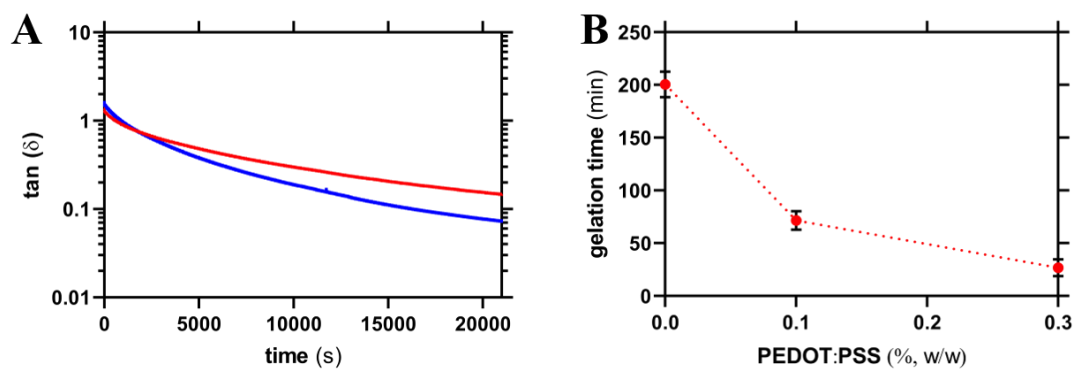

Fig. 4.3 Time oscillatory sweep tests by rheology. (A) Dependence of the loss tangents, tan (δ) on time at two different frequencies, *i.e.* 5 Hz (red dots) and 3 Hz (blue dots), for the sample in the presence of PEDOT:PSS 0.3% (w/w). (B) Dependence of the gelation time on the concentration of PEDOT:PSS (%, w/w).

For the control sample the gelation time was equal to 3 hours and 20 minutes $\pm$ 15 minutes (Fig. 4.3 B). In presence of PEDOT:PSS a marked gelation time reduction was detected. Specifically, in presence of a limited amount of PEDOT:PSS, *i.e.* with PEDOT:PSS 0.1%, gelation time was close to 1 hour. By further increasing PEDOT:PSS concentration from 0.1% w/w to 0.3% w/w, gelation time further decreased to 27 $\pm$ 8 minutes. This behavior can be attributed to the ability of conductive polymer to behave as nucleation site for the network assembly. Thus, the presence of a conductive polymer greatly enhanced gelatine network gelation. The final results of the process were homogenous hydrogels based on gelatine embedding PEDOT:PSS. Similar findings, such as a reduction in the gelation time in presence of colloids, were previously reported for fibrin hydrogels embedding magnetic nanoparticles[55] and sstems with similar gelation times, *i.e.* within 60 minutes at physiological temperature, resulted to be appropriate for regenerative medicine purposes[56–58].

4.3.2 Mechanical performance of hydrogels

In order to study the role played by PEDOT:PSS in modulating the mechanical properties of networks Dynamic Mechanical Analysis (DMA) tests were performed on systems with different amounts of conductive polymer.

Stress-strain tests were then performed by Dynamic Mechanical Analysis (DMA). In Fig. 4.4 are reported compression stress values as function of the applied strain. Young moduli (E) were determined as the angular coefficient of the stress-strain response from 0 to 10% strain. Control hydrogels displayed a Young's modulus (E) equal to 11.3 $\pm$ 1.5 kPa. A similar Young's modulus was previously reported by Annabi and collaborators for hydrogels based on UV-crosslinked methacryloyl gelatine suitable for myoblasts encapsulation[20].

The addition of PEDOT:PSS improved the stiffness of resulting hydrogels. More in detail, by using a concentration of PEDOT:PSS equal to 0.3% w/w, Young's modulus was increased up to 17.7 $\pm$ 1.7 kPa. Specifically, Young's modulus resulted to be proportional to the amount of PEDOT:PSS (Fig. 4.4 B). An inverse trend, meaning a decrease in the Young's modulus as function of PEDOT:PSS amount, was previously reported by Annabi and co-workers and by Zhang and collaborators for hydrogels

based on UV-crosslinked methacryloyl gelatine and the same amounts of PEDOT:PSS[19,20,40]. They attributed these finding to the lower ability of UV light penetration through the gelatine network in the presence of the conductive polymer, entailing the lower crosslinks of the resulting hydrogels. Our approach, on the contrary, not being based on any light-dependent crosslinking reaction, passible of impairment by the increased amount of conductive polymer potentially shielding the light, wasn't affected by this problem.

Similar Young's moduli were previously reported for other electroconductive materials devised for neural tissue engineering and as sensors/actuators[33,59,60]. Indeed, Young's modulus of all fabricated hydrogels was proven to be in the range of the native nervous tissue (E ~ 0.1-20 kPa)[61]. Furthermore, materials with similar ranges of Young's moduli were reported to promote differentiation of mesenchymal stem cells towards neural and muscular lineage[62,63]. Taking into account these pivotal reports, the hydrogels herein reported can be considered as biomimetics of the central nervous system mechanics.
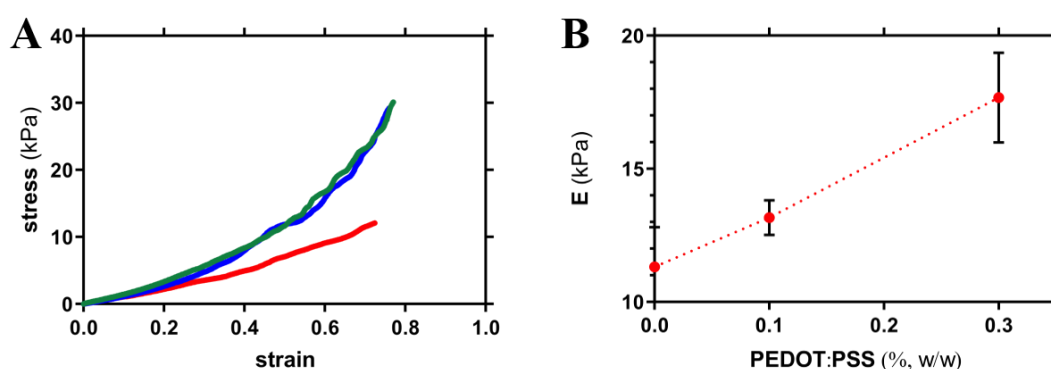

Figure 4.4 Mechanical characterization by Dynamic Mechanical Analysis (DMA). (A) Dependence of compression stress on applied strain for gelatine-based hydrogels with different amounts of PEDOT:PSS: [PEDOT:PSS] = 0% (w/w) (red), [PEDOT:PSS] = 0.1% (w/w) (blue), and [PEDOT:PSS] = 0.3% (w/w) (green). (B) Dependence of the Young modulus, *E*, on the amount of PEDOT:PSS. Data are reported as means ± standard deviations (SD) of six measurements. The dotted line is drawn to guide the eye.

4.3.3 Electroconductive properties of hydrogels

In order to study the role played by PEDOT:PSS in modulating the electroconductive properties of networks, electrochemical impedance spectroscopy (EIS) tests were performed on hydrogels with three different PEDOT:PSS concentrations, namely 0,

0.1 and 0.3 % w/w by an home-made designed electrochemical cell made of two gold flaps anchored onto an insulating support by means of insulating tape (Fig. 4.5, A and B).
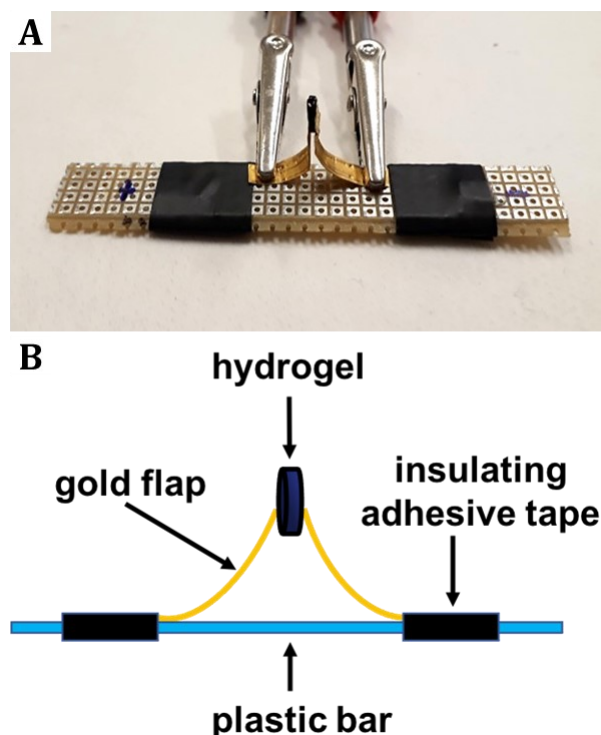

Fig. 4.5 Experimental set-up used for Electrochemical Impedance Spectroscopy (EIS) analyses (A). The electroconductive hydrogel sample was tested between the gold electrodes. (B) Schematic representation of experimental set-up used for Electrochemical Impedance Spectroscopy analyses.

In Fig. 4.6 A and D are reported the Bode plots of hydrogels with different amounts of PEDOT:PSS, prepared using deionized water (Fig. 4.6, A-C) and phosphate-buffered saline (PBS) as solvent (Fig. 4.6, D-F). This because hydrogels are mainly made of water (~ 90%), which, as deionized water, behaves as good insulant medium (0.055 μS/cm, 25 °C) and if any additional ions were introduced during hydrogels fabrication the ion transport within hydrogels might have been partially impaired.–Moreover, cells live in an ions-rich environment in which the ionic conductivity is not prevented[64]. PBS was selected since it can mimic physiological pH and osmolarity.

The corresponding EIS spectra were plotted also according to Nyquist plot (Fig. 4.6 B and E with magnification in the high frequencies region). In order to calculate the hydrogels conductivity, Nyquist plots were fitted using the equivalent circuit reported in Fig.4.5 B and E where R1 describe the overall electrical conductivity, R2

and CPE1 describe respectively the resistance and the charge accumulation capacitance of the interface between the hydrogel pellet and the metal electrodes, and finally WS-1 describe the Warburg impedance related to ions diffusion. According to this approach, it was possible to distinguish between the electronic and ionic properties of electroconductive materials[65]. Hydrogels electronic conductivity (σ) was determined according to equation:

$$\sigma = \frac{h}{A \times R_1}$$

where A is the hydrogel area (0.283 cm^2), h is the distance between the two electrodes (0.12 cm) and R_1 is the bulk resistance at the highest frequency obtained from EIS.

A similar trend in the conductivity was detected for both the hydrogels typology (Figure 4.5 C, F). The overall conductivity resulted to be increased by the PBS presence of almost one order of magnitude, but what was interesting to see was that, also in the present of physiologically relevant ions, the electronic conductivity of hydrogels resulted to be proportional to the amount of PEDOT:PSS, with higher amount of PEDOT:PSS correlating with great enhancement of the electronic conductivity.

A similar trend of impedance values as function of PEDOT:PSS amount was previously reported by Annabi and co-workers for hydrogels based on methacrylate gelatine[19,20]. For the highest PEDOT:PSS amount, similar conductivity values were reported by Magistris and collaborators for poly(ethylene oxide)-based polymer electrolytes[66].
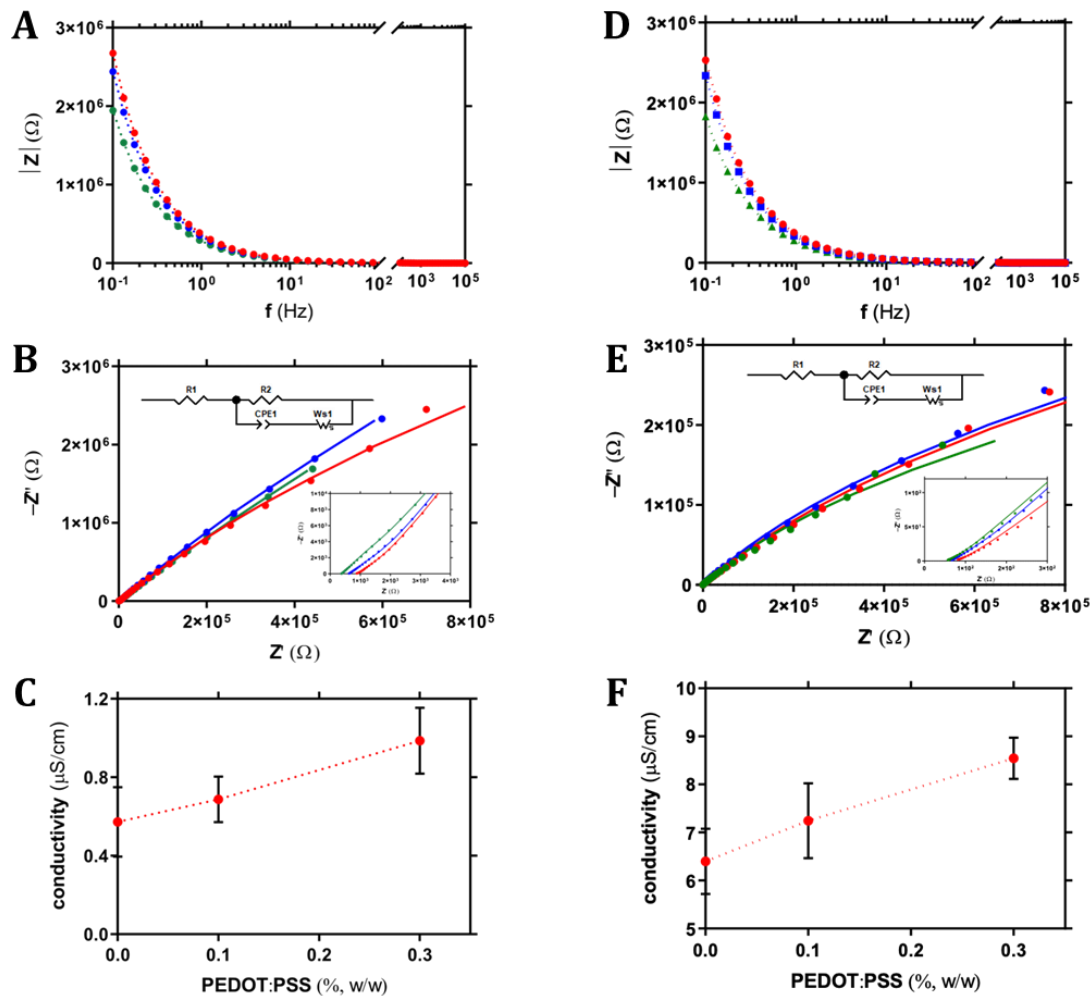
Figure 4.6 Electrochemical Impedance Spectroscopy measurements of gelatine-based hydrogels prepared in deionized water (A-C) and in PBS (D-F). (A, D) Electrochemical Impedance Spectroscopy measurements of gelatine-based hydrogels with different amounts of PEDOT: [PEDOT:PSS] = 0% (w/w) (red), [PEDOT:PSS] = 0.1% (w/w) (blue), and [PEDOT:PSS] = 0.3% (w/w) (green). (B, E) Corresponding Nyquist plot for gelatine-based hydrogels with different amounts of PEDOT. Colored solid lines are the best fit of experimental points. (C, F) Dependence of the electronic conductivity on the amount of PEDOT. Data are reported as means ± standard deviations (SD) of seven measurements. All dotted lines are drawn to guide the eye.

The ionic conductivity was similar in all samples (observed at medium-low frequencies of Nyquist plots in Fig 4.5 B and E).

Hydrogels were fabricated also by using PEDOT:PSS sterilized by means of different techniques. This step was necessary in order to find the best sterilization technique to prepare the hydrogels for biological applications. Gamma radiation treatment on liquid and freeze-dried PEDOT:PSS was proven to not significantly affect the electroconductivity of resulting hydrogels contrary to autoclaving (Fig. 4.7). A similar decrease in conductivity of electrophysiology devices based on PEDOT:PSS

upon autoclaving was previously reported by Malliaras and co-workers.[67]
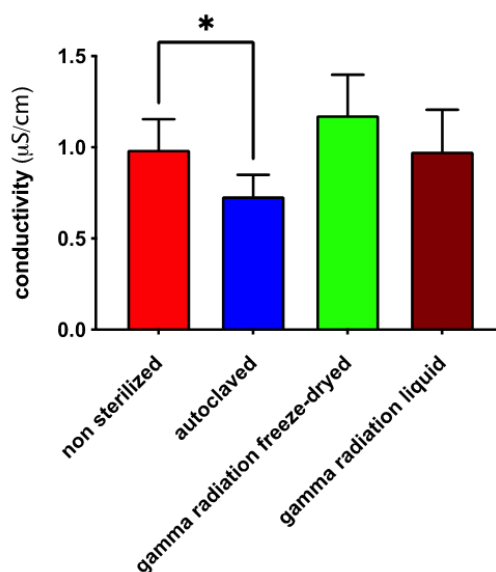
Figure 4.7 Dependence of conductivity on different sterilization techniques for PEDOT:PSS. The evaluation was performed on PEDOT:PSS concentration of 0.3% w/w respect to the total weight of the sample. One-way ANOVA followed by Dunnett post-hoc test was performed to compare all groups (*: p value < 0.05). In all cases, data are reported as means ± standard deviations (SD) of five measurements.

4.3.4 Hydrogels stability

In order to study the role played by PEDOT:PSS in modulating the stability of networks, swelling and degradation tests were performed on hydrogels with different amounts of the conductive polymer.

After 24 hours in PBS, control hydrogels were able to uptake a large amount of solvent, showing a weight increase of about 70% (Fig. 4.8).

Fig. 4.8 Dependence of swelling, i.e. PBS uptake, on time of gelatine-based hydrogels with different amounts of PEDOT:PSS: [PEDOT:PSS] = 0% (w/w) (red), [PEDOT:PSS] = 0.1% (w/w) (blue), and [PEDO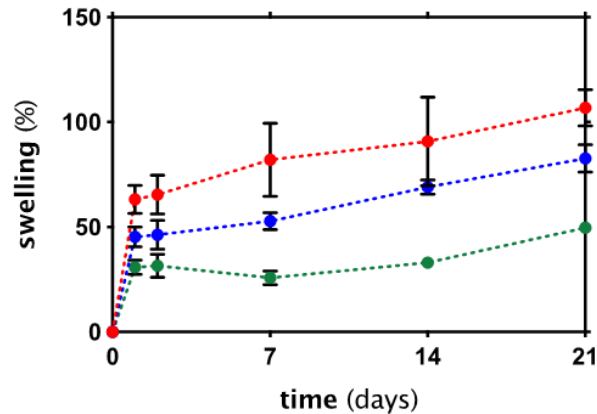T:PSS] = 0.3% (w/w) (green). Experimental conditions: [gelatine] = 10% (w/w respect to the total weight of the sample), [genipin] = 1% (w/w respect to gelatine), and [PEDOT:PSS] = 0 - 0.3% (w/w respect to the total weight of the sample), T = 37 °C. In all cases, data are reported as means ± standard deviations (SD) of three measurements.

At later timeframes, up to 21 days, their solvent uptake slightly increased up to almost doubling their weight, with an increase of almost 100%.

Hydrogels embedding PEDOT:PSS displayed a reduced swelling ability, proportional to the conductive polymer concentration (Fig. 4.8). Specifically, for hydrogels with a concentration of PEDOT:PSS equal to 0.3% w/w the swelling of resulting hydrogels after 21 days was equal to about 50%. This behavior can be attributed to the partial hindrance of networks deformation due to the conductive polymer presence, as previously discussed in the mechanics section.

Consequently, networks embedding conductive polymer displayed a lower solvent uptake ability, even if still in a suitable range for appropriate cell colonization and growth[20].

All the realized hydrogels, with and without PEDOT:PSS, displayed a degradation inferior to 10% in PBS (data not shown). Thus, all hydrogels displayed a good stability after 21 days in physiological conditions of pH and osmolarity.

4.3.5 Effects of PEDOT:PSS hydrogels on the viability of primary astrocytes

Given the importance of conductive materials in neuro-regenerative medicine targeting brain repair, we next sought to investigate the effect of electroconductive hydrogels on primary astrocytes. It has been recently highlighted that the interaction

of implantable materials and device with astrocytes is critical for the long-term stability and to determine the successful outcome of brain implantation[68].

In this respect, to determine the impact of hydrogels on astrocytes viability, confluent primary rat cortical astrocytes were re-plated on electroconductive PEDOT:PSS hydrogels. Given the well-known biocompatibility of gelatine and genipin[69,70], hydrogels without electroconductive polymer were used as control.
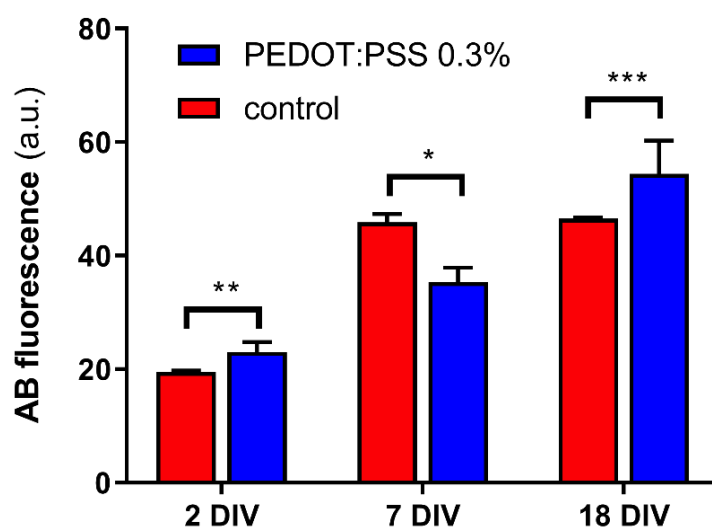

Fig. 4.9 Time course of astrocytes viability on electroconductive and control hydrogels obtained by Alamar Blue (AB) assay performed after 2, 7 and 18 days *in vitro* (DIV) from cells seeding on the substrates. Experimental conditions: [gelatine] = 10% (w/w respect to the total weight of the sample), [genipin] = 1% (w/w respect to gelatine), and [PEDOT:PSS] = 0 or 0.3% (w/w respect to the total weight of the sample). Data are plotted as the averaged percentages of reduced AB ± Standard Error (SE). Unpaired Student's *t* test was performed to compare samples (*: *p* value < 0.05; **: *p* value < 0.01; ***: *p* value < 0.001).

The bar plot shown in Fig. 4.9 reports the averaged percentage of reduced AB, with respect to the oxidize one observed in different conditions tested at different time points equal to 2, 7 and 18 DIV (days *in vitro*) after replating. The values reported are proportional to the metabolic activity of the cells and, on turn, correlate with the presence of viable cells in the substrate[71].

Notably, the results demonstrate that, at 2 DIV, the viability was significantly higher on electroconductive samples than on control. In particular, electroconductive samples promote the highest adhesion of astrocytes after 2 DIV. Nonetheless, the cell viability increase over time up to 7 DIV in control hydrogels and up to 18 days in PEDOT:PSS-based hydrogels. These data are in line with other *in vitro* and *in vivo*

studies showing good biocompatibility of PEDOT:PSS film and bidimensional substrates with other cell types, including brain cells[72]. We found that the adhesion as well as the long-term viability are ameliorated in the electroconductive hydrogels, obtained using the conductive polymer PEDOT:PSS. It is remarkable that, while the growth of astrocytes on control samples reaches a plateau after 7 DIV, astrocytes continue to grow in electroconductive hydrogels. These results suggest that the presence of electroconductive polymer enhance a sustained cell growth and colonization.

Collectively, the analyses revealed that these electroconductive hydrogels display a very good biocompatibility with primary astrocytes and thus might be a suitable candidate as neural interface or for neural tissue engineering.

4.4 Conclusions

Within this work, we developed an original method to fabricate electroconductive hydrogels based on gelatine, a biologically derived polymer, and PEDOT:PSS, a biocompatible conductive polymer. Genipin, in synergy with PEDOT:PSS, was able to promote a homogenous reticulation of the resulting composite networks. Physical-chemical properties, including mechanical performance, electroconductive properties, swelling and degradation of resulting hydrogels were proven to be consistent with the native neural tissue features as well as finely tunable through the amount of conductive polymer added. Moreover, all the hydrogels resulted to be biocompatible with primary rat astrocytes, an essential condition for materials intended as neural probes or for neuro-regenerative medicine.

This hydrogel system can be proposed as electrically conductive interfaces with human tissues, *e.g.* as neural probes and skin electrodes. Resulting hydrogels can be also proposed as biomaterials in the field of tissue engineering, being potentially *in-vivo* injectable and *in-situ* cross-likable thanks to its unique properties, especially for regeneration of electrically conductive tissues, *e.g.* muscular and neural tissues. Finally, this system is undoubtedly promising for development of 3D bio-printed electroconductive biomaterials for regenerative medicine.

References

(1)   Tibbitt, M. W.; Anseth, K. S. Hydrogels as Extracellular Matrix Mimics for 3D Cell Culture. *Biotechnol. Bioeng.* **2009**, *103* (4), 655–663. https://doi.org/10.1002/bit.22361.

(2)   Zhang, Y. S.; Khademhosseini, A. Advances in Engineering Hydrogels. *Science (80-.).* **2017**, *356* (6337). https://doi.org/10.1126/science.aaf3627.

(3)   Li, Y.; Rodrigues, J.; Tomás, H. Injectable and Biodegradable Hydrogels: Gelation, Biodegradation and Biomedical Applications. *Chem. Soc. Rev.* **2012**, *41* (6), 2193–2221. https://doi.org/10.1039/c1cs15203c.

(4)   Jiang, Y.; Chen, J.; Deng, C.; Suuronen, E. J.; Zhong, Z. Click Hydrogels, Microgels and Nanogels: Emerging Platforms for Drug Delivery and Tissue Engineering. *Biomaterials* **2014**, *35* (18), 4969–4985. https://doi.org/10.1016/j.biomaterials.2014.03.001.

(5)   Kim, T. G.; Shin, H.; Lim, D. W. Biomimetic Scaffolds for Tissue Engineering. *Adv. Funct. Mater.* **2012**, *22* (12), 2446–2468. https://doi.org/10.1002/adfm.201103083.

(6)   Webber, M. J.; Appel, E. A.; Meijer, E. W.; Langer, R. Supramolecular Biomaterials. *Nat. Mater.* **2015**, *15* (1), 13–26. https://doi.org/10.1038/nmat4474.

(7)   Holzapfel, B. M.; Reichert, J. C.; Schantz, J. T.; Gbureck, U.; Rackwitz, L.; Nöth, U.; Jakob, F.; Rudert, M.; Groll, J.; Hutmacher, D. W. How Smart Do Biomaterials Need to Be? A Translational Science and Clinical Point of View. *Adv. Drug Deliv. Rev.* **2013**, *65* (4), 581–603. https://doi.org/10.1016/j.addr.2012.07.009.

(8)   Marti, M. E.; Sharma, A. D.; Sakaguchi, D. S.; Mallapragada, S. K. *Nanomaterials for Neural Tissue Engineering*; Woodhead Publishing Limited, 2013. https://doi.org/10.1533/9780857097231.2.275.

(9)   Eyre, D. Collagen of Articular Cartilage. *Arthritis Res.* **2002**, *4* (1), 30–35. https://doi.org/10.1186/ar380.

(10)   He, Q.; Huang, Y.; Wang, S. Hofmeister Effect-Assisted One Step Fabrication of

Ductile and Strong Gelatine Hydrogels. *Adv. Funct. Mater.* **2018**, *28* (5), 1–10. https://doi.org/10.1002/adfm.201705069.

(11)   Baumann, M. D.; Stanwick, J. C.; Donaghue, I. E.; Shoichet, M. S. *Biomaterials for Spinal Cord Repair*; Elsevier Ltd., 2011; Vol. 6. https://doi.org/10.1016/b978-0-08-055294-1.00238-5.

(12)   Li, X.; Xiao, Z.; Han, J.; Chen, L.; Xiao, H.; Ma, F.; Hou, X.; Li, X.; Sun, J.; Ding, W.; Zhao, Y.; Chen, B.; Dai, J. Promotion of Neuronal Differentiation of Neural Progenitor Cells by Using EGFR Antibody Functionalized Collagen Scaffolds for Spinal Cord Injury Repair. *Biomaterials* **2013**, *34* (21), 5107–5116. https://doi.org/10.1016/j.biomaterials.2013.03.062.

(13)   Amy CY Lo, F. S. Collagen-Based Scaffolds for Cell Therapies in the Injured Brain. *J. Stem Cell Res. Ther.* **2015**, *05* (02). https://doi.org/10.4172/2157-7633.1000267.

(14)   Sirivisoot, S.; Pareta, R.; Harrison, B. S. Protocol and Cell Responses in Threedimensional Conductive Collagen Gel Scaffolds with Conductive Polymer Nanofibres for Tissue Regeneration. *Interface Focus* **2014**, *4* (1). https://doi.org/10.1098/rsfs.2013.0050.

(15)   Distler, T.; Boccaccini, A. R. 3D Printing of Electrically Conductive Hydrogels for Tissue Engineering and Biosensors – A Review. *Acta Biomater.* **2020**, *101*, 1–13. https://doi.org/10.1016/j.actbio.2019.08.044.

(16)   Zhang, S.; Chen, Y.; Liu, H.; Wang, Z.; Ling, H.; Wang, C.; Ni, J.; Çelebi-Saltik, B.; Wang, X.; Meng, X.; Kim, H. J.; Baidya, A.; Ahadian, S.; Ashammakhi, N.; Dokmeci, M. R.; Travas-Sejdic, J.; Khademhosseini, A. Room-Temperature-Formed PEDOT:PSS Hydrogels Enable Injectable, Soft, and Healable Organic Bioelectronics. *Adv. Mater.* **2020**, *32* (1), 1–7. https://doi.org/10.1002/adma.201904752.

(17)   Aggas, J. R.; Abasi, S.; Phipps, J. F.; Podstawczyk, D. A.; Guiseppi-Elie, A. Microfabricated and 3-D Printed Electroconductive Hydrogels of PEDOT:PSS and Their Application in Bioelectronics. *Biosens. Bioelectron.* **2020**, *168* (August), 112568. https://doi.org/10.1016/j.bios.2020.112568.

(18) Usmani, S.; Biagioni, A. F.; Medelin, M.; Scaini, D.; Casani, R.; Aurand, E. R.; Padro, D.; Egimendia, A.; Cabrer, P. R.; Scarselli, M.; De Crescenzi, M.; Prato, M.; Ballerini, L. Functional Rewiring across Spinal Injuries via Biomimetic Nanofiber Scaffolds. *Proc. Natl. Acad. Sci. U. S. A.* **2020**, *117* (41), 25212–25218. https://doi.org/10.1073/pnas.2005708117.

(19) Spencer, A. R.; Shirzaei Sani, E.; Soucy, J. R.; Corbet, C. C.; Primbetova, A.; Koppes, R. A.; Annabi, N. Bioprinting of a Cell-Laden Conductive Hydrogel Composite. *ACS Appl. Mater. Interfaces* **2019**, *11* (34), 30518–30533. https://doi.org/10.1021/acsami.9b07353.

(20) Spencer, A. R.; Primbetova, A.; Koppes, A. N.; Koppes, R. A.; Fenniri, H.; Annabi, N. Electroconductive Gelatine Methacryloyl-PEDOT:PSS Composite Hydrogels: Design, Synthesis, and Properties. *ACS Biomater. Sci. Eng.* **2018**, *4* (5), 1558–1567. https://doi.org/10.1021/acsbiomaterials.8b00135.

(21) Kuzmenko, V.; Kalogeropoulos, T.; Thunberg, J.; Johannesson, S.; Hägg, D.; Enoksson, P.; Gatenholm, P. Enhanced Growth of Neural Networks on Conductive Cellulose-Derived Nanofibrous Scaffolds. *Mater. Sci. Eng. C* **2016**, *58*, 14–23. https://doi.org/10.1016/j.msec.2015.08.012.

(22) Bagher, Z.; Atoufi, Z.; Alizadeh, R.; Farhadi, M.; Zarrintaj, P.; Moroni, L.; Setayeshmehr, M.; Komeili, A.; Kamrava, S. K. Conductive Hydrogel Based on Chitosan-Aniline Pentamer/Gelatine/Agarose Significantly Promoted Motor Neuron-like Cells Differentiation of Human Olfactory Ecto-Mesenchymal Stem Cells. *Mater. Sci. Eng. C* **2019**, *101* (March), 243–253. https://doi.org/10.1016/j.msec.2019.03.068.

(23) Wang, S.; Guan, S.; Xu, J.; Li, W.; Ge, D.; Sun, C.; Liu, T.; Ma, X. Neural Stem Cell Proliferation and Differentiation in the Conductive PEDOT-HA/Cs/Gel Scaffold for Neural Tissue Engineering. *Biomater. Sci.* **2017**, *5* (10), 2024–2034. https://doi.org/10.1039/c7bm00633k.

(24) Wang, S.; Guan, S.; Li, W.; Ge, D.; Xu, J.; Sun, C.; Liu, T.; Ma, X. 3D Culture of Neural Stem Cells within Conductive PEDOT Layer-Assembled Chitosan/Gelatine Scaffolds for Neural Tissue Engineering. *Mater. Sci. Eng. C* **2018**, *93* (August), 890–901. https://doi.org/10.1016/j.msec.2018.08.054.

(25)   Tysseling, V. M.; Kessler, J. A. *Biomaterials for Central Nervous System Regeneration*; Elsevier Ltd., 2011; Vol. 5. https://doi.org/10.1016/b978-0-08-055294-1.00185-9.

(26)   Guo, J.; Yu, Y.; Wang, H.; Zhang, H.; Zhang, X.; Zhao, Y. Conductive Polymer Hydrogel Microfibers from Multiflow Microfluidics. *Small* **2019**, *15* (15), 1–7. https://doi.org/10.1002/smll.201805162.

(27)   Nezakati, T.; Seifalian, A.; Tan, A.; Seifalian, A. M. Conductive Polymers: Opportunities and Challenges in Biomedical Applications. *Chem. Rev.* **2018**, *118* (14), 6766–6843. https://doi.org/10.1021/acs.chemrev.6b00275.

(28)   Yano, H.; Kudo, K.; Marumo, K.; Okuzaki, H. Fully Soluble Self-Doped Poly(3,4-Ethylenedioxythiophene) with an Electrical Conductivity Greater than 1000 S Cm -1. *Sci. Adv.* **2019**, *5* (4), 1–10. https://doi.org/10.1126/sciadv.aav9492.

(29)   Yuk, H.; Lu, B.; Lin, S.; Qu, K.; Xu, J.; Luo, J.; Zhao, X. 3D Printing of Conducting Polymers. *Nat. Commun.* **2020**, *11* (1), 4–11. https://doi.org/10.1038/s41467-020-15316-7.

(30)   Teng, W.; Zhou, Q.; Wang, X.; Che, H.; Hu, P.; Li, H.; Wang, J. Hierarchically Interconnected Conducting Polymer Hybrid Fiber with High Specific Capacitance for Flexible Fiber-Shaped Supercapacitor. *Chem. Eng. J.* **2020**, *390* (December 2019), 124569. https://doi.org/10.1016/j.cej.2020.124569.

(31)   Jang, H.; Park, J.; Kim, F. S. Doped State and Solubility Changes in PEDOT:PSS Thin Films by High-Energy Gamma-Ray Irradiation. *Phys. Status Solidi Appl. Mater. Sci.* **2019**, *216* (9), 1–7. https://doi.org/10.1002/pssa.201800980.

(32)   Alegret, N.; Dominguez-Alfaro, A.; Salsamendi, M.; Gomez, I. J.; Calvo, J.; Mecerreyes, D.; Prato, M. Effect of the Fullerene in the Properties of Thin PEDOT/C60 Films Obtained by Co-Electrodeposition. *Inorganica Chim. Acta* **2017**, *468*, 239–244. https://doi.org/10.1016/j.ica.2017.04.059.

(33)   Wu, Y.; Chen, Y. X.; Yan, J.; Quinn, D.; Dong, P.; Sawyer, S. W.; Soman, P. Fabrication of Conductive Gelatine Methacrylate-Polyaniline Hydrogels. *Acta Biomater.* **2016**, *33*, 122–130. https://doi.org/10.1016/j.actbio.2016.01.036.

(34)   Lu, B.; Yuk, H.; Lin, S.; Jian, N.; Qu, K.; Xu, J.; Zhao, X. Pure PEDOT:PSS

Hydrogels. *Nat. Commun.* **2019**, *10* (1). https://doi.org/10.1038/s41467-019-09003-5.

(35)　Yang, B.; Yao, F.; Hao, T.; Fang, W.; Ye, L.; Zhang, Y.; Wang, Y.; Li, J.; Wang, C. Development of Electrically Conductive Double-Network Hydrogels via One-Step Facile Strategy for Cardiac Tissue Engineering. *Adv. Healthc. Mater.* **2016**, *5* (4), 474–488. https://doi.org/10.1002/adhm.201500520.

(36)　Alegret, N.; Dominguez-Alfaro, A.; González-Domínguez, J. M.; Arnaiz, B.; Cossío, U.; Bosi, S.; Vázquez, E.; Ramos-Cabrer, P.; Mecerreyes, D.; Prato, M. Three-Dimensional Conductive Scaffolds as Neural Prostheses Based on Carbon Nanotubes and Polypyrrole. *ACS Appl. Mater. Interfaces* **2018**, *10* (50), 43904–43914. https://doi.org/10.1021/acsami.8b16462.

(37)　Ferlauto, L.; D'Angelo, A. N.; Vagni, P.; Leccardi, M. J. I. A.; Mor, F. M.; Cuttaz, E. A.; Heuschkel, M. O.; Stoppini, L.; Ghezzi, D. Development and Characterization of PEDOT:PSS/Alginate Soft Microelectrodes for Application in Neuroprosthetics. *Front. Neurosci.* **2018**, *12* (SEP), 1–10. https://doi.org/10.3389/fnins.2018.00648.

(38)　Alegret, N.; Dominguez-Alfaro, A.; Mecerreyes, D. 3D Scaffolds Based on Conductive Polymers for Biomedical Applications. *Biomacromolecules* **2019**, *20* (1), 73–89. https://doi.org/10.1021/acs.biomac.8b01382.

(39)　Fomby, P.; Cherlin, A. J.; Hadjizadeh, A.; Doillon, C. J.; Sueblinvong, V.; Weiss, D. J.; Bates, J. H. T.; Gilbert, T.; Liles, W. C.; Lutzko, C.; Rajagopal, J.; Prockop, D. J.; Chambers, D.; Giangreco, A.; Keating, A.; Kotton, D.; Lelkes, P. I.; Wagner, D. E.; Prockop, D. J. Stem Cells and Cell Therapies in Lung Biology and Diseases: Conference Report. *Ann. Am. Thorac. Soc.* **2010**, *12* (3), 181–204. https://doi.org/10.1002/term.

(40)　Heo, D. N.; Lee, S. J.; Timsina, R.; Qiu, X.; Castro, N. J.; Zhang, L. G. Development of 3D Printable Conductive Hydrogel with Crystallized PEDOT:PSS for Neural Tissue Engineering. *Mater. Sci. Eng. C* **2019**, *99* (January), 582–590. https://doi.org/10.1016/j.msec.2019.02.008.

(41)　Kayser, L. V.; Lipomi, D. J. Stretchable Conductive Polymers and Composites Based on PEDOT and PEDOT:PSS. *Adv. Mater.* **2019**, *31* (10), 1–13.

https://doi.org/10.1002/adma.201806133.

(42)   Vishnoi, T.; Singh, A.; Teotia, A. K.; Kumar, A. Chitosan-Gelatine-Polypyrrole Cryogel Matrix for Stem Cell Differentiation into Neural Lineage and Sciatic Nerve Regeneration in Peripheral Nerve Injury Model. *ACS Biomater. Sci. Eng.* **2019**, *5*, 3007–3021. https://doi.org/10.1021/acsbiomaterials.9b00242.

(43)   Benfenati, V.; Caprini, M.; Nobile, M.; Rapisarda, C.; Ferroni, S. Guanosine Promotes the Up-Regulation of Inward Rectifier Potassium Current Mediated by Kir4.1 in Cultured Rat Cortical Astrocytes. *J. Neurochem.* **2006**, *98* (2), 430–445. https://doi.org/10.1111/j.1471-4159.2006.03877.x.

(44)   Durso, M.; Borrachero-Conejo, A. I.; Bettini, C.; Treossi, E.; Scidà, A.; Saracino, E.; Gazzano, M.; Christian, M.; Morandi, V.; Tuci, G.; Giambastiani, G.; Ottaviano, L.; Perrozzi, F.; Benfenati, V.; Melucci, M.; Palermo, V. Biomimetic Graphene for Enhanced Interaction with the External Membrane of Astrocytes. *J. Mater. Chem. B* **2018**, *6* (33), 5335–5342. https://doi.org/10.1039/c8tb01410h.

(45)   Saracino, E.; Maiolo, L.; Polese, D.; Semprini, M.; Borrachero-Conejo, A. I.; Gasparetto, J.; Murtagh, S.; Sola, M.; Tomasi, L.; Valle, F.; Pazzini, L.; Formaggio, F.; Chiappalone, M.; Hussain, S.; Caprini, M.; Muccini, M.; Ambrosio, L.; Fortunato, G.; Zamboni, R.; Convertino, A.; Benfenati, V. A Glial-Silicon Nanowire Electrode Junction Enabling Differentiation and Noninvasive Recording of Slow Oscillations from Primary Astrocytes. *Adv. Biosyst.* **2020**, *4* (4). https://doi.org/10.1002/adbi.201900264.

(46)   Bi, L.; Cao, Z.; Hu, Y.; Song, Y.; Yu, L.; Yang, B.; Mu, J.; Huang, Z.; Han, Y. Effects of Different Cross-Linking Conditions on the Properties of Genipin-Cross-Linked Chitosan/Collagen Scaffolds for Cartilage Tissue Engineering. *J. Mater. Sci. Mater. Med.* **2011**, *22* (1), 51–62. https://doi.org/10.1007/s10856-010-4177-3.

(47)   Barbosa, J. S.; Ribeiro, A.; Testera, A. M.; Alonso, M.; Arias, F. J.; Rodríguez-Cabello, J. C.; Mano, J. F. Development of Biomimetic Chitosan-Based Hydrogels Using an Elastin-like Polymer. *Adv. Eng. Mater.* **2010**, *12* (1–2), 37–44. https://doi.org/10.1002/adem.200980152.

(48)   Fessel, G.; Cadby, J.; Wunderli, S.; Van Weeren, R.; Snedeker, J. G. Dose- and

Time-Dependent Effects of Genipin Crosslinking on Cell Viability and Tissue Mechanics - Toward Clinical Application for Tendon Repair. *Acta Biomater.* **2014**, *10* (5), 1897–1906. https://doi.org/10.1016/j.actbio.2013.12.048.

(49)   Dimida, S.; Demitri, C.; De Benedictis, V. M.; Scalera, F.; Gervaso, F.; Sannino, A. Genipin-Cross-Linked Chitosan-Based Hydrogels: Reaction Kinetics and Structure-Related Characteristics. *J. Appl. Polym. Sci.* **2015**, *132* (28), 1–8. https://doi.org/10.1002/app.42256.

(50)   Sacco, P.; Furlani, F.; Marfoglia, A.; Cok, M.; Pizzolitto, C.; Marsich, E.; Donati, I. Temporary/Permanent Dual Cross-Link Gels Formed of a Bioactive Lactose-Modified Chitosan. *Macromol. Biosci.* **2020**, *20* (12), 1–7. https://doi.org/10.1002/mabi.202000236.

(51)   Burke, N. J.; Burrows, A. D.; Mahon, M. F.; Teat, S. J. Incorporation of Sulfonate Dyes into Hydrogen-Bonded Networks. *CrystEngComm* **2004**, *6* (71), 429–436. https://doi.org/10.1039/b406614f.

(52)   Ditta, L. A.; Bulone, D.; Biagio, P. L. S.; Marino, R.; Giacomazza, D.; Lapasin, R. The Degree of Compactness of the Incipient High Methoxyl Pectin Networks. A Rheological Insight at the Sol-Gel Transition. *Int. J. Biol. Macromol.* **2020**, *158*, 985–993. https://doi.org/10.1016/j.ijbiomac.2020.05.019.

(53)   Maleki, A.; Kjøniksen, A. L.; Nyström, B. Characterization of the Chemical Degradation of Hyaluronic Acid during Chemical Gelation in the Presence of Different Cross-Linker Agents. *Carbohydr. Res.* **2007**, *342* (18), 2776–2792. https://doi.org/10.1016/j.carres.2007.08.021.

(54)   Holly, E. E.; Venkataraman, S. K.; Chambon, F.; Henning Winter, H. Fourier Transform Mechanical Spectroscopy of Viscoelastic Materials with Transient Structure. *J. Nonnewton. Fluid Mech.* **1988**, *27* (1), 17–26. https://doi.org/10.1016/0377-0257(88)80002-8.

(55)   Bonhome-Espinosa, A. B.; Campos, F.; Rodriguez, I. A.; Carriel, V.; Marins, J. A.; Zubarev, A.; Duran, J. D. G.; Lopez-Lopez, M. T. Effect of Particle Concentration on the Microstructural and Macromechanical Properties of Biocompatible Magnetic Hydrogels. *Soft Matter* **2017**, *13* (16), 2928–2941. https://doi.org/10.1039/c7sm00388a.

(56) Supper, S.; Anton, N.; Seidel, N.; Riemenschnitter, M.; Curdy, C.; Vandamme, T. Thermosensitive Chitosan/Glycerophosphate-Based Hydrogel and Its Derivatives in Pharmaceutical and Biomedical Applications. *Expert Opin. Drug Deliv.* **2014**, *11* (2), 249–267. https://doi.org/10.1517/17425247.2014.867326.

(57) Park, K. M.; Lee, S. Y.; Joung, Y. K.; Na, J. S.; Lee, M. C.; Park, K. D. Thermosensitive Chitosan-Pluronic Hydrogel as an Injectable Cell Delivery Carrier for Cartilage Regeneration. *Acta Biomater.* **2009**, *5* (6), 1956–1965. https://doi.org/10.1016/j.actbio.2009.01.040.

(58) Tseng, T. C.; Tao, L.; Hsieh, F. Y.; Wei, Y.; Chiu, I. M.; Hsu, S. H. An Injectable, Self-Healing Hydrogel to Repair the Central Nervous System. *Adv. Mater.* **2015**, *27* (23), 3518–3524. https://doi.org/10.1002/adma.201500762.

(59) Odent, J.; Wallin, T. J.; Pan, W.; Kruemplestaedter, K.; Shepherd, R. F.; Giannelis, E. P. Highly Elastic, Transparent, and Conductive 3D-Printed Ionic Composite Hydrogels. *Adv. Funct. Mater.* **2017**, *27* (33), 1–10. https://doi.org/10.1002/adfm.201701807.

(60) Zhang, B.; Li, S.; Hingorani, H.; Serjouei, A.; Larush, L.; Pawar, A. A.; Goh, W. H.; Sakhaei, A. H.; Hashimoto, M.; Kowsari, K.; Magdassi, S.; Ge, Q. Highly Stretchable Hydrogels for UV Curing Based High-Resolution Multimaterial 3D Printing. *J. Mater. Chem. B* **2018**, *6* (20), 3246–3253. https://doi.org/10.1039/c8tb00673c.

(61) Tyler, W. J. The Mechanobiology of Brain Function. *Nat. Rev. Neurosci.* **2012**, *13* (12), 867–878. https://doi.org/10.1038/nrn3383.

(62) Engler, A. J.; Sen, S.; Sweeney, H. L.; Discher, D. E. Matrix Elasticity Directs Stem Cell Lineage Specification. *Cell* **2006**, *126* (4), 677–689. https://doi.org/10.1016/j.cell.2006.06.044.

(63) Murphy, W. L.; McDevitt, T. C.; Engler, A. J. Materials as Stem Cell Regulators. *Nat. Mater.* **2014**, *13* (6), 547–557. https://doi.org/10.1038/nmat3937.

(64) Zhao, S.; Tseng, P.; Grasman, J.; Wang, Y.; Li, W.; Napier, B.; Yavuz, B.; Chen, Y.; Howell, L.; Rincon, J.; Omenetto, F. G.; Kaplan, D. L. Programmable Hydrogel

Ionic Circuits for Biologically Matched Electronic Interfaces. *Adv. Mater.* **2018**, *30* (25). https://doi.org/10.1002/adma.201800598.

(65) Lee, S.; Randall, C. A. Determination of Electronic and Ionic Conductivity in Mixed Ionic Conductors: HiTEC and in-Situ Impedance Spectroscopy Analysis of Isovalent and Aliovalent Doped BaTiO3. *Solid State Ionics* **2013**, *249–250*, 86–92. https://doi.org/10.1016/j.ssi.2013.07.016.

(66) Capiglia, C.; Mustarelli, P.; Quartarone, E.; Tomasi, C.; Magistris, A. Effects of Nanoscale SiO2 on the Thermal and Transport Properties of Solvent-Free, Poly(Ethylene Oxide) (PEO)-Based Polymer Electrolytes. *Solid State Ionics* **1999**, *118* (1–2), 73–79. https://doi.org/10.1016/s0167-2738(98)00457-3.

(67) Uguz, I.; Ganji, M.; Hama, A.; Tanaka, A.; Inal, S.; Youssef, A.; Owens, R. M.; Quilichini, P. P.; Ghestem, A.; Bernard, C.; Dayeh, S. A.; Malliaras, G. G. Autoclave Sterilization of PEDOT:PSS Electrophysiology Devices. *Adv. Healthc. Mater.* **2016**, *5* (24), 3094–3098. https://doi.org/10.1002/adhm.201600870.

(68) Maiolo, L.; Guarino, V.; Saracino, E.; Convertino, A.; Melucci, M.; Muccini, M.; Ambrosio, L.; Zamboni, R.; Benfenati, V. Glial Interfaces: Advanced Materials and Devices to Uncover the Role of Astroglial Cells in Brain Function and Dysfunction. *Adv. Healthc. Mater.* **2021**, *10* (1). https://doi.org/10.1002/adhm.202001268.

(69) Macaya, D. J.; Hayakawa, K.; Arai, K.; Spector, M. Astrocyte Infiltration into Injectable Collagen-Based Hydrogels Containing FGF-2 to Treat Spinal Cord Injury. *Biomaterials* **2013**, *34* (14), 3591. https://doi.org/10.1016/j.biomaterials.2012.12.050.

(70) Saracino, E.; Cirillo, V.; Marrese, M.; Guarino, V.; Benfenati, V.; Zamboni, R.; Ambrosio, L. Structural and Functional Properties of Astrocytes on PCL Based Electrospun Fibres. *Mater. Sci. Eng. C* **2021**, *118*. https://doi.org/10.1016/j.msec.2020.111363.

(71) Sagnella, A.; Pistone, A.; Bonetti, S.; Donnadio, A.; Saracino, E.; Nocchetti, M.; Dionigi, C.; Ruani, G.; Muccini, M.; Posati, T.; Benfenati, V.; Zamboni, R. Effect of Different Fabrication Methods on the Chemo-Physical Properties of Silk Fibroin Films and on Their Interaction with Neural Cells. *RSC Adv.* **2016**, *6*

(11), 9304–9314. https://doi.org/10.1039/c5ra20684g.

(72) Liang, Y.; Offenhäusser, A.; Ingebrandt, S.; Mayer, D. PEDOT:PSS-Based Bioelectronic Devices for Recording and Modulation of Electrophysiological and Biochemical Cell Signals. *Adv. Healthc. Mater.* **2021**, *10* (11). https://doi.org/10.1002/adhm.202100061.

CHAPTER 5

Conclusions

Starting from the key concept of biomimicry, within this work, we aimed for design and development of printable and injectable bio-hybrid inks for the realization of devices suitable for tissue engineering applied to regenerative medicine.

We targeted three different tissues: chondral tissue, bone tissue and neural tissue. The fulfilment of this purpose was pursued by following pivotal subsequential steps. First, the main features of the targeted native tissues were thoroughly considered and evaluated to be able to select the most suitable biomaterial, meaning biocompatible material, fit for the purpose. Then, an accurate evaluation of the possible functionalization exploitable for mimic at best the native tissue was performed. Functional bio-hybrid inks were then realized towards a lengthy optimization process, that was also taking into consideration the technological process meant to be employed for each device production. Each device was designed to be not only bioconductive, meaning grant cells support to attach, spread and grow, but also potentially bioinductive, meaning able to provide cells with the correct cues and stimuli to fulfil the goal.

This aspect was tuned, in each device, through control of different parameters, from the technological process and functional elements to the crosslink method.

After the devices were realized, the obtainment of the designed and desired features was checked by a multi-pronged characterization towards which was possible to point out the main achievements as well as the main setbacks that still need to be overcome. A possible application in regenerative medicine for each developed device was finally suggested.

Acknowledgements

To the whom who built with love and commitment, year after year, the trampoline to make me jump in whatever life I would have ever wanted, no matter how scaring or painful that jump would have been for them to watch. Thank you for transforming your fears and pain in cheering for my attempts, comfort for my failures and happiness for my successes. You have always been and always will be the best I could have ever wished for.

To the whom who showed me what passion and commitment are and mean, and how much they might cost but how much they can give you, thank you. You have been the best example I could have ever had.

To the whom who shared with me a cheap, oddly shaped, suburban room in my first big city life-experience, cracking me up in my darkest moments, feeding my utopian dreams at all times of day and night and toasting with me to the up-and-coming future, thank you. Thank you for remembering me to never give up.

To the whom who warmly welcomed me in my first life experience abroad. You didn't just teach me about a new country, city, and language, but you made me discover a brand-new part of myself. I won't never be grateful enough.

To the whom who were the best mates I could have ever asked for in my wandering period. You didn't just help me finding my way, you made me having fun while searching for it. Thank you for that meaningful time together.

To the whom who inspired me rekindling my flame for science and research, you made me do this. Thank you, from the naïve, passionate, and enthusiastic me. You brought her back to life.

To the whom who jumped with me in this incredible, absorbing, demanding, life-changing adventure that is a PhD. Thank you for walking by my side during this journey, you were the best companions ever.

To the whom who, during this journey, dragged me out from the swamps of insecurity, push me up the cliffs of fear to overcome them one by one and remembered

me to take time to look back and be pleased of my achievements, thank you. I might still be a bit dirty of that mud, but it's thanks to you if I can now remove it myself.

To the whom who, out of the blue, hooked my soul with her bluntness, openness and unquenchable being her. Thank you for being the most perfectly imperfect person I needed so badly in my life. You, my gruff talking cricket, made my time in Faenza.

To the whom who shared with me the coffee in the mornings, the tea in the afternoons and the alcohol in the evenings, who dealt with my everyday brand-new complaints, saw my most embarrassing pyjamas, assisted to my stress-driven reckless shopping and sleepless nights, thank you. To have always loved me as the mesmerizing mess I am.

To the whom who, coming from all over the world, ended up being my Norwegian family, the most random, crazy, improbable, and simply perfect family I could have ever had. Thank you for all the love, the lough, the tears. You were the garden of my new beginning. It won't have been possible without you.

To the whom who is responsible of my listening at Finnish rap in the lab, who was my sun (in a Norwegian winter, to be noted), my shadow, my chocolate dealer, my northern country culture teacher, my everything and more, for nine months of my life. You (and actually the unaware Kasper, the honorary member of our golden team as well as the only man who made me cry even before being born!) are the best present Norway gave to me.

To all the ones who were there, in their unique way, contributing to make me the person able to achieve this goal, thank you. I couldn't have done this without you.

Margherita Montanari